LIBRARY
OCT - 9 2001
National Oceanic &
Atmospheric Administration
U.S. Dept. of Commerce

ISSN 1000-9620

Marine Science Bulletin

Volume 3 • Number 1 2001

LIBRARY
Pacific Islands Fisheries Science Center
NOAA Fisheries
Honolulu, Hawai'i

ISSN 1000-9620
01>
9 771000 962001

NATIONAL MARINE DATA AND
INFORMATION SERVICE OF CHINA

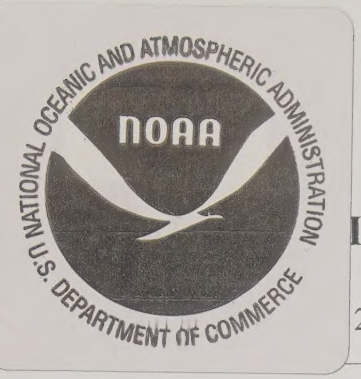

IENCE BULLETIN

2001

CONTENTS

Vertical Structure of Baroclinic Currents over Northern South China Sea Continental Slope ..... *Qiu Zhang* (邱章) (1)

Effects of Second Order Scattered Wave in Stratified Ocean ..... *Huang Hua* (黄华) et al. (9)

Analysis of the Sea Fog in the Sea Around the Great Wall Station, Antarctica ..... *Huang Yaorong* (黄耀荣) et al. (19)

Numerical Simulated Study on the Separation of Oblique Incident and Reflected Waves ..... *Shao Limin* (邵利民) et al. (26)

Studies on the Ecology of Fouling Community in Daguanban Reclamation Area of Luoyuan Bay ..... *Zhou Shiqiang* (周时强) et al. (38)

Isolated Cells of *Porphyra yezoensis* Cultured on Solid Medium ..... *Shen Songdong* (沈颂东) (45)

Toxicity Study of Anti-HABs Agents on *Penaeus chinensis* ..... *Sun Xiaoxia* (孙晓霞) et al. (51)

Maltivariate Analysis of the Occurring Process of *Skeletonema costatum* Red Tide in the Changjiang Estuary ..... *Huang Xiuqing* (黄秀清) et al. (55)

Production of Aneuploid *Pinctada martensii* Dunker in Tetraploid Induction ..... *He Maoxian* (何毛贤) et al. (63)

Application of Microbial BOD Sensors in Marine Monitoring ..... *Zhang Yue* (张 悦) et al. (69)

Species and Distribution of Mangroves in the Fujian Coastal Area ..... *Wang Wenqing* (王文卿) et al. (74)

Studies on Antineoplastic Constituents from Marine Bryozoan *Bugula neritina* Inhabiting South China Sea (III): Isolation and Structural Elucidation of Bryostatin 10, 11 and 18 ..... *Lin Houwen* (林厚文) et al. (83)

Avoidance Reaction of *Penaeus Chinensis* to Heavy Metals (Pb, Cr, Zn) and Heavy Metal Mixtures (Pb-Cr, Pb-Zn) ..... *Chen Minshan* (陈民山) (91)

LIBRARY
OCT - 9 2001
National Oceanic &
U.S. Dept. of Commerce

Vertical Structure of Baroclinic Currents over Northern South China Sea Continental Slope

Qiu Zhang (邱 章)
South China Sea Institute of Oceanology, the Chinese Academy of Sciences, Guangzhou, 510301

Abstract The 28.6 d time series of ADCP currents at 27 depth levels, (11,15,…,115m) which are obtained from a mooring station at the northern South China Sea continental slope, have been decomposed into barotropic and baroclinic components. The emphasis in this paper is on the analysis of the time series of baroclinic currents by means of several methods,such as the tidal harmonic analysis, the power spectra and the kinetic energy estimation. The major results are as follows: (1) In respect of the baroclinic currents, the values of several parameters first decrease and then increase with depth. These parameters include the temporal mean value of the cross-shelf component, the standard deviations, the amplitudes of K_1 constituents, the mean eddy kinetic energy, as well as the significant peaks of the power spectra of the cross-shelf components. (2) The diurnal period of the baroclinic currents is dominant. The diurnal tidal current rotates clockwise and the major axis of current ellipse is located along the directions of NW-SE. The vertical distribution of the phases of the diurnal constituent varies with the different water layers. Around the 67m depth level, the phase changes very much.At those layers far away from the 67m depth level, the vertical distribution of the phase is relatively stable, but with opposite phases in the upper and lower water layers.For the upper layers between the surface and 67m,the phases are around 300°; for the lower layers between 67m and 115m, the phases are around 120°.(3) The mean eddy kinetic energy of the baroclinic current is quite large, accounting for 41% of the mean kinetic energy of the measured currents. The cross-shelf component is larger than the along-shelf one. The two baroclinic current components correspond to the major and minor axes of the current ellipse of the diurnal constituent respectively. (4) The power spectra of the baroclinic currents show a singnificant period of about 24h, with 23.6h at both 19m and 99m and 24.4h at 55m. The vertical distributions of the significant spectra-peak values of the power spectra of both the cross-shelf and along-shelf components of both the baroclinic currents are different. The former increases with depth, then decreases and finally increases again while the latter decreases with depth.

Keywords Northern South China Sea, barotropic current, baroclinic current

Rich in marine resources, the northeastern sea area of the South China Sea boasts great prospects for development.As an important component part of marine resources, oil and natural gas has recently attracted numerous oil companies both at home and abroad to carry out exploration and exploitation of oil and natural gas in this sea area. To conduct such work, it is undoubtedly necessary to know well and grasp the marine environmental condition of this sea area and its changing pattern.In recent years, some work has been done in the research on internal waves in the light of the offshore exploration and exploitation of oil and natural gas in this sea area[1-4], which has laid a foundation for the thorough

The paper is financially supported by the China National Key Basic Research Project (G1999043810), Guangdong Science and Technology Innovation Project (99B07102G), Chinese Academy of Sciences Innovation Project (KZCX2-206) and (CXJJ-28)

research on baroclinic currents and internal waves. Based on about one month's fixed-point observations of current by ADCP, the paper mainly analyses the baroclinic currents in relation to the internal waves in this sea area so as to gain a better understanding of it.

1 Data and methods

1.1 Acquisition and decomposition of data

In March~April, 1996, the current profiler ADCP produced by the U.S.RD Instruments Company was deployed in the continental slope area over 300 metres deep to the west of the Dongsha Islands (20° 41'N,115°52' E) at 27 equi-spacing depth levels between 11m and 115m. The sea currents are observed every 3 minutes and the 28.6d time series of measured current data at 27depth levels after being quality checked and controlled are chosen within the same time period (10:09, March 9, 1996 ~ 01:23, April 7, 1996).And then these data are decomposed layer by layer into an along-shelf component $U(z,t)$ (its normal direction is 40°) and a cross-shelf component $V(z, t)$ (its normal direction is 310°) respectively.

In the studied sea area, the seawater stratification is obvious, the thermocline exists all the year round[5] and the activities of internal tide are frequent[1-4].The current caused by the internal tide movement belongs to the baroclinic current. As far as the along-shelf component of the measured current at a certain water layer $U(z,t)$ is concerned, it is regarded as the sum of the barotropic current $U_b(t)$ and the baroclinic current $U_d(z, t)$, i.e.,$U(z,t) = U_b(t) + U_d(z, t)$.Its barotropic current component may be expressed by:

$$U_b(t) = \frac{1}{z}\int_{z_1}^{z_2} U(z,t)\, dz \qquad (1)$$

Where $z = z_2 - z_1$. z_1 and z_2 are the upper bound depth and the lower bound depth of the observed water body respectively. As the observed water layers are equally spaced, in the actual computation, arithmetic means may be simply obtained for the observations at each depth level at the same moment respectively, while the baroclinic current at the same moment is the difference between the observed current and the barotropic current at this moment:

$$U_d(z, t) = U(z, t) - U_b(t) \qquad (2)$$

For the cross-shelf component of the observed current at the same depth level $V(z,t)$,the same method may be used to decompose it into the barotropic current $V_b(t)$ and the baroclinic current $V_d(z,t)$. In this way, so long as we have the time series of observed current, we can obtain its corresponding barotropic and baroclinic current series.

1.2 Kinetic energy calculation

The mean value of the along-shelf component $U(z, t)$ of the observed current at a particular depth level at the observation interval of this level (T) may be calculated by averaging its time series versus time:

$$\overline{U}(z) = \frac{1}{T}\int_0^T U(z, t)\, dt \qquad (3)$$

where T is the duration of observation. From the difference between the time series of the along-shelf component of observed current and its mean value $U(z, t) - \overline{U}(z)$, we may get the anomaly time series of the along-shelf component of observed current $U'(z,t)$:

$$U'(z,t) = U(z,t) - \overline{U}(z) \tag{4}$$

The square of the anomaly time series of the along-shelf component of observed current $U'^2(z,t)$ is averaged versus time and the result is the variance of the time series of the along-shelf component of observed current $U(z,t)$:

$$\overline{U'^2}(z) = \frac{1}{T}\int_0^T U'^2(z,t)\,dt \tag{5}$$

For the cross-shelf component of observed current at the same depth level $V(z,t)$, the same method may be used to obtain its mean value $\overline{V}(z)$ and variance $\overline{V'^2}(z)$. Suppose the along -shelf component and the cross-shelf component of the baroclinic carrent at the same depth level are $U_d(z,t)$ and $V_d(z,t)$ respectively. In the same way we can obtain the mean value $\overline{U_d}(z)$ and variance $\overline{U_d'^2}(z)$ of its along-shelf component, as well as the mean value $\overline{V_d}$ (z) and variance $\overline{V'^2}(z)$ of the cross-shelf component.

Given the mean value and variance, the observed current mean kinetic energy and eddy mean kinetic of the unit quality are respectively:

$$MK(z) = (\overline{U}^2(z) + \overline{V}^2(z))/2 \tag{6}$$

$$EK(z) = (\overline{U'^2}(z) + \overline{V'^2}(z))/2 \tag{7}$$

The unit is cm^2/s^2.

The mean kinetic energy and eddy mean kinetic energy of the baroclinic current are respectively:

$$MK_d(z) = (\overline{U_d^2}(z) + \overline{V_d^2}(z))/2 \tag{8}$$

$$EK_d(z) = (\overline{U'^2}(z) + \overline{V'^2}(z))/2 \tag{9}$$

The ratio of the eddy mean kinetic energy of the baroclinic current to the mean kinetic energy of the observed current is:

$$K(z) = EK_d(z)/MK(z) \tag{10}$$

1.3 Tidal harmonic analysis

Harmonic analysis is made of the barotropic and baroclinic current series obtained from decomposition in Section 1.1 by means of the tidal harmonic analysis using the least square method[6], from which the harmonic constants of the relevant constituents of tidal current are obtained and then the elliptical elements of the diurnal constituent K_1 are calculated.

1.4 Computation of the baroclinic current power spectra

After the along-shelf component $U_d(z,t)$ and the cross-shelf component $V_d(z,t)$ of the baroclinic current at each depth level have been standardized, the power spectra analysis of autocorrelation function [7] is applied to calculate the power spectra of along-shelf and cross-shelf components respectively.

In calculating the power spectra, the lengths of the time series of the along-shelf and cross-shelf components of the baroclinic current at each depth level are both 13 716, the time interval of data d τ is 3 min and the maximum back extension number M is 320.

2 Results and discussion

2.1 Vertical distribution of the baroclinic current mean values and standard deviations

The internal wave in the ocean is a gravity wave occurring in the interior of the stably stratified ocean and the current resulted from such wave motion belongs to the baroclinic current, whose directions are opposite at the crest and trough of the internal wave[8] .In the studied sea area, the seawater stratification is obvious in four seasons and there exists a thermocline all the year round in between the depths of 10～120m[5]. The water layer where the current data analysed in this paper lie is just located within the thermocline. For the mean values of the baroclinic current obtained after being decomposed by means of the above-mentioned method, there obviously exists the phenomenon of the oppositely moving upper and lower water bodies in their vertical distribution.Fig.1a is the vertical distribution of the mean values of the along-shelf and cross-shelf components of the baroclinic current during the observation,which shows the distributive characteristic of the baroclinic current increasing with depth, becoming from large to small and finally large again.

The standard deviation of the sample baroclinic current is one of the statistics describing its dispersion of distribution. The vertical distribution of standard deviation of the sample baroclinic current may reflect the pulsation of baroclinic current in the observed water body. Fig.1b shows the vertical distribution of standard deviation of the sample baroclinic current given according to the method of calculating variance mentioned in the preceding section, from which it can be seen that the distributions of its cross-shelf and along-shelf components are very similar. From the 15m depth level to the 55m depth level, the standard deviation of the sample becomes smaller with the increase of depth, the least at the 55m depth level. From the 55m depth level to the 115m depth level, it becomes from small to large. For the depth levels shallower than 51m and deeper than 75m, the sample standard deviations of the cross-shelf component of the baroclinic current are all larger than those of the along-shelf component, thus suggesting that at these depth levels, the pulsation of the cross-shelf component is larger than that of the along-shelf component. The sample standard deviation is the least around the 55m depth level, where the phase of the K_1 constituent of the baroclinic current changes very much. Limited in the observation depth, what depth such oscillation will affect is beyond discussion.

2.2 Kinetic energy distribution

Table 1 shows the results obtained by using the above-mentioned method of calculating the kinetic energy. As for the energies of the observed current, the along-shelf component of the mean kinetic energy $\overline{U}^2(z)$ is much larger than the cross-shelf component $\overline{V^2}(z)$ while the along-shelf component of the eddy kinetic energy $\overline{U'^2}(z)$ is smaller than the cross-shelf component $\overline{V'^2}(z)$. As far as the kinetic energy of the baroclinic current is concerned, the kinetic energies of both the along-shelf component $\overline{U}_d^2(z)$ and the cross-shelf component $\overline{V_d^2}(z)$ are small, with a maximum of 2.9 cm^2/s^2 and a minimum of less than 0.1cm^2/s^2 while, for the eddy kinetic energy, the cross-shelf component $\overline{V_d'^2}(z)$ is larger than the along-shelf component $\overline{U_d'^2}(z)$. Fig. 2 shows the vertical distribution of mean eddy kinetic energy of baroclinic currents, which is similar to the vertical distribution of the sample standard deviations of baroclinic currents, i.e., it increases with depth at the depth levels of 11~115m, becoming from large to small, and finally large again. As for the ratio of the mean eddy kinetic energy of baroclinic currents to the mean kinetic energy of observed currents, the mean eddy kinetic energy accounts for 23%

~73%,with an average of 41%.

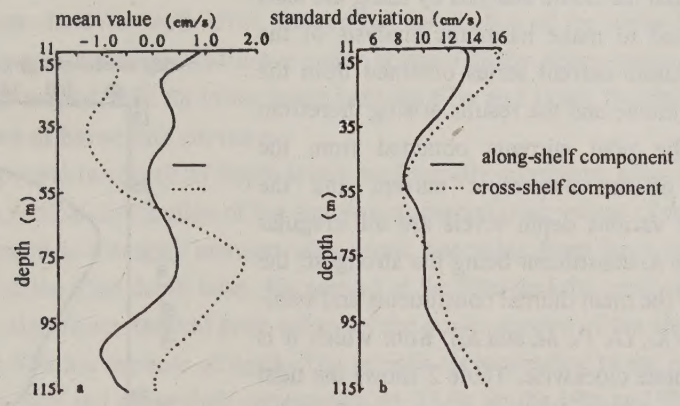

Fig.1 Vertical distributions of sample mean value (a) and standard deviation (b) of baroclinic currents

Tab. 1 Statistical results of kinetic energy

depth	along-shelf component (cm^2/s^2)				cross-shelf component (cm^2/s^2)				$MK(z)$	$MK_d(z)$	$K(z)$
(m)	$\overline{U}^2(z)$	$\overline{U'^2}(z)$	$\overline{U}_d^2(z)$	$\overline{U'^2_d}(z)$	$\overline{V}^2(z)$	$\overline{V'^2_d}(z)$	$\overline{V}(z)$	$\overline{V'^2_d}(z)$	(cm^2/s^2)	(cm^2/s^2)	
11	523	550	0.7	174	54	884	1.2	240	289	207	0.72
15	537	558	0.3	183	61	898	0.5	253	299	218	0.73
19	555	544	0.0	173	61	875	0.5	241	308	207	0.67
23	553	526	0.1	163	59	841	0.6	218	306	191	0.62
27	547	502	0.1	147	55	802	1.1	188	301	168	0.56
31	542	480	0.2	128	52	760	1.5	155	297	142	0.48
35	544	463	0.1	110	51	729	1.7	129	298	120	0.40
39	553	450	0.0	93	51	706	1.7	109	302	101	0.33
43	563	440	0.0	80	54	678	1.2	92	309	86	0.28
47	567	436	0.0	73	56	650	0.9	81	312	77	0.25
51	566	439	0.0	72	58	624	0.7	74	312	73	0.23
55	562	444	0.0	76	63	606	0.3	73	313	75	0.24
59	560	449	0.0	85	70	591	0.0	75	315	80	0.25
63	554	449	0.0	93	79	575	0.2	80	317	87	0.27
67	548	443	0.1	98	88	562	0.9	88	318	93	0.29
71	545	434	0.1	100	97	553	1.9	99	321	100	0.31
75	544	425	0.2	101	103	546	2.8	109	324	105	0.32
79	545	414	0.1	100	103	538	2.9	119	324	110	0.34
83	549	406	0.1	99	99	524	2.2	126	324	113	0.35
87	560	401	0.0	99	94	506	1.5	131	327	115	0.35
91	575	402	0.1	102	90	487	1.1	135	333	119	0.36
95	590	409	0.3	111	87	469	0.7	139	339	125	0.37
99	605	418	0.8	124	82	455	0.4	149	344	137	0.40
103	614	426	1.1	138	79	447	0.1	163	347	151	0.43
107	613	432	1.1	151	74	444	0.0	181	344	166	0.48
111	602	436	0.7	162	72	442	0.0	200	337	181	0.54
115	587	436	0.3	171	71	441	0.0	218	329	195	0.59
average	563	452	0.24	119	73	616	0.99	143	318	131	0.41

2.3 Results of tidal harmonic analysis

The method of tidal harmonic analysis by using the least square method is used to make harmonic analysis of the barotropic and baroclinic current series obtained from the above-mentioned formulae and the results arising therefrom are very similar: the tidal currents obtained from the harmonic analysis of the barotropic current and the baroclinic current at various depth levels are all irregular diurnal ones, with the K_1 constituent being the strongest; the elliptical elements of the main diurnal constituents and semi-diurnal constituents (K_1, O_1, P_1, M_2 and S_2), from which it is found that they all rotate clockwise. Table 2 shows the tidal current characteristics and the elliptical elements of K_1 constituent at the barotropic current and the three depth levels (19, 55 and 99m) of baroclinic current, from which it is clear that the values of ratio of their tidal current character are very close, 4.0 for the barotropic current and 2.5 ~ 5.3 for the baroclinic current: the largest, 5.3 at the 19m depth level, the second, 3.2 at the 99m depth level and the smallest, 2.5 at the 55 m depth level. They all belong to the irregular diurnal tidal currents. Research findings of the numerical simulation of the tide and tidal current in the South China Sea show that the tides in this sea area belong to the mixed ones, which seems to be identical with those in the paper. From Table 2 and Fig. 3 we can see the major axis of current ellipse:for the barotropic current, it is approximately in the W-E direction while for the baroclinic current it is in the NW-SE direction at the upper depth level (19m) and the lower depth level (99m), longer than that at the middle depth level (55m), which is nearly in the W-E direction; the maximum possible current speeds occur at the same time at the upper and lower depth levels, but their directions are opposite; that for the upper level is in the SE direction while that for the lower level is in the NW direction, and the ellipses at the upper and lower levels are not so flat as that at the middle level; moreover, both the barotropic and baroclinic diurnal constituents rotate closewise, i.e., the characteristic of rotating to the right.

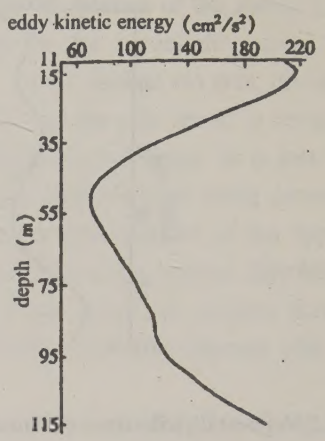

Fig.2 Vertical distribution of mean eddy kinetic energy of baroclinic currents

Tab. 2 Tidal current characteristics and elliptical element of K_1 constituent

Type		tidal current characteristics	elliptical element of K_1 constituent				
			major axis	direction	time	minor axis	ellipticity
barotropic current		4.0	26cm	106°	2.5h	16cm	−0.67
baroclinic current	19m	5.3	18cm	139°	4.8h	14cm	−0.77
	55m	2.5	8cm	75°	3.9h	4cm	−0.61
	99m	3.2	16cm	308°	4.8h	14cm	−0.79

Statistics are made of the results of tidal harmonic analysis of the baroclinic currents. Fig. 4 shows the vertical distribution of amplitude and phase of K_1 constituent, from which it can be seen that the distribution of amplitude has the similar trend to that of kinetic energy:at the 11~23m depth level, there exists a small swing of amplitude of the K_1 constituent, at 23~67m level, the amplitude of the K_1 constituent decreases with the increase of depth, at the 67m level, it is less than 1 cm/s at the least and, at the 67

~115m level, increases with depth. The vertical distribution of the phases of the diurnal constituent varies with the different water layers. Around the 67m depth level,the phase changes greatly. At those layers far away from the 67m depth level, the vertical distribution of the phase is relatively stable, but with opposite phases in the upper and lower water layers. For the upper layers between the 11m and 67m, the phases are around 300°; for lower layers between 67m and 115m, the phases are around 120°.

2.4 Power spectra of baroclinic currents

The power spectral results of 27 depth levels are basically consistent, showing a significant period of about 24h. The vertical distribution of the significant spectral peak values of the power spectra of the cross-shelf component is that they increase with depth, becoming from large to small and then large again: the largest at the 19m depth level, the second at the 99m and the smallest at 55m. The vertical distribution of the significant spectral peak values of the power spectra of the along-shelf component is that they decrease with the increase of depth. The periods corresponding to the maximum spectral peak values of the cross-shelf and along-shelf components are 23.6h for the 19m and 99m layers and 24.4h for the 55m layer.

The power spectrum periodic significance is tested through x^2 distribution and the significance level of spectral peak values around 24h is 5%.

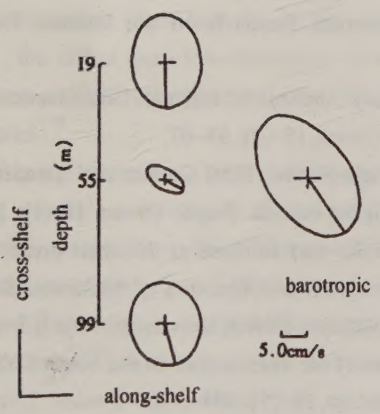

Fig.3 Vertical distribution of ellipse of K_1 constituent

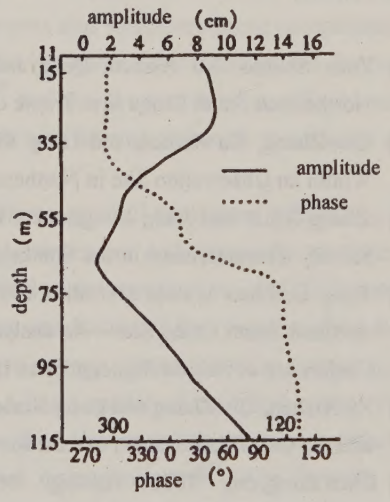

Fig.4 Vertical distribution of amplitude and phase of K_1 constituent

3 Conclusions

The analysis of the 28.6d time series data at 11~115m depth levels obtained from a mooring station at the northern South China Sea continental slope yields the following results:

(1)In respect of the baroclinic currents, the values of several parameters first decrease and then increase with depth. These parameters include the temporal mean value of the cross-shelf component, the standard deviations, the amplitudes of K_1 constituent, the main eddy kinetic energy, as well as the significant peaks of the power spectra of the cross-shelf component.

(2) The diurnal period of the baroclinic current is significant and the major axis direction of current ellipse is NW-SE. The diurnal tidal current has the characteristic of rotating to the right, i.e., rotating clockwise. The vertical distribution of the phases of the diurnal constituent varies with different water layers. Around the 67m depth level, the phase changes greatly; At those layers far away from the 67m depth level, the vertical distribution of phases is relatively stable, but with opposite phases in the upper and lower water layers. For the upper layers between the 11m and 67m, the phases are around 300°; for the lower layers between 67m and 115m, the phases are around 120° .

(3) The mean eddy kinetic energy of the baroclinic current is quite large, accounting for 41% of the mean kinetic energy of the measured currents. The cross-shelf component is larger than the along-shelf one and the two baroclinic current components correspond to the major and minor axes of the current ellipse of the diurnal constituent respectively.

(4) The power spectra of the baroclinic currents shows a significant period of about 24h, with 23.6h at both 19m and 99m, and 24.4h at 55m.

(5) The vertical distributions of the significant spectra-peak values of the power spectra of both the cross-shelf and along-shelf components of the baroclinic currents are different. The former increases with depth, then decreases and finally increases again while the latter decreases with depth.

Reference

[1] Yuan Shurao, Xu Xizhen, Deng Jiuzai et al. (1995) Numerical Research on the Internal Tides in Northeasten South China Sea. *Tropic Ocean*, **14** (4): 15~23.

[2] Qiu Zhang, Xu Xizhen, and Long Xiaomin (1996) Preliminary Analysis of Internal Tide Characteristics Within an Observation Site in Northern South China Sea. *Tropic Ocean*, **15** (4): 63~67.

[3] Zhang Aijun and Jiang Mingshun (1999) Analysis of the Single-Station Tidal Current and Temperature-Salinity Characteristics in the Southeastern Sea Area of the Dongsha Islands. *Tropic Ocean*, **18** (1): 23~30.

[4] Fang G, Zhao J, Bole J et al. (1995) Circulation, internal tides and solitions at the shelf break of the northern South China Sea —An analysis of measured currents. *Program and Abstracts of the Marine Science Conference in Taiwan Adjacent Seas.* Institute of Oceanography, National Taiwan University, Taipei, 5 ~ 52.

[5] Xu Xizhen, Qiu Zhang and Long Xiaomin (1993) Basic Features of the Thermocline in the South China Sea and the One-Dimensional Forecast Model. *Oceanology and Limnology*, **24** (5): 494~502.

[6] Chen Zongyong (1980) *Tidology.* Beijig: Science Press, 138~185.

[7] Huang Zhongshu (1984) Spectral Analysis Method and Its Application in Hydrometeorology, Beijing: Meteorological Press, 1~82.

[8] Fang Xinhua (1987) Marine Internal Waves. *Encyclopedia of China, Atmospheric Sciences, Marine Sciences, Hydrological Sciences.* Beijing: Encyclopedia of China Publishing House, 360~362.

[9] Fang Guohong, Cao deming and Huang Qizhou (1994) Numerical Simulation of Tides and Tidal Currents in the South China Sea. *Acta Oceanologica Sinica*, **16** (4): 1~12.

Effects of Second Order Scattered Wave in Stratified Ocean

Huang Hua（黄 华），Zhan Jiemin（詹杰民），Zhu Dingjin（朱顶金），Liao Deju（廖德驹）
Dept. of Applied Mechanics and Eng., Zhongshan University, Guangzhou, 510275

Abstract By using the theories on Stokes multicolored water waves and taking the two- layer ocean as a basic model of stratified ocean, the paper analyzes the problems related to the effects of the nonlinear water wave on offshore structures. A mathematical expression is presented to describe second order wave radiation conditions. Using integral principle, the analytical integral solutions are given to evaluate second order scattered wave loads on general vertical circular cylinders in the two-layer ocean, and the special recurrence formulas for infinite integrals over free and stratified surfaces are derived.

Keywords Stratified ocean, second order wave, two layer ocean, scattering, diffracting, wave load

Stratification is a usual phenomenon in the ocean and will produce inner waves inside the layered ocean ,which usually makes the problems of interaction between waves and structures more complicated. Some researches show that the surface wave and inner radiated waves generally concur in the layered ocean , the effect from low-frequency wave may be very strong[1-2] and the properties of stratified water may have a direct influence on the evaluation of the water dynamic coefficients and total wave loads on structures[3-4].

Although there have been some results about linear wave problems, we still have great difficulties in finding possible solutions to wave interference caused by multiple structures and especially nonlinear diffracted wave effects, due to the special mechanism of multicolored water waves, sum- and difference-frequency potentials from high order waves and nonlinear boundary conditions of free water surface and stratified flow surface. Considering that the main part of inner wave energy comes from the lowest type of inner wave[1,5], it is appropriate to take the two-layer ocean as a basic model of stratified ocean. For estimating second order wave loads on structures, a approach based on the boundary element method , which makes use of Greens function and intergral principle ,was once presented[5]. The formula of integration given in the paper is only regarded as approximate solution to second order scattered wave load, due to having taken an improper or weak model as second order radiation condition. In this paper, a general type of vertical circular cylinder is given as the analyzed structure, then, an accurate solution to first order diffracted wave potential is found by means of the method of eigenfunction expansion, thereby a possible and proper model of second order radiation condition is derived and, furthermore, a rigorous integral solution (including a practical approach to evaluating the slowly convergent integrals over free and stratified flow surfaces) to second order scattered wave load is established.

Received on 25 May, 1999; Revised on 20 October, 1999
Foundation: National Natural Science Foundation of China (19802023)

1 Governing Equations of Diffracted Water Wave Potential in the Two-Layer Ocean

It is appropriate to take the general vertical circular cylinder as a specified structure in order to compare the results given in this paper with those we have known about uniform ocean. As shown in Fig. 1, the whole fluid domain is divided into three subregions (ν_1- ν_2), which are the three most basic forms of fluid subregions[6], $z = h_0$ expresses the mean interface between the two superposed fluids (ρ_1 and ρ_2 are the upper and lower layer fluid density, respectively and $\rho_2 > \rho_1$), which may have three possible value ranges (assuming $h_1 > h_2$) as (a) $h_1 < h_0 \leqslant h$, (b)$h_2 < h_0 \leqslant h_1$ (shown in Fig. 1), (c) $0 \leqslant h_0 \leqslant h_2$ (let c (=1, 2, 3) to denote the above three possible value ranges). From the theories on multicolored water waves, Stokes first and second order wave potentials in the two-layer ocean are governed by

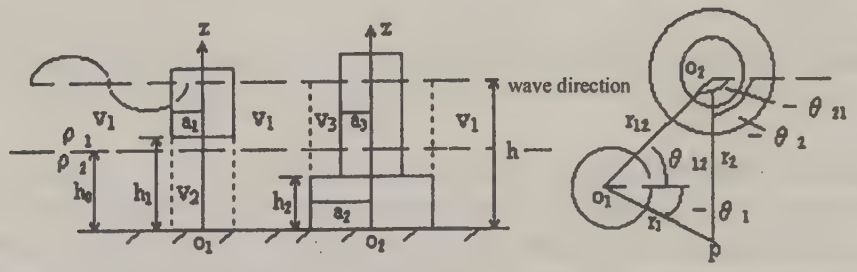

Fig.1 General type of vertical circular cylinder in the two-layer ocean

$$\Phi = \varepsilon\Phi_1 + \varepsilon^2\Phi_2 + \cdots \tag{1}$$

$$\Phi_1 = \Phi_1^i + \Phi_1^s = \sum_{m=1} \{Re[\varphi_m^i e^{-iw_m t} + Re[\varphi_m^s e^{-i\omega_m t}]\} \tag{2}$$

$$\Phi_2 = \Phi_2^i + \Phi_2^s = \sum_{n,m=1} [(\varphi_{inm}^+ + \varphi_{snm}^+) e^{-i\Omega_{nm}^+ t} + (\varphi_{inm}^- + \varphi_{snm}^-) e^{-i\Omega_{nm}^- t}] \tag{3}$$

where ε is the perturbation parameter, $\Omega_{nm}^{\pm}$ (= $\omega_n \pm \omega_m$) the second order sum- and d ifference-frequencies, Φ, Φ_1, Φ_2, φ_m^i and φ_m^s correspond to total wave potential, first order total wave potential, second order total wave potential, first order incident potential and scattered potential, respectively; $\varphi_{inm}^{\pm}$ and $\varphi_{snm}^{\pm}$ are second order sum- and difference-frequency incident and scattered potentials respectively. The potentials φ_m^s and $\varphi_{snm}^{\pm}$ are governed by

$$\nabla^2(\varphi_m^s;\ \varphi_{snm}^{\pm}) = 0 \qquad (\nu_1+\nu_2+\nu_3) \tag{4}$$

$$g\frac{\partial}{\partial z}(\varphi_m^s;\ \varphi_{snm}^{\pm}) - [\omega_m^2\varphi_m^s;\ (\Omega_{nm}^{\pm})^2\varphi_{snm}^{\pm}] = (0;\ E_{nm}^{\pm}) \qquad (z = h) \tag{5}$$

$$\frac{\partial}{\partial n}[(\varphi_m^s + \varphi_m^i);\ (\varphi_{snm}^{\pm} + \varphi_{inm}^{\pm})] = 0 \qquad (S_b \text{ and } S_0) \tag{6}$$

$$\rho\left\{g\frac{\partial}{\partial z}(\varphi^{s}_{m},\varphi^{\pm}_{snm})-[\omega^{2}_{m}\varphi^{s}_{m},(\Omega^{\pm}_{nm})^{2}\varphi^{\pm}_{snm}]\right\}\Big|^{z=h_0+0}_{z=h_0-0}=(0,G^{\pm}_{nm}) \tag{7}$$

$$\frac{\partial}{\partial z}(\varphi^{s}_{m},\varphi^{\pm}_{snm})\Big|_{z=h_0+0}-\frac{\partial}{\partial z}(\varphi^{s}_{m},\varphi^{\pm}_{snm})\Big|_{z=h_0-0}=(0,H^{\pm}_{nm}) \tag{8}$$

$$\lim_{r_e\to\infty}\sqrt{r_e}\left\{\left(\frac{\partial}{\partial r_e}\varphi^{s}_{m}-ik_m\phi^{s}_{m}\right);\ \int_0^{2\pi}\left(\frac{\partial}{\partial r_e}\varphi^{\pm}_{snm}-k^{\pm}_{nm}\varphi^{\pm}_{snm}\right)\mathrm{d}\theta_e\right\}\to 0 \tag{9}$$

where e (= 1, 2) denotes the cylinder number, S_b the wetted surface of the body, S_0 the sea bottom surface, ρ the layer fluid density ($\rho=\rho_1$ for the upper layer fluid and $\rho=\rho_2$ forthe lower layer fluid). The part of Eq. (9) related to the second order scattered is only an approximate model for radiation condition[5]. The forcing terms are given by

$$E^{\pm}_{nm}=(i/2)\left\{\Omega^{\pm}_{nm}\nabla\varphi^{s}_{n}\cdot\nabla\varphi^{s,\pm}_{m}-\omega_n\varphi^{s}_{n}\left[\frac{\partial^2\varphi^{s,\pm}_{m}}{\partial z^2}-g^{-1}\omega^{2}_{m}\varphi^{s,\pm}_{m}\right]+2\Omega^{\pm}_{nm}\nabla\varphi^{s}_{n}\cdot\nabla\varphi^{i,\pm}_{m}-\right.$$

$$\left.\omega_n\varphi_n\left[\frac{\partial^2\varphi^{i,\pm}_{m}}{\partial z^2}-g^{-1}\omega^{2}_{m}\varphi^{i,\pm}_{m}\right]\mp\omega_m\varphi^{i,\pm}_{m}\left[\frac{\partial^2\varphi^{s}_{n}}{\partial z^2}-g^{-1}\omega^{2}_{n}\varphi^{s}_{n}\right]\right\} \tag{10}$$

$$G^{\pm}_{nm}=\rho E^{\pm}_{nm}\Big|^{z=h_0+0}_{z=h_0-0} \tag{11}$$

$$H^{\pm}_{nm}=(i/2)\left\{\nabla_1\cdot\left[\omega_n^{-1}\frac{\partial\varphi^{s}_{n}}{\partial z}\nabla_1\varphi^{s,\pm}_{m}\right]+\nabla_1\cdot[\eta^{i,\pm}_{m}\nabla_1\varphi^{s}_{n}]+\right.$$

$$\left.\nabla_1\cdot\left[\omega_n^{-1}\frac{\partial\varphi^{s}_{n}}{\partial z}\nabla_1\varphi^{i,\pm}_{m}\right]\right\}\Big|_{z=h_0} \tag{12}$$

where $X^{x,+}=X^{x}=(X^{x,-})^{*}$ (X and x denote general notations), $\eta^{i}_{m}=\omega_m^{-1}\frac{\partial\varphi^{i}_{m}}{\partial z}$, $\nabla_1=(\frac{\partial}{\partial r_e},\frac{\partial}{r_e\partial\theta_e})$, $k=(k_m,k^{\pm}_{nm})$ are the positive real roots, corresponding to $\omega=(\omega_m,\Omega^{\pm}_{nm})$, of the dispersion equation as follows

$$\omega^2=g\upsilon$$

$$=\frac{k\{\rho_0T(1+T_1T_2)\pm[\rho_0^2T^2(1+T_1T_2)^2-4(\rho_0-1)T_1T_2(\rho_0+T_1T_2)]^{1/2}\}}{2(\rho_0+T_1T_2)} \tag{13}$$

where $T=\tanh kh$, $T_1=\tanh k(h-h_0)$, $T_2=\tanh kh_0$, $\rho_0=\rho_2/\rho_1$, first and second solutions of Eq. (13) correspond to surface wave and inner wave respectively. Due to nonlinear boundary conditions, it is very difficult to find an accurate solution to $\varphi^{\pm}_{snm}$.

2 Analytical Solution to First Order Wave Potential and Radiation Condition on Second Order Diffracted Wave

First order incident water wave potential in the two-layer ocean may be rewritten as[1]

$$\varphi_m^i = i(k_m\omega_m)^{-1} A_m f_1(\omega_m, k_m, z)\cosh k_m z \cosh k_m h\, e^{ik_m x} \tag{14}$$

$$f_1(\omega,k,z) = \begin{cases} k-\upsilon T+(\upsilon-kT)\tanh kz & (h_0<z\le h) \\ (\nu-kT_1)(1-TT_2)/T_2 & (0\le z<h_0) \end{cases} \tag{15}$$

where ω, and k satisfy Eq. (13), and A_m is wave amplitude. By considering scattered wave effect and wave interference between multiple cylinders, we may have

$$\varphi_m^{(1)} = \varphi_m^{i(1)} + \varphi_m^{s(1)}$$

$$= \sum_{n=-\infty}^{\infty} \left[i^{n+1}(k_m\omega_m)^{-1} A_m \cosh k_m h f_1(\omega_m, k_m, z)\cosh k_m z J_n(k_m r_e)\, e^{in\theta_e} + \right.$$

$$\left. \sum_{f=1}^{2}\sum_{l=0}^{\infty} p_{nl}^{(1)}(r_f, z)\, e^{in\theta_f} \right] \tag{16}$$

$$p_{nl}^{(1)}(r_f, z) = A_{nlm}^{(1,f)} K_n(\alpha_{lm}^{(1)} r_f)\cos\alpha_{lm}^{(1)} z f_1(\omega_m, i\alpha_{lm}^{(1)}, z) \tag{17}$$

$$\varphi_m^{(k)} = \varphi_m^{i(k)} + \varphi_m^{s(k)} = \sum_{n=-\infty}^{\infty}\sum_{l=0}^{\infty} P_{nl}^{(k)}(r_e, z)\, e^{in\theta_e} \quad (k=2,3) \tag{18}$$

$$p_{nl}^{(2)}(r_1, z) = \delta_{1c} A_{nlm}^{(2)}[\delta_{0l} r_1^n + 2(1-\delta_{0l}) I_n(l\pi h_1^{-1} r_1)]\cos l\pi h_1^{-1} z + (\delta_{2c} + \delta_{3c})\, A_{nlm}^{(2)} f_2(z) I_n(\alpha_{lm}^{(2)} r_1) \tag{19}$$

$$f_2(z) = \begin{cases} [(\nu_m - kT_1')(1 - T'T_2')/T_2']\cos\alpha_{lm}^{(2)}(h_1 - z) & (\alpha_{lm}^{(2)} = \beta_{lm}, h_0 < z \le h_1) \\ f_1(\omega_m, i\alpha_{lm}^{(2)}, z) & (\alpha_{lm}^{(2)} \text{ is the inner wave solution to } \alpha_{lm}^{(1)}, 0 \le z < h_0) \end{cases} \tag{20}$$

$$p_{nl}^{(3)}(r_2, z) = \delta_{3c}[A_{nlm}^{(3)} I_n(\mu_{lm} r_2) + B_{nlm}^{(3)} K_n(\mu_{lm} r_2)]\cos\mu_{lm}(z - h_2) + (\delta_{1c} + \delta_{2c}) f_3(z)\cos\alpha_{lm}^{(3)}(z - h_2)[A_{nlm}^{(3)} I_n(\alpha_{lm}^{(3)} r_2) + B_{nlm}^{(3)} K_n(\alpha_{lm}^{(3)} r_2)] \tag{21}$$

$$f_3(z) = \begin{cases} k-\upsilon_m T'' + i(\upsilon_m - kT'')\,\mathrm{tg}\,\alpha_{lm}^{(3)}(z-h_2) & (h_0<z\le h) \\ (\nu_m - kT_1'')(1-T''T_2'')/T_2'' & (h_2\le z<h_0) \end{cases} \tag{22}$$

where $\varphi_m^{(k)}$ expresses the first total wave potential in field ν_k, $A_{nlm}^{(1,f)}$ (f=1,2), $A_{nlm}^{(2)}$, $A_{nlm}^{(3)}$ and $B_{nlm}^{(3)}$ are all unknown coefficients, $J_n(x)$, $I_n(x)$ and $K_n(x)$ denote different kinds of Bessel functions. In Eqs. (17)—(22), we have that $\alpha_{0m}^{(1)} = -ik_m$, $\alpha_{lm}^{(1)}$ ($l \neq 0$) are the imaginary roots of Eq. (13), $T' = -\tanh\beta_{lm}(h - h_1)$, $T_2' = \tanh\beta_{lm} h_0$, $T_1' = \tanh\beta_{lm}(h_1 - h_0)$ (β_{lm} are the inner wave solutions of Eq. (13) if T, T_1 and T_2 in Eq. (13) are replaced respectively by T', T_1' and T_2'), $\mu_{lm}\,\mathrm{tg}\,\mu_{lm}(h - h_2) = -\omega_m^2/g$, $T'' = i\,\mathrm{tg}\,\alpha_{lm}^{(3)}(h - h_2)$, $T_2'' = i\,\mathrm{tg}\,\alpha_{lm}^{(3)} h_0$, $T_1'' = i\,\mathrm{tg}\,\alpha_{lm}^{(3)}(h_0 - h_2)$ ($\alpha_{lm}^{(3)}$ are the real or imaginary roots of Eq. (13) if T, T_1 and T_2 in Eq. (13) are replaced respectively by T'', T_1'' and T_2'').

By applying Bessel and Graf addition theorem, we obtain

$$K_n(br_f)\{e^{in\theta_f}, \cos n\theta_f\}$$

$$= \sum_{j=-\infty}^{\infty} [\delta_{1s}(-1)^j + \delta_{2s}] K_{n+j}\left(b \begin{matrix} r_{ef} \\ r_f \end{matrix}\right) K_j\left(b \begin{matrix} r_e \\ r_{ef} \end{matrix}\right) \cdot$$

$$\{e^{in\theta_{fe} + ij(\theta_{ef} - \theta_e)}, \cos[\, j\theta_e - n\pi - (j+n)\theta_{ef}\,]\} \quad \left(\begin{matrix} \infty > r_{ef} \geq r_e \geq a_e \\ \infty > r_e \geq r_{ef} \geq a_e \end{matrix} \right) \tag{23}$$

where b represents a general parameter. Eq.(23) is used to interchange cylindrical coordinates. It is easy to verify that the items $P_{nl}^{(1)}(r_e, z)$ in Eq .(18), $P_{nl}^{(2)}(r_1, z)$ in Eq. (19) and $P_{nl}^{(3)}(r_2, z)$ in Eq.(21) are orthogonal in three domains along z axis $0 \leqslant z \leqslant h$, $0 \leqslant z \leqslant h_1$ and $h_2 \leqslant z \leqslant h$ respectively . By means of the method of eigenfunction expansion which was once used successfully in similar problems in the uniform ocean[6] ,we can easily get full algebraic equations to determine all unknown coefficients .

For analyzing the possible model on second order radiation condition, we rewrite the governing equations for the second order potential as follows

$$\varphi_{snm}^{\pm} = \varphi_{snm}^{\pm L} + \varphi_{snm}^{\pm F}, \quad E_{nm}^{\pm} = E_{nm}^{\pm(i,s)} + E_{nm}^{\pm(s,s)},$$

$$G_{nm}^{\pm} = G_{nm}^{\pm(i,s)} + G_{nm}^{\pm(s,s)}, \quad H_{nm}^{\pm} = H_{nm}^{\pm(i,s)} + H_{nm}^{\pm(s,s)} \tag{24}$$

$$\nabla^2(\varphi_{snm}^{\pm L}, \varphi_{snm}^{\pm F}) = 0 \quad (\nu_1 + \nu_2 + \nu_3) \tag{25}$$

$$g\,\frac{\partial}{\partial z}(\varphi_{snm}^{\pm L}, \varphi_{snm}^{\pm F}) - (\Omega_{nm}^{\pm})^2(\varphi_{snm}^{\pm L}, \varphi_{snm}^{\pm F}) = (E_{nm}^{\pm(i,s)}, E_{nm}^{\pm(s,s)}) \quad (z = h) \tag{26}$$

$$(\rho_1 - \rho_2)[g\frac{\partial}{\partial z}(\varphi_{snm}^{\pm L}, \varphi_{snm}^{\pm F}) - (\Omega_{nm}^{\pm})^2(\varphi_{snm}^{\pm L}, \varphi_{snm}^{\pm F})]\Big|_{z=h_0-0}$$
$$= (G_{nm}^{\pm(i,s)} - \rho_1 g H_{nm}^{\pm(i,s)}, G_{nm}^{\pm(s,s)} - \rho_1 g H_{nm}^{\pm(s,s)}) \tag{27}$$

$$\frac{\partial}{\partial z}(\varphi_{snm}^{\pm L}, \varphi_{snm}^{\pm F}) = 0 \qquad (S_0) \tag{28}$$

$$\frac{\partial}{\partial n}\varphi_{snm}^{\pm F} = -\frac{\partial}{\partial n}(\varphi_{snm}^{\pm L} + \varphi_{inm}^{\pm}) \qquad (S_b) \tag{29}$$

where $E_{nm}^{\pm(i,s)}$, $G_{nm}^{\pm(i,s)}$ and $H_{nm}^{\pm(i,s)}$ refer, respectively, to the cross products containing first potentials $\varphi_m^{i,\pm}$ and φ_n^s , while $E_{nm}^{\pm(s,s)}$, $G_{nm}^{\pm(s,s)}$ and $H_{nm}^{\pm(s,s)}$, respectively, to the cross products containing φ_n^s and $\varphi_m^{s,\pm}$. It is appropriate to approximate Laplace equation by[7]

$$\nabla^2(\varphi_{snm}^{\pm L}, \varphi_{snm}^{\pm F}) = o(r^{-1/2}) \qquad (k_n r >> 1) \tag{30}$$

In terms of Eq. (25)—(30), we get the asymptotic solutions of $\varphi_{snm}^{\pm L}$ and $\varphi_{snm}^{\pm F}$ for large r as

$$\varphi_{snm}^{\pm L} \sim r^{-1/2}\left(\begin{matrix} L_1^{\pm}(\theta) \\ M_1^{\pm}(\theta) \end{matrix} \right) \cosh[k_n(1 \pm 2b_{nm}\cos\theta + b_{nm}^2)^{1/2} z]\, e^{irk_n(1 \pm b_{nm}\cos\theta)}$$

$$\left(\begin{matrix} h \geq z > h_0 \\ h_0 \geq z > 0 \end{matrix}, k_n r >> 1 \right) \tag{31}$$

$$\varphi_{snm}^{\pm F} \sim r^{-1/2}\begin{pmatrix} L_2^{\pm}(\theta) \\ M_2^{\pm}(\theta) \end{pmatrix} \cosh k_{nm}^{\pm} z\, e^{ik_{nm}^{\pm} r} \qquad \begin{pmatrix} h \geq z > h_0 \\ h_0 \geq z > 0 \end{pmatrix}, k_n r >> 1 \tag{32}$$

where $b_{nm} = k_m / k_n$, $L_t^{\pm}(\theta)$ and $M_t^{\pm}(\theta)(t = 1,2)$ may be determined by using asymptotic forms of Eq. (26) and Eq. (27) respectively. Obviously, it is appropriate to take Eq. (31)—(32) as a possible and proper radiation condition model for second order scattered potential. From this model, we can see that, at a large distance, the second scattered wave in the two-layer ocean behaves the way similar to that in the uniform ocean.

3 Integral Solutions to Second Order Scattered Wave Loads

Due to second order radiation condition and nonlinear conditions on free and stratified flow surfaces, it is difficult to get a direct solution to $\varphi_{snm}^{\pm}$. Through the application of Green's second identity, the second order wave loading components due to the second order scattered potential are still able to be determined in terms of free surface, stratified flow surface and structural integrals involving the first order potential, the second order incident potential and the linear assisting potential[7]. The second order scattered wave loads $F_{nmij}^{\pm}$ on the body may have the following expression

$$F_{nmij}^{\pm} = C_{nm}^{\pm} \iint_{S_b} \rho \varphi_{snm}^{\pm} n_{ij}\, \mathrm{d}s = C_{nm}^{\pm} I_{nmij}^{\pm} \tag{33}$$

where $C_{nm}^{\pm}$ is a complex constant, n_{ij} the component of the unit normal vector pointing to the cylinder surface, $i = 1$ and $j = 1, 2$ correspond to the horizontal wave force and moment respectively, $i = 2$, $j = 1$, 2 the vertical wave force and moment respectively. Introducing the sum- and difference- frequency assisting potentials $\psi_{nmij}^{\pm}$ governed by

$$\nabla^2 \psi_{nmij}^{\pm} = 0 \qquad (\nu_1 + \nu_2 + \nu_3) \tag{34}$$

$$g \frac{\partial}{\partial z} \psi_{nmij}^{\pm} - (\Omega_{nm}^{\pm})^2 \psi_{nmij}^{\pm} = 0 \quad (z = h) \tag{35}$$

$$\frac{\partial}{\partial z} \psi_{nmij}^{\pm} = 0 \qquad (S_0) \tag{36}$$

$$\rho \left[g \frac{\partial}{\partial z} \psi_{nmij}^{\pm} - (\Omega_{nm}^{\pm})^2 \psi_{nmij}^{\pm} \right] \Big|_{z = h_0 - 0}^{z = h_0 + 0} = 0 \tag{37}$$

$$\frac{\partial}{\partial z} \psi_{nmij}^{\pm} \Big|_{z = h_0 + 0} - \frac{\partial}{\partial z} \psi_{ijnm}^{\pm} \Big|_{z = h_0 - 0} = 0 \tag{38}$$

$$\lim_{r_e \to \infty} \sqrt{r_e} \left(\frac{\partial}{\partial r_e} \psi_{nmij}^{\pm} - ik_{nm}^{\pm} \psi_{nmij}^{\pm} \right) \to 0 \tag{39}$$

$$\frac{\partial}{\partial r_e} \psi_{nmij}^{\pm} = \delta_{1i} \delta_{1t} [1 + (z - 1)\delta_{2j}] \cos\theta_e \qquad (S_{re};\ t = 0,1) \tag{40}$$

$$\frac{\partial}{\partial z} \psi_{nmij}^{\pm} = \delta_{2i} [\delta_{1j} + \delta_{2j} r_e \cos\theta_e] \qquad (S_{ve};\ t = 0,1) \tag{41}$$

where S_{re} and S_{ve} denote the radial and vertical surfaces of the e-th (e =1,2) cylinder respectively, t =1 if the wave loading components on the e-th cylinder are taken account into the total wave loads and otherwise t = 0. For example, we may have that i=1, j = 2 and t = 0 when e = 1 and t =1 when e = 2, if only the horizontal wave force on a single platform (cylinder 2) needs to be evaluated. Greens integral identity for $\varphi^{\pm}_{snm}$ and $\psi^{\pm}_{nmij}$ gives

$$
\begin{aligned}
I^{\pm}_{nmij} &= \sum_{e=1}^{2} \iint_{S_{re}+S_{we}} \rho \varphi^{\pm}_{snm} n_{ij} \, \mathrm{d}s \\
&= \iiint_{V_1+V_2+V_3} \rho(\varphi^{\pm}_{snm} \nabla^2 \psi^{\pm}_{nmij} - \psi^{\pm}_{nmij} \nabla^2 \varphi^{\pm}_{snm}) \, \mathrm{d}v - \\
&\quad \sum_{e=1}^{2} \iint_{S_{re}+S_{we}} \rho \frac{\partial \varphi^{\pm}_{inm}}{\partial n} \psi^{\pm}_{nmij} \, \mathrm{d}s + \iint_{S_0+S_\infty+S_f+S_i} \rho(\psi^{\pm}_{nmij} \frac{\partial \varphi^{\pm}_{snm}}{\partial n} - \frac{\partial \psi^{\pm}_{nmij}}{\partial n} \varphi^{\pm}_{snm}) \, \mathrm{d}s \\
&= -\sum_{e=1}^{2} \iint_{S_{re}+S_{we}} \rho \frac{\partial \varphi^{\pm}_{inm}}{\partial n} \psi^{\pm}_{nmij} \, \mathrm{d}s + \rho_1 g^{-1} \iint_{S_f} \psi^{\pm}_{nmij} E^{\pm}_{nm} \, \mathrm{d}s - [g/(\Omega^{\pm}_{nm})^2 (\rho_2 - \rho_1)] \cdot \\
&\quad \iint_{S_i} \left[(\rho_2 - \rho_1) \frac{\partial \psi^{\pm}_{nmij}}{\partial z} G^{\pm}_{nm} + \rho_1 \rho_2 g^{-1} (\Omega^{\pm}_{nm})^2 \psi^{\pm}_{nmij} \Big|^{z=-h_0+0}_{z=-h_0-0} \right] \mathrm{d}s
\end{aligned}
\tag{42}
$$

where $n_{ij} = \frac{\partial}{\partial n} \psi^{\pm}_{nmij}$, S_∞, S_f and S_i denote the vertical circular cylindrical surface at large r, free surface and mean interface of the two fluid layers, respectively. It is easily verified by the method of stationary phase that the integral over S_∞ vanishes as $r^{-1/2} e^{i\lambda r}$. In Eq. (42), only $\psi^{\pm}_{nmij}$ is regarded as unknown potential, needed to be given an appropriate solution. By using the method of eigenfunction expansion again, we have

$$
\psi^{\pm(1)}_{nmij} = \sum_{e=1}^{2} \sum_{n_1=0}^{\infty} \sum_{l=0}^{\infty} (a^{(1,e)}_{nmij,n_1 l} \cos n_1 \theta_e + b^{(1,e)}_{nmij,n_1 l} \sin n_1 \theta_e) g^{(1)}_{n_1 l}(r_f, z) \tag{43}
$$

$$
g^{(1)}_{n_1 l}(r_f, z) = K_{n_1}(\alpha^{(1)\pm}_{lnm} r_f) \cos \alpha^{(1)\pm}_{lnm} z f_1(\Omega^{\pm}_{nm}, i\alpha^{(1)\pm}_{lnm}, z) \tag{44}
$$

$$
\begin{aligned}
\psi^{\pm(2)}_{nmij} &= \sum_{n_1=0}^{\infty} \sum_{l=0}^{\infty} (a^{(2)}_{nmij,n_1 l} \cos n_1 \theta_1 + b^{(2)}_{nmij,n_1 l} \sin n_1 \theta_1) g^{(2)}_{n_1 l}(r_1, z) + \\
&\quad \delta_{2i} [\delta_{1j} (2z^2 - r_1^2) / 4h_1 \delta_{2j} (4r_1 z^2 - r_1^3)] \cos n_2 \theta_1 \\
&\quad (n_2 = \delta_{ij} + (1 - \delta_{ij}) \delta_{2j})
\end{aligned}
\tag{45}
$$

$$
\begin{aligned}
g^{(2)}_{n_1 l}(r_1, z) &= \delta_{1c} [\delta_{0l} r_1^{n_1} + 2(1 - \delta_{0l}) I_{n_1}(l\pi h_1^{-1} r_1)] \cos l\pi h_1^{-1} z + \\
&\quad (\delta_{2c} + \delta_{3c}) \, g_2(z) I_{n_1}(\alpha^{(2)\pm}_{lnm} r_1)
\end{aligned}
\tag{46}
$$

$$\psi_{nmij}^{\pm(3)} = \sum_{n_1=0}^{\infty}\sum_{l=0}^{\infty} g_{n_1 l}^{(3)}(r_2,\theta_2,z) + \delta_{2i}\{\delta_{1j}[z-h+g/(\Omega_{nm}^{\pm})^2] + \delta_{2j}[r_2(z-h)+gr_2/(\Omega_{nm}^{\pm})^2]\}\cos n_2\theta_2 \quad (47)$$

$$g_{n_1 l}^{(3)}(r_2,\theta_2,z) = \delta_{3c}h_{n_1 l}(\mu_{1nm}^{\pm},r_2,\theta_2,z) + (\delta_{1c}+\delta_{2c})g_3(z)h_{n_1 l}(\alpha_{1nm}^{(3)\pm},r_2,\theta_2,z) \quad (48)$$

$$h_{n_1 l}(b,r_2,\theta_2,z) = [(a_{nmij,n_1 l}^{(3)}\cos n_1\theta_1 + b_{nmij,n_1 l}^{(3)}\sin n_1\theta_1)I_{n_1}(br_2) + (c_{nmij,n_1 l}^{(3)}\cos n_1\theta_1 + d_{nmij,n_1 l}^{(3)}\sin n_1\theta_1)K_{n_1}(br_2)]\cos b(z-h_2) \quad (49)$$

where $\psi_{nmij}^{\pm(k)}$ represents the assisting potential in subregion v_k, $a_{nmij,n_1 l}^{(1,e)}, b_{nmij,n_1}^{(1,e)}, a_{nmij,n_1 l}^{(k)}$, $b_{nmij,n_1 l}^{(k)}$, $c_{nmij,n_1 l}^{(3)}$ and $d_{nmij,n_1 l}^{(3)}$ are all unknown coefficients, and b is a general parameter. In Eq.(44), we have that $\alpha_{0nm}^{(1)\pm} = -ik_{nm}^{\pm}$, $\alpha_{lnm}^{(1)\pm}(l\neq 0)$ are the imaginary roots of Eq. (13) ($\omega = \Omega_{nm}^{\pm}$). In Eqs. (46)—(48), $\mu_{lnm}^{\pm}$ tg $\mu_{lnm}^{\pm}(h-h_2) = -(\Omega_{nm}^{\pm})^2/g$, $g_2(z)$ and $g_3(z)$ have the same mathematical forms as $f_2(z)$ and $f_3(z)$ in Eq. (20)—(22) where parameters ω_m , $\alpha_{lm}^{(k)}$ and β_{lm} should be replaced by $\Omega_{nm}^{\pm}$, $\alpha_{lnm}^{(k)\pm}$ and $\beta_{lnm}^{\pm}$ respectively. For interchanging different cylindrical coordinates , we may develop Graf's addition theorem as[8]

$$K_{n_1}^{(q)}(br_f)T(n_1\theta_f) = \sum_{j=-\infty}^{\infty}[\delta_{1q}(-1)^j + \delta_{2q}]K_{n_1+j}^{(q)}\left(b\ \ r_{ef}\right)K_j^{(q)}\left(b\ \ r_e\right)\cdot T[j\theta_e - n_1\pi - (j+n_1)\theta_{ef}] \quad \begin{pmatrix}\infty > r_{ef}\geq r_e \geq a_e\\ \infty > r_e \geq r_{ef}\geq a_e\end{pmatrix} \quad (50)$$

where $T(x)$ denotes $\sin x$ or $\cos x$. By taking the series expansion steps similar to those in finding the solution to the first order potential, we may readily give the full algebraic equations to determine all unknown coefficients .

Now, for evaluating $F_{nmij}^{\pm}$, we have to face the problems, which we have faced in the numerical computation of second order scattered wave loads in the uniform ocean, of slowly convergent integrals over the free and stratified surfaces. For convenience, we only consider the horizontal wave force on a single vertical circular cylinder. From Eq.(16) and Eq. (43), the first order potential and the assisting potential ($i=1$, $j=1$) about a single cylinder are given as

$$\varphi_m^{(1)} = \varphi_m^{i(1)} + \varphi_m^{s(1)} = \sum_{n=0}^{\infty}(2-\delta_{0n})i^{n+1}(k_m\omega_m)^{-1}A_m\cosh k_m h f_1(\omega_m,k_m,z)\cosh k_m z\cdot [J_n(k_m r) - \frac{J_n'(k_m a)}{H_n^{(1)'}(k_m a)}H_n^{(1)}(k_m r)]\cos n\theta \quad (51)$$

$$\psi_{nm11}^{\pm(1)} = \sum_{l=0}^{\infty} a_{lnm}^{\pm}K_1(\alpha_{lnm}^{\pm}r)\cos\alpha_{lnm}^{\pm}z f_1(\Omega_{nm}^{\pm}, i\alpha_{lnm}^{\pm}, z)\cos\theta \quad (52)$$

We may express, respectively, integral over s_f (second item of Eq. (42)) and integral over s_i (third item of Eq. (42)) as the sums of a series of infinite integrals, whose integrands contain triple products of

Bessel and Hankle functions , as follows

$$\begin{pmatrix} I_{nm}^{\pm(sf)} \\ I_{nm}^{\pm(sf)} \end{pmatrix} = \sum_{l=0}^{\infty} \begin{pmatrix} D_{nm,l}^{\pm} \\ Q_{nm,l}^{\pm} \end{pmatrix} \sum_{e=0}^{\infty} [\begin{pmatrix} a_{nm,e}^{\pm} \\ g_{nm,e}^{\pm} \end{pmatrix} S_{nm}^{\pm(e,1)} + \begin{pmatrix} a_{mn,e}^{\pm} \\ g_{mn,e}^{\pm} \end{pmatrix} S_{mn}^{\pm(e,1)} + \begin{pmatrix} b_{nm,e}^{\pm} \\ h_{nm,e}^{\pm} \end{pmatrix} (S_{nm}^{\pm(e+1,1)} + S_{nm}^{\pm(e-1,1)}) + \begin{pmatrix} b_{mn,e}^{\pm} \\ h_{mn,e}^{\pm} \end{pmatrix} (S_{mn}^{\pm(e+1,1)} + S_{mn}^{\pm(e-1,1)}) + \begin{pmatrix} c_{nm,e}^{\pm} \\ i_{nm,e}^{\pm} \end{pmatrix} T_{e,1}^{\pm} + \begin{pmatrix} d_{nm,e}^{\pm} \\ j_{nm,e}^{\pm} \end{pmatrix} (T_{e+1,1}^{\pm} + T_{e-1,1}^{\pm}) + \begin{pmatrix} e_{nm,e}^{\pm} \\ k_{nm,e}^{\pm} \end{pmatrix} T_{e+1,-1}^{\pm} + \begin{pmatrix} f_{nm,e}^{\pm} \\ l_{nm,e}^{\pm} \end{pmatrix} (T_{e,-1}^{\pm} + T_{e+2,-1}^{\pm})] \tag{53}$$

$$S_{nm}^{\pm(e,f)} = \int_1^{\infty} H_{e+f}^{(1)}(k_n ar) H_e^{(1),\pm}(k_m ar) K_f(\alpha_{lnm}^{\pm} ar) r \, \mathrm{d}\, r \tag{54}$$

$$T_{e,f}^{\pm} = \int_1^{\infty} H_{e+f}^{(1)}(k_n ar) J_e(k_m ar) K_f(\alpha_{lnm}^{\pm} ar) r \, \mathrm{d}\, r \tag{55}$$

where $D_{nm,l}^{\pm}, Q_{nm,l}^{\pm}, a_{nm,l}^{\pm} \sim l_{nm,l}^{\pm}$ are all known coefficients, $H_e^{(1)}(x)$ is the third kind of Bessel function or Hankle function and $H_e^{(1),+}(x) = H_e^{(1)}(x) = [H_e^{(1),-}(x)]^* = [H_e^{(2)}(x)]^*$. Introducing a general integral as

$$I_{e,f}(a,b,c,t) = \int_1^t X_e^{(1)}(ar) X_f^{(2)}(br) X_{e+f}^{(3)}(cr) r \, \mathrm{d}\, r \tag{56}$$

where a, b, c and t are general parameters, $X_e^{(j)}(x)$ denotes the j-th kind of e-th order Bessel function. Obviously, with proper values for the parameters$a$, b and$c$ and proper forms for $X_e^{(j)}(x)$, the general integral $I_{e,f}$ may be reduced to $S_{mn}^{\pm(e,f)}$ or $T_{e,f}^{\pm}$ as $t \to \infty$. By using the recurrence formulas of the derivative of general Bessel function and the method of integration by parts, we may have

$$\begin{aligned} I_{e,f} &= C_{e,f}^{(1)} + (a^2 + c^2 - b^2) I_{e-1,f} / ac - I_{e-2,f} \\ &= C_{e,f}^{(2)} + (b^2 + c^2 - a^2) I_{e,f-1} / bc - I_{e,f-2} \end{aligned} \tag{57}$$

$$I_{1,0} = \frac{1}{2}\left(C_{1,0}^{(1)} + \frac{a^2 + c^2 - b^2}{ac} I_{0,0} \right), \quad I_{0,1} = \frac{1}{2}\left(C_{0,1}^{(2)} + \frac{b^2 + c^2 - a^2}{bc} I_{0,0} \right) \tag{58}$$

$$C_{e,f}^{(1)} = (ac)^{-1}[aU_{e,f} - cU_{e-1,f} + bV_{e-1,f-1}] \tag{59}$$

$$C_{e,f}^{(2)} = (bc)^{-1}[bU_{e,f} - cU_{e,f-1} + aV_{e-1,f-1}] \tag{60}$$

$$U_{e,f}(a,b,c,t) = X_e^{(1)}(a) X_f^{(2)}(b) X_{e+f-1}^{(3)}(c) - tX_e^{(1)}(at) X_f^{(2)}(bt) X_{e+f-1}^{(3)}(ct) \tag{61}$$

$$V_{e,f}(a,b,c,t) = X_e^{(1)}(a) X_f^{(2)}(b) X_{e+f+1}^{(3)}(c) - tX_e^{(1)}(at) X_f^{(2)}(bt) X_{e+f+1}^{(3)}(ct) \tag{62}$$

By using the above recurrence relations , the integral $S_{mn}^{\pm(e,f)}$ or $T_{e,f}^{\pm}$ can be easily evaluated only by getting the values of $S_{mn}^{\pm(0,0)}$ and $T_{0,0}^{\pm}$, which may be calculated by an asymptotic method or some special integrals[6,9]. For the general type of vertical circular cylinders (shown in Fig. 1), the same analyzing results relating to integrals overs_r and s_i inv_1 may be gotten if a suitable integral line is given.

4 Conclusions

(1) By taking a basic model of stratified ocean—two-layer ocean model and applying the theories of Stokes multicolored waves , the paper analyzes the problems about the effects of scattered wave on general vertical circular cylinder or multiple cylinders in the stratified ocean, the wave interference due to multiple cylinders and the radiation conditions on the nonlinear diffracted wave.

(2) By using the asymptotic method, a proper expression for second order wave radiation condition is presented and verified to replace the weak model.

(3) Applying Greens integral identity, an analytical integral solution is given to evaluate second order scattered wave loads on the general type of vertical circular cylinders in the two-layer ocean and compared with that for the uniform ocean.

(4) A simplified method of evaluating the slowly convergent integral is given and the special recurrence formulas, similar to those for the uniform ocean, for infinite integrals over free and stratified surfaces are derived.

Acknowledgements

The work is supported by the National Natural Science Foundation of China (19802023).

References

[1] Yih C S (1980) Stratified flows . New York, Academic Press, Inc., 237 ~ 241.

[2] Wu Jianhua, Wu Xiuheng,Li shimo (1989) Theories of wave diffraction and scattering caused by large scale bodies in stratified ocean (I). *J. of Hydrodynamics*, **4** (2) 81 ~ 88.

[3] Turner, T S (1979) Buoyancy effects in fluids. London, Syndies of the Cambridge Univ. Press, 48 ~ 57.

[4] Wu Jianhua,Wu Xiuheng,Li Shimo (1991) Theories of wave diffraction and scattering caused by large scale bodies in stratified ocean (IV). *J. of Hydrodynamics*, **6** (3) 46 ~ 53.

[5] Wu Jianhua (1991) The Second Order Wave Loads in the Stratified Ocean.*Acta Mechanica Sinica*,**7** (1) 1~4.

[6] Huang Hua, Zhang Diming , Sun Mingguang (1996) A practical method evalnating the finite amplitude wave forces on vertical compound circular cylinders. *Acta Scientiarum Naturalium Universitatis Sunyatseni*, **35** (5) 33 ~ 38.

[7] Mei Qiang zhong (1983) The applied dynamics of ocean surface waves. New York, A Wiley-Interscience Publication, 657 ~ 667.

[8] Huang Hua, Luo Zhigao, Sun Mingguang et al. (1999) Nonlinear wave loads on large scale circular cylinders.*Tropic Oceanology*, **18** (4) 24 ~ 31.

[9] Wu Jianhua,Fang Ying (1992) On the numerical evaluation of the second order wave diffraction loads in regular sea. *Proc. of 7th Intl. workshop on Water Waves and Floating Bodies.* France, Val de Reuil, 24 ~ 27.

Analysis of the Sea Fog in the Sea Around the Great Wall Station, Antarctica

Huang Yaorong（黄耀荣），Xue Zhenhe（薛振和）
National Research Center for Marine Forecasts, Beijing 100081

Abstract The synoptic analysis of sea fog in western Antarctic sea region is made based on the observation data in the Chinese Antarctic station, Great Wall Station, from December 1994 to November 1995, and the facsimile weather charts issued by Chile. It is found that more than 90% fog in this region is the advection cooling fog. Also, the synoptic mechanism of the fog creation and distinction is discussed by analyzing the pressure field, the temperature field and the upper-level stratification. Finally, the focus of attention in forecasting fog is pointed out.

Keywords western Antarctic seas, advection cooling fog, temperature inversion

1 Introduction

Sea fog is one of the important weather disasters in polar regions. For lack of marine weather records in the Antarctic, it is difficult to study Antarctic weather , especially the sea fog there.

In recent ten-odd years, meteorologists both in China and abroad have carried out some studies on Antarctic sea fog. Wang Binhua gave a concise discussion on the sea fog in the Southern Ocean in his book, *Sea fog*. Schwerdtfeger made some statistics of the relation between the creation of sea fog and the sea-air temperature difference and the wind speed variation in the area south of 60°S in southern Atlantic Ocean. Peng Bangan analyzed the sea fog in the Maxwell Bay, and so on. However, those studies mentioned above rarely deal with the synoptic mechanism. Based on the statistics, emphasis is laid on analyzing the synoptic mechanism in this paper to find out the synoptic mechanism of the creation and extinction of the sea fog in the Antarctic, and to have a better way to forecast sea fog.

2 Monthly analysis of the sea fog days in western Antarctic seas

Great Wall Station, a Chinese Antarctic research station, is situated at 62°12' S, 58°57' W, in King George Island in western Antarctica. The island is small with a low elevation. As a year-round weather and marine station, the observatory of Great Wall Station is at seashore, 10 m above sea level, suitable for observation and research. Based on the observation data there from December 1994 to November 1995, monthly analysis of foggy days is made in this paper, and the result is shown in Table 1.

Tab. 1 Monthly distribution of foggy days in Great Wall Station from December 1994 to November 1995

Month	Jan.	Feb.	Mar.	Apr.	May	Jun.	Jul.	Aug.	Sep.	Oct.	Nov.	Dec.	total
Foggy days	18	11	7	8	3	1	1	5	4	7	13	14	89

It can be seen from Table 1 that 88% of the foggy days in Great Wall Station are concentrated from October to April of the next year, mostly in November, December, January and February. The total

number in the four months is 56 days, taking 63% of the yearly foggy days and 47% of the summer foggy days, or taking about half of the summer days. This indicates that there is obviously some relation between the fog and the active warm air caused by the southward movement of the polar front in the Southern Hemisphere during summer.

3 The relation between sea fog and field of wind

During the summer expedition it came into our notice that the dense fog always comes from the west coast and it remains even when the wind speed is high. The relation between foggy days and wind direction and speed is counted statistically (Table 2).

Tab. 2 The relation between sea fog and field of wind in the Great Wall Station

Wind direction	Foggy days (wind 0)	Foggy days (wind 1-2)	Foggy days (wind 3-4)	Foggy days (wind 5-6)	Foggy days (wind≥7)	Total foggy days	Percentage of TFD
C							
N		1	1	5		7	8%
NW		2	28	26	3	59	66%
W		3	6	8		17	19%
SW							
W							
SE		1	1			2	2%
E		2	2			4	5%
NE							
total		9	38	39	3	89	
Percentage of TFD		10%	43%	44%	3%		100%

* TFD stands for the total foggy days.

It can be seen from Table 2 that the sea fog there well correlates with the field of wind. As to the relation between fog and wind direction, the total foggy days in the year are 89 days, and 93% of them with wind directions of N, NW and W, among which, NW, including WNW and NNW, is the one with the most foggy days, taking 66%. In addition, there are a few foggy days with the wind directions from E to SE when the wind is weak. There are also a few foggy days with light fog and precipitation when the wind is weak, taking about 7% of the total foggy days. This indicates that the sea fog has a close relation with the warm and wet air from the low-latitude area, or from the direction of northwest, which is a significant characteristic of the advection cooling fog. As to the relation between sea fog and wind speed, most sea fog there occurs when wind speed is from 3 to 6 on the Beaufort scale, about 87% of the total foggy days, especially 44% with wind speed of 5 to 6 on the Beaufort scale. Foggy days with strong wind of 7 or more on the Beaufort scale are three days. That is different from the fog in coastal China, where fog occurs with wind measuring 4 or less on the Beaufort scale. It is clear from the discussion above that most of the fog there is advection cooling fog; a little strong wind is favorable for the transportation of the warm and wet air, hence the forming and maintaining of the sea fog. However, excessively strong wind is not favorable and there is never fog with wind measuring 8 or more on the Beaufort scale in the Great Wall Station, because it is not favorable for the gathering of saturated air, much less the forming of fog.

4 The relation between sea fog and field of temperature and humidity

Figure 1 is the element profile of temperature, dew point, pressure, wind and weather in the Great Wall Station in January 1995. It can be seen from Figure 1 that, (1) Sea fog often occurs at the stage of continuous high temperature and high humidity ($1^{st}-2^{nd}$, $9^{th}-12^{th}$, $19^{th}-30^{th}$), being dense and long-lasting, which is the characteristic of the advection cooling fog. (2) Sea fog often forms in the period when depression of the dew point ($t - t_d$) is decreasing ($19^{th}-30^{th}$), disappears in the period when depression of the dew point is increasing (after 30^{th}). All 89 foggy days in the year are with the depression of the dew point less than 2℃ (Table 3).

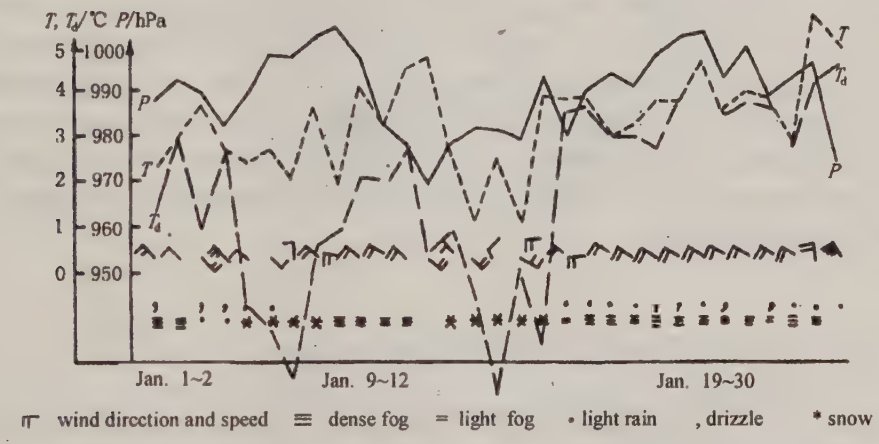

Fig. 1 Element profile of temperature, dew point, wind and weather in January 1995

Tab. 3 The distribution of foggy days with different depressions of the dew point

kind	$T-T_d=0\sim1$ ℃	$T-T_d=1.1\sim2$ ℃	Sum (d)	Percentage (%)
Dense fog	54	10	64	71
Light fog with precipitation	24	1	25	29
Sum	78	11	89	
Percentage (%)	88	12		100

It can be seen from Table 3 that foggy days with $t - t_d \leqslant 1$ ℃ take 88% of the total foggy days, densely foggy days take 71%, lightly foggy days with precipitation take only 29%. Then does fog definitely occur when $t-t_d \leqslant 2$℃? Table 4 gives the answer.

Tab. 4 The occurrence of fog with different depressions of the dew point

Kind	$T-T_d=0\sim1$ ℃	$T-T_d=1.1\sim2$ ℃	Total days	Percentage of total observation days (%)
Dense fog with precipitation	68	10	78	5
No fog with precipitation	49	16	65	45
No fog without precipitation		2		1
Total days	117	28	145	100

It can be seen from Table 4 that when $t - t_d \leqslant 2^{\circ}$, only 54% of the days are with fog, 45% without fog and with precipitation, 1% with neither fog nor precipitation. Then how to tell fog from precipitation ? It can be seen from the following discussion that fog always occurs with a near-ground inversion layer that distinguishes between sea fog and precipitation. Sea fog disappears when the pressure decreases, which is just the time when the high pressure ahead moves eastwards or the blocking high collapses.

5 The relation between sea fog and field of pressure

Figure 2 shows a typical baric topography of NW wind bringing fog. It can be seen from Figure 2 that the subtropical high in southwestern Atlantic Ocean develops rapidly southwards, with its center reaching 45°S. Its ridge extends southwestwards to the Antarctic Peninsula and becomes a stationary blocking high. Two frontal cyclones from the sea southeast of New Zealand move to the northwest of the ridge and slow down at the Drake Passage. The northwest stream, which is behind the ridge and in front of the trough, is prevailing at the Great Wall Station. Then a weather process of dense fog lasts about ten days. Therefore, the blocking high in southwestern Atlantic Ocean is an important weather system for the forming of fog. It works in two ways, (1) to block the frontal cyclone following it; (2) to transport warm and wet air from the low latitude area.

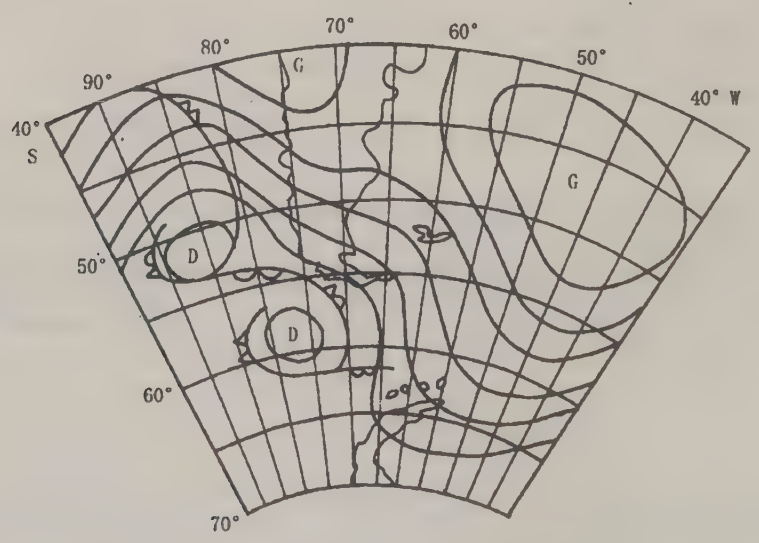

Fig. 2 The baric topography with NW wind and fog (surface, January 21, 1995)

Another important weather system, which creates fog, is the baroclinic frontal cyclone following the blocking high. It also brings a great deal of warm and wet air or transports the warm and wet air. Both transporting mechanisms, the blocking high and the frontal cyclone, create the advection cooling fog in the Great Wall Station.

Figure 3 gives a situation, in which southeast wind brings fog. The polar high extends northwards, forming a ridge in the Antarctic Peninsula, together with the cyclone back in the Weddell Sea, bringing

SE wind to the Great Wall Station and light fog with precipitation. Obviously, it is the advection evaporation fog. This kind of fog will not be dealt with too much in this paper because of its low density, short-lasting time and low probability of occurrence.

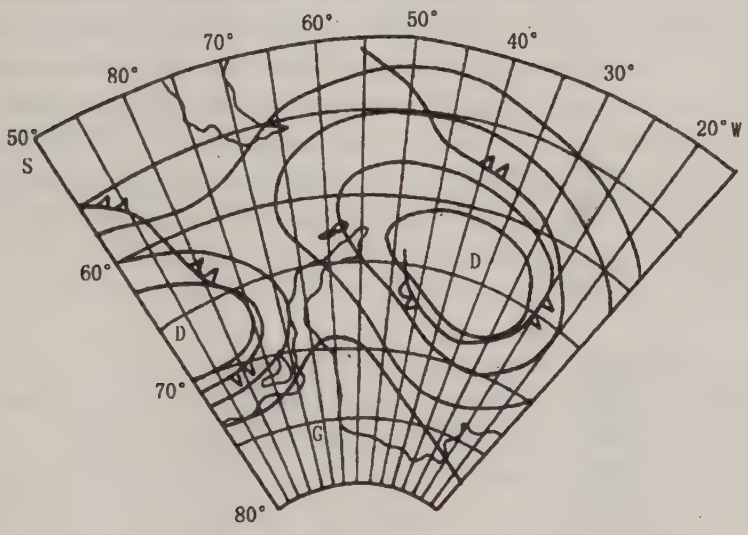

Fig. 3 The situation with ESE wind and fog (surface, November 24,1995)

6 The high-level stratification of advection cooling fog

The stream-field and temperature-humidity-field characteristics creating the advection cooling fog in the seas around the Great Wall Station is analyzed as above. Table 5 shows the high-level stratification, in which the fog occurs.

Tab. 5 The day-by-day distribution of the height of the near-ground inversion layer at the Bellingshauseng Station (2 km away from the Great Wall Station) January 18th ~ 30th 1995

Date	18	19	20	21	22	23	24
Inversion thickness (m)	0	100 ~ 300	100 ~ 200	100 ~ 200	100 ~ 700	100 ~ 600	100 ~ 2000
Date	25	26	27	28	29	30	31
Inversion thickness (m)	100 ~ 1000	300 ~ 600	100 ~ 400	100 ~ 400	100 ~ 200	100 ~ 200	0

The fog occurring at the Great Wall Station and the seas around from January 19 to 30 1995 is a typical advection cooling one with long lasting time, 12 days, and high density.

It can be seen from Table 5 that the advection inversion layer began on January 19 and lasted until Jan.30, with relatively high thickness. It reached the height of 2000 m (about 700hPa) on January 24. According to the only sounding data available so far, the advection cooling fog there always occurs corresponding to a relatively thick near-ground advection inversion layer. While the advection inversion layer decreased, it broke; as the inversion layer rose, there was a period with the weather mainly

dominated by precipitation; and the inversion layer decreased and decreased. The sea fog disappeared on Jan. 31 when the advection inversion layer disappeared. The advection inversion layer fundamentally corresponds to the advection fog one by one.

Figure 4 is the sounding curves of the weathers with and without fog. It can be seen from the figure that the advection inversion is significant while there is fog , and the inversion layer is thick. Therefore, the occurrence of advection inversion is the key to the occurrence of advection cooling fog. The advection inversion works in two ways, (1) to form a stable stratification, to ensure that the heat is carried downwards to the ocean below, to keep the warm and wet air which is moved horizontally on the sea loosing heat, cooling down, and to keep the moisture condensing; (2) to shield the moisture, because the inversion layer blocks the convection, making the humidity at low level saturated and condensed to form fog. But the height of the inversion layer should be appropriate, for once it lifts it becomes cloud, the fog disappears and there is precipitation.

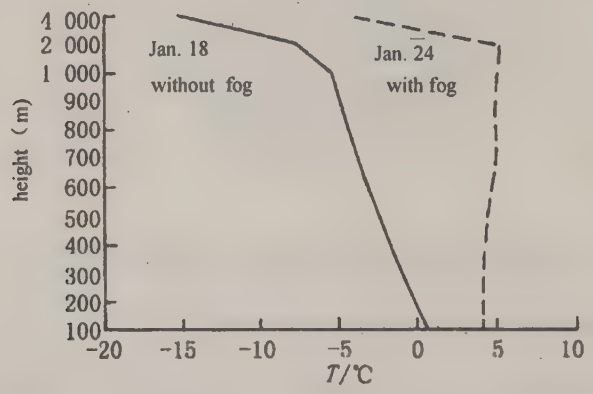

Fig. 4 the sounding curves of January 18 and 24, 1995

7 Discussion and conclusions

(1) Advection cooling fog is prevailing in western Antarctic seas represented by the Great Wall Station during the summer. Its occurrence is mainly due to the warm and wet air moving from the low-latitude area.

(2) The weather systems that bring the warm and wet air there are the high ridge which is extending from South America or southwestern Atlantic Ocean and the cyclone from the sea southeast of New Zealand. Therefore, special attention must be paid to the time of the coming of the two systems to forecast the advection cooling fog there.

(3) As to the field of weather elements, most sea fog there occurs when there are high temperature, high humidity and NW wind measuring 3~6 on the Beaufort scale.

(4) The creation of advection cooling fog has relation with the unique cushion there. When summer begins the polar fronts move southwards, the warm and wet air becomes more active. There is abundant floating ice in the oceans and seas around the continent due to the melting and collapse of the Antarctic ice sheet; beyond the floating ice area is the west wind drift with floating icebergs. Because of the

mixing of water and ice, the SST (sea surface temperature) there is low; the area becomes a cold surface one; the average SST measured during the summer is about 0~2 ℃. Because of the great thermal capacity of the ocean, the sea temperature is a stable factor compared with that of the atmosphere; so it can be taken as a quasi-stationary constant. The quasi-stationary constant cold ocean surface absorbs the heat of the warm and wet air from above, and lowers the temperature of the air, making it reach its dew point, the moisture saturated and become fog. So the station temperature can be calculated with the following formula:

$$\frac{\partial T}{\partial t} = -\bar{v}\frac{\partial T}{\partial n} = -|v|\cos\alpha\frac{\partial T}{\partial n}$$

where, $|v|$ is a scalar of the measured wind, $\frac{\partial T}{\partial n}$ is the temperature gradient on the isobaric surface, α is the angle between the wind direction and the temperature gradient. Then consider the depression of the dew point, when $t - t_d = 0.2 \sim 2$ ℃ and there is a near-ground inversion layer, the judgement of forming fog can be made.

(5) In the summer, because the polar fronts move southwards, and the warm and wet air becomes more active, Antarctic ice sheet melts and collapses, forming a floating ice area around the continent. Beyond the floating ice area is the iceberg drift area, where the SST is very low due to the mixing of water and ice, thus making the oceans and seas around Antarctic continent a cold cushion. When the warm and wet air moves on, the advection cooling fog forms. Therefore, it can be inferred that the advection cooling fog fundamentally prevails in the Antarctic during the summer.

(6) The main weather systems which bring warm and wet air to the seas around the Antarctic continent in the summer are the frontal cyclone and the northly stream of the west side of the blocking high, which is stretching from the mid-latitude area to the high-latitude area, especially the frontal cyclone moving from the mid-latitude area. Therefore, in the Southern Hemisphere during the summer, the sea area of the west side of the blocking high and the area where the cyclone is active are certainly the area where sea fog often occurs.

References

[1] Wang Binhua (1993) Sea Fog, Beijing: China Ocean Press, 15 ~ 35.

[2] Shwerdtfeger W (1984) Weather and Climate of the Antarctic. *Development in Atmospheric Science*, 15: 168 ~ 1853.

[3] Peng Pang'an, Analysis of Sea Fog in the Maxwell Bay, Antarctic. *Collection of Antarctic Scientific Treatises*, Vol. 4, Beijing: China Ocean Press.

[4] Huang Yaorong (1992) Analysis and Research of the Summer Sea Fog in the Drake Passage. *Polar Research*, 4 (2).

Numerical Simulated Study on the Separation of Oblique Incident and Reflected Waves

Shao Limin（邵利民）[1,2], Yu Yuxiu（俞聿修）[1]

1 *State Key Laboratory of Coastal and Offshore Engineering, DUT, Dalian* 116024

2 *Navigation Department of Dalian Naval Academy, Dalian* 116018

Abstract The Goda's method of separating the frequency spectrum of the unidirectional incident and reflected waves is improved. The proposed method can be applied to the separation of oblique incident and reflected waves and the two wave gauges can be arranged in an arbitrary angle in front of a structure. When the projected distance of the two probes on the incident wave direction is the multiple of the half length of the incident waves, the singular problem will emerge by using the method. It is advised that when the projected distance of the two measured points on the incident wave direction is 0.05~0.45 times the wave length of peak frequency wave, good results can be obtained. The simulated resultant waves are separated by the method of numerical simulation and the separated wave spectra are basically corresponding to the target spectra input. The wave trains calculated by the separated incident and reflected wave frequency spectrum are approximated to the input wave trains and the reflected coefficient can be derived correctly. Therefore, the method proposed in this paper is reliable.

Keyword oblique direction, incident wave, reflected wave, frequency spectrum, separated, numerical simulation

Introduction

During the process of the wave propagation from far sea to shoreline, the phenomena such as refraction, diffraction and reflection will occur. It is the base of the design of offshore structures to describe the physical processes. When the shape of sea bank is crag or the offshore structure is vertical, the problem of reflection is more serious. Especially in the half-closed harbor, the multi-reflection of waves will influence the wave states strongly and further the safety of the sailing ships and the stability of the anchoring ships in the harbor are also affected. In addition, the reflection of waves will influence the motion characteristic of sands in harbor and sea bank, which can cause the evolvement of the sea bank shape.

Much research work about the separation of incident and reflect waves has been carried out, such as the work of Kaijima (1969) , Thornton and Calhoun (1972) , Goda and Suzuki (1976) , Morden and Bichy (1976) , Yu Yuxiu (1985) and Fan Qijin(1985). In order to measure synthetic wave elevation, Goda put two wave gauges in a vertical line in front of a structure, and also the frequency spectra of the incident and reflect waves of the normal incidence are separated. Because only two wave gauges are used to measure waves, it is called the two-point method. The FFT method is adopted for the calculation of Fourier coefficient and the method is aimed at the normal incident waves in which the directions of waves are vertical to the structures. Goda indicated that singular phenomena will occur, when the

distance of the two measured points is the multiple of the half wave length of the incident waves. Mansard and Funke(1980) analyzed the characteristics of the incident and reflect waves field and improved the precision of the separation of the incident and reflected waves by using three wave gauges and the least square method, so it is called the three-point method. There are singular problems also in this method and the distances of different measured points are limited to meet some conditions. Zelt and Skjelbreia (1992) invented the multi-points method by extending the Mansard method to the straight line array of multi-probes. Frigaard and Brorsen (1993) separated the incident and the reflected waves of the irregular waves in time domain. Guza, et al.(1984) , Walton, T.L.(1992), Hughes (1993) Zhu Liangsheng and Sui Shifeng (1997) separated the frequency spectra of the incident and reflected waves by using the combination of different wave factors of the single-point method. Huang Peiji (1989), Sun Zhaochen (1999) improved the two-point method and separated the incident and reflected waves of oblique waves in front of a model structure.

The two-point method of Goda is improved and the method to separate the frequency spectra of the unidirectional incident and reflected waves is indicated in this paper. The improved method can be applied to separate the oblique incident and reflected waves and the direction of gauges can be arranged in arbitrary angles. In order to verify the reliability of the new method, the numerical simulated method is adopted to achieve the resultant wave field of the incident and reflected waves. The simulated resultant waves are separated by the method provided and the wave spectra detached are basically corresponding to the target spectra input. Also the wave trains calculated by the frequency spectra of the separated incident and reflected wave are approximate to the input wave trains and the reflected coefficient of the structures are provided preciously. Therefore, the correctness of the separating method is confirmed.

1 Mathematical Model of Separating Oblique Incident and Reflected Waves

According to the method used to describe the unidirectional irregular waves in wave theory, the wave elevation of the oblique incident waves $\eta_i(x,y,t)$ and the reflected waves $\eta_r(x,y,t)$ before the structures can be defined as follows:

$$\begin{cases} \eta_i(x,y,t) = \sum_{m=0}^{\infty} a_{im} \cos(k_m x \cos\theta + k_m y \sin\theta - \omega_m t + \varepsilon_{im}) \\ \eta_r(x,y,t) = \sum_{m=0}^{\infty} a_{rm} \cos(k_m x \cos\theta + k_m y \sin\theta + \omega_m t + \varepsilon_{rm}) \end{cases} \tag{1}$$

In which, a_{im} and a_{rm} are the amplitudes of harmonic wave of the incident and reflected waves, ε_{im} and ε_{rm} are the initial phases of harmonic wave of the incident and reflected waves respectively, x,y are the location coordinates of the measured points, t is the time, θ is the incident angle of wave propagation, k_m and ω_m are the wave number and angular frequency of different component waves and the dispersion relationship between them can be described as follows:

$$\omega_m^2 = k_m g \tanh(k_m d) \tag{2}$$

Where, g is the gravitational acceleration, d is the depth of water. For the convenience of discussion, only a component harmonic wave is considered and the subscript m is omitted, then the synthetic waves combined by the incident and reflected waves are:

$$\begin{aligned}\eta(x,y,t) &= \eta_i(x,y,t) + \eta_r(x,y,t) \\ &= a_i \cos(kx\cos\theta + ky\sin\theta - \omega t + \varepsilon_i) + a_r \cos(kx\cos\theta + ky\sin\theta + \omega t + \varepsilon_r)\end{aligned} \tag{3}$$

In theory, the synthetic wave elevation derived from the first gauge is expressed as:

$$\eta(x_1,y_1,t) = a_i \cos(kx_1\cos\theta + ky_1\sin\theta - \omega t + \varepsilon_i) + a_r \cos(kx_1\cos\theta + ky_1\sin\theta + \omega t + \varepsilon_r) \tag{4}$$

The synthetic wave elevation achieved by the second gauge is:

$$\eta(x_2,y_2,t) = a_i \cos(kx_2\cos\theta + ky_2\sin\theta - \omega t + \varepsilon_i) + a_r \cos(kx_2\cos\theta + ky_2\sin\theta + \omega t + \varepsilon_r) \tag{5}$$

In practice, the synthetic elevation got by the gauge in the first point is:

$$\eta_1 = A_1\cos\omega t + B_1\sin\omega t \tag{6}$$

The synthetic elevation derived by the wave gauge in the second point is:

$$\eta_2 = A_2\cos\omega t + B_2\sin\omega t \tag{7}$$

By comparing formulae (4) and (6) or formulae (5) and (7), the following formula can be achieved:

$$\begin{cases} A_1 = a_i\cos(kx_1\cos\theta + ky_1\sin\theta + \varepsilon_i) + a_r\cos(kx_1\cos\theta + ky_1\sin\theta + \varepsilon_r) \\ B_1 = a_i\sin(kx_1\cos\theta + ky_1\sin\theta + \varepsilon_i) - a_r\sin(kx_1\cos\theta + ky_1\sin\theta + \varepsilon_r) \\ A_2 = a_i\cos(kx_2\cos\theta + ky_2\sin\theta + \varepsilon_i) + a_r\cos(kx_2\cos\theta + ky_2\sin\theta + \varepsilon_r) \\ B_2 = a_i\sin(kx_2\cos\theta + ky_2\sin\theta + \varepsilon_i) - a_r\sin(kx_2\cos\theta + ky_2\sin\theta + \varepsilon_r) \end{cases} \tag{8}$$

Assuming $\phi_i = kx_1\cos\theta + ky_1\sin\theta + \varepsilon_i$, $\phi_r = kx_1\cos\theta + ky_1\sin\theta + \varepsilon_r$, $x_2 = x_1 + \Delta x$, $y_2 = y_1 + \Delta y$, $\Delta l = \Delta x\cos\theta + \Delta y\sin\theta$, and put them into the formula (8), the following expression is obtained:

$$\begin{cases} A_1 = a_i\cos\phi_i + a_r\cos\phi_r \\ B_1 = a_i\sin\phi_i - a_r\sin\phi_r \\ A_2 = a_i\cos(\phi_i + k\Delta l) + a_r\cos(\phi_r + k\Delta l) \\ B_2 = a_i\sin(\phi_i + k\Delta l) - a_r\sin(\phi_r + k\Delta l) \end{cases} \tag{9}$$

Extending the right side of A_2, B_2 in the formula above, inputting the formulae A_1, B_1, and eliminating a_r, ϕ_r, the following formula can be derived:

$$\begin{cases} A_2 = A_1\cos k\Delta l + B_1\sin k\Delta l - 2a_i\sin k\Delta l\cdot\sin\phi_i \\ B_2 = -A_1\sin k\Delta l + B_1\cos k\Delta l + 2a_i\sin k\Delta l\cdot\cos\phi_i \end{cases} \tag{10}$$

Eliminating ϕ_i in the formula (10):

$$a_i = \frac{1}{2|\sin k\Delta l|}[(A_2 - A_1\cos k\Delta l - B_1\sin k\Delta l)^2 + (B_2 + A_1\sin k\Delta l - B_1\cos k\Delta l)^2]^{1/2} \tag{11}$$

According to the above, extending the right side of A_2, B_2 in formula (9), inputting the formula A_1, B_1 and eliminating a_i, ϕ_i, ϕ_r, the following is obtained:

$$a_r = \frac{1}{2|\sin k\Delta l|}[(A_2 - A_1\cos k\Delta l + B_1\sin k\Delta l)^2 + (B_2 - A_1\sin k\Delta l - B_1\cos k\Delta l)^2]^{1/2} \tag{12}$$

It can also be derived from the formula (9) as above:

$$\begin{cases} \phi_i = tg^{-1}\dfrac{A_1\cos k\Delta l + B_1\sin k\Delta l - A_2}{A_1\sin k\Delta l - B_1\cos k\Delta l + B_2} \\ \phi_r = tg^{-1}\dfrac{A_1\cos k\Delta l - B_1\sin k\Delta l - A_2}{A_1\sin k\Delta l + B_1\cos k\Delta l - B_2} \end{cases} \tag{13}$$

For the irregular waves, the wave trains of the incident and reflected waves at the first measured point achieved by the principle of linear overlapping are expressed as:

$$\begin{cases} \eta_i(x,y,t) = \sum_{m=0}^{\infty} a_{im} \cos(-\omega_m t + \phi_{im}) \\ \eta_r(x,y,t) = \sum_{m=0}^{\infty} a_{rm} \cos(\omega_m t + \phi_{rm}) \end{cases} \tag{14}$$

The wave trains of the incident and reflected wave in the second measured point are:

$$\begin{cases} \eta_i(x,y,t) = \sum_{m=0}^{\infty} a_{im} \cos(k_m \Delta l - \omega_m t + \phi_{im}) \\ \eta_r(x,y,t) = \sum_{m=0}^{\infty} a_{rm} \cos(k_m \Delta l + \omega_m t + \phi_{rm}) \end{cases} \tag{15}$$

In the formula (12) or (13), A_1, B_1, A_2, B_2 are the Fourier coefficients respectively:

$$\begin{cases} A_{1m} = \frac{2}{N}\sum_{i=1}^{N} \eta_1(\frac{i}{N}T)\cos\frac{2\pi(i-1)m}{N} \\ B_{1m} = \frac{2}{N}\sum_{i=1}^{N} \eta_1(\frac{i}{N}T)\sin\frac{2\pi(i-1)m}{N} \\ A_{2m} = \frac{2}{N}\sum_{i=1}^{N} \eta_2(\frac{i}{N}T)\cos\frac{2\pi(i-1)m}{N} \\ B_{2m} = \frac{2}{N}\sum_{i=1}^{N} \eta_2(\frac{i}{N}T)\sin\frac{2\pi(i-1)m}{N} \end{cases} \tag{16}$$

Where, N is the total number of samples, T is the time length of the total sample, $T = N \cdot \Delta t$, Δt is the time interval of samples, $m = 1,2,\cdots, N/2-1$. The FFT method can be used in the formula above. In order to get the smoother spectra, the estimated spectra need to be smoothed. There are different smoothing functions often used , such as rectangular, angular and parabola and so on. Here the nine-point rectangular smoothing function is adopted. The amplitudes of the incident and reflected waves derived by the formulae (11) and (12) are the function of frequency and should be expressed as $a_i(f)$, $a_r(f)$. The estimated spectra $S_i(f)$, $S_r(f)$ of the incident and reflected waves, the whole reflected coefficient K_R and the reflected coefficient spectra $k_r(f)$ can be achieved by $a_i(f)$, $a_r(f)$. The frequency spectra of the incident and reflected waves can be derived from the formula (17).

$$\begin{cases} S_{im}(f) = \frac{1}{2\Delta f} a_{im}^2(f) \\ S_{rm}(f) = \frac{1}{2\Delta f} a_{rm}^2(f) \end{cases} \tag{17}$$

$$K_R = \sqrt{\sum_{m=1}^{N} S_{rm}(f)\Delta f \Big/ \sum_{m=1}^{N} S_{im}(f)\Delta f} = \sqrt{\sum_{m=1}^{N} a_{rm}^2(f) \Big/ \sum_{m=1}^{N} a_{im}^2(f)} \tag{18}$$

$$k_r(f) = a_{rm}(f)/a_{im}(f) \tag{19}$$

From the formulae (11) and (12), it can be seen that when $\sin(k\Delta L)=0$, there is a singular problem, therefore, the situation that $k\Delta L=0$ should be avoided, that is $\Delta L/L = n/2$, in which $n = 0,1, 2\cdots$. It is noted that when arranging measured points, proper values should be chosen so that the main part of the wave spectrum is in the range of the two odd points. According to Goda, the wave length L_{max} and L_{min} can be calculated from the expected range f_{min} and f_{max} of the spectrum and also by controlling $\Delta L/L_{max} \geqslant 0.05$, $\Delta L/L_{min} \leqslant 0.45$. In addition, for formulae (11) and (12), when $\theta = 0^\circ$, that is, the wave is

a normal incidence, $\triangle L=k\triangle x\cos\theta+k\triangle y\sin\theta=k\triangle x$, which is the same as the Goda's. It is suggested that the Goda's method is a special case.

2 Numerical Test

According to the input target spectrum and the input reflected coefficient, the unidirectional irregular incident waves, reflected waves and the synthetic waves on the measured points are simulated in this paper. In order to review the separating result of the improved two-point method on the synthetic wave train of the different wave directions and different reflected coefficients, the wave direction θ is adopted as 0°, 15°, 30°, 45°, 60°, and the reflected coefficient $(K_r)_I$ 1.0, 0.75, 0.5, 0.25 respectively. The target spectrum input is JONSWAP, in which, $\gamma = 3.3$, $\sigma_A = 0.07$, $\sigma_B = 0.09$, the peak frequency f_p is 1Hz, the potential height H_s is 0.08 and the depth of water d is 0.5m, the sampling time interval $\triangle t$ is 0.05s, and the total sample number is 4 096. The same wave factors are adopted as the parameters of physical model so that the comparison with the physical experiment can be made conveniently. The array for simulating wave is adopted as pentagon. The coordinates of the five measured points and the arrangement of gauges are showed in Fig.1. The abscissa X is perpendicular to the structures and the ordinate Y is parallel to the structures. The pentagon array is disposed in front of the structures and the minimum distance between the measured point and the structures is 0.5m. For the numerical test, the problem of the minimum distance between structures and the measured point can be ignored, but for the study of the physical model and the field, the problem of the minimum distance and the wave stability condition before structures must be taken into account, for which reference can be made to the work of Goda (1976) or Yu Yuxiu (1992).

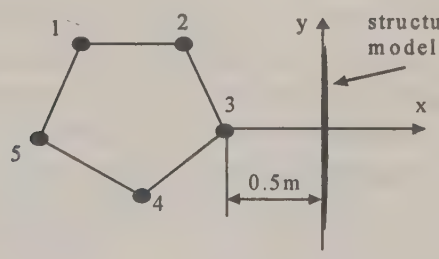

Measuredd Points	x	y
1	-1.2	0.49
2	-0.7	0.47
3	-0.5	0.00
4	-1.0	-0.30
5	-1.4	-0.10

Unit: m

Fig.1 The sketch of wave gauges disposed

The details of the simulating waves is as follows. The linear overlapping method is adopted to simulate the synthetic waves and the method of the equal divided frequency and energy are adopted in dividing the frequency band. In the paper, the method of the equal divided frequency is used and the M is set as 50~100. The equation of the wave elevation is expressed as the formula (20), in which, the first item on the right side of the equal sgin is the incident wave elevation and the second is the reflected wave elevation.

$$\eta(x,y,t)=\sum_{m=1}^{M}[a_m\cos(k_m x\cos\theta+k_m y\sin\theta-\tilde{\omega}_m t+\varepsilon_{mi}) + K_R\cdot a_m\cos(k_m x\cos\theta+k_m y\sin\theta+\tilde{\omega}_m t+\varepsilon_{mr})] \quad (20)$$

in which, amplitude $a_m=\sqrt{2S(\hat{\omega}_m)\Delta\omega_m}$, $\hat{\omega}_m=(\omega_{m-1}+\omega_m)/2$, $\Delta\omega_m=\omega_m-\omega_{m-1}$,

$m=1,2,\cdots, M$. The angular frequency $\tilde{\omega}_m$ is chosen randomly in all bands, and the initial phases ε_{mi}, ε_{mr} are adopted as the random number distributed evenly in the range of 0~2 π, k_m is the wave number of the compoonent waves and K_R is the inputting bulk reflection coefficient. The wave elevations of the incident waves, reflected waves and the synthetic waves are showed in Fig.2, in which, the incident angle of the wave propagation is 15°, the reflection coefficient is 0.5, the potential height of incident wave is 0.08m and its period is 0.95s, the maximum height is 0.134m, the minimum height is 0.003m, and the average wave height is 0.05m.

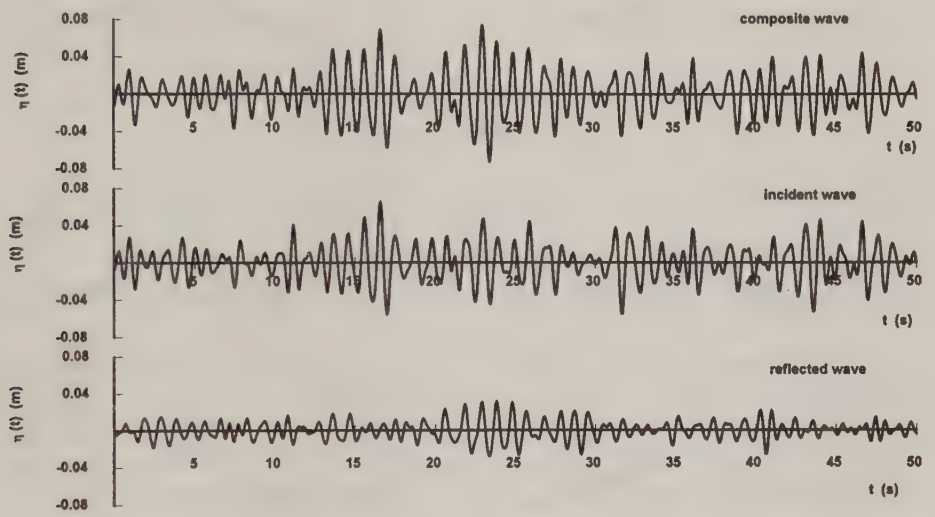

Fig. 2 elevations of the incident waves, reflected waves and the synthetic waves input ($K_r = 0.5$, $\theta = 15^\circ$)

2.1 The separated frequency spectra and the reflected coefficient spectra

By using formulae (11), (12), (17), (18) and (19), the frequency spectra of the incident waves, reflected waves and the synthetic waves, the bulk reflection coefficient and the spectra of the reflected coefficient can be obtained. Fig.3 shows the distribution of all kinds of calculated frequency spectra. Figs.3 (a) ~3(d) show the frequency spectra when the wave propagation direction of the incident waves is 0°, namely, normal incidence, and the reflected coefficient is 1.0, 0.75, 0.5, 0.25 respectively. The frequency spectra in Figs.3(e)~3(h) are in different reflected coefficient and the incident wave direction is 60°, namely oblique incidence. From Fig.3, it can be seen that the distribution of all kinds of frequency spectra is basically correct and the separated frequency spectra of the incident waves are almost consistent with the inputting target spectra. The calculated bulk reflection coefficients are approximate to the inputting reflected coefficients. Also near the part of the peak frequency, the spectra of the reflected coefficient approach the inputting values, but sometimes on the two sides far from the peak frequency, the difference is obvious. It can be explained by the fact that because of the small spectrum of the incident and reflected waves in this band, the calculated error is large and the error of the quotient between the two is even larger, but their effect on the bulk reflection coefficient is little. It can be proved by the analyses above that the improved two points method of separating incident and reflected waves is correct and can be applied to the practical project computation.

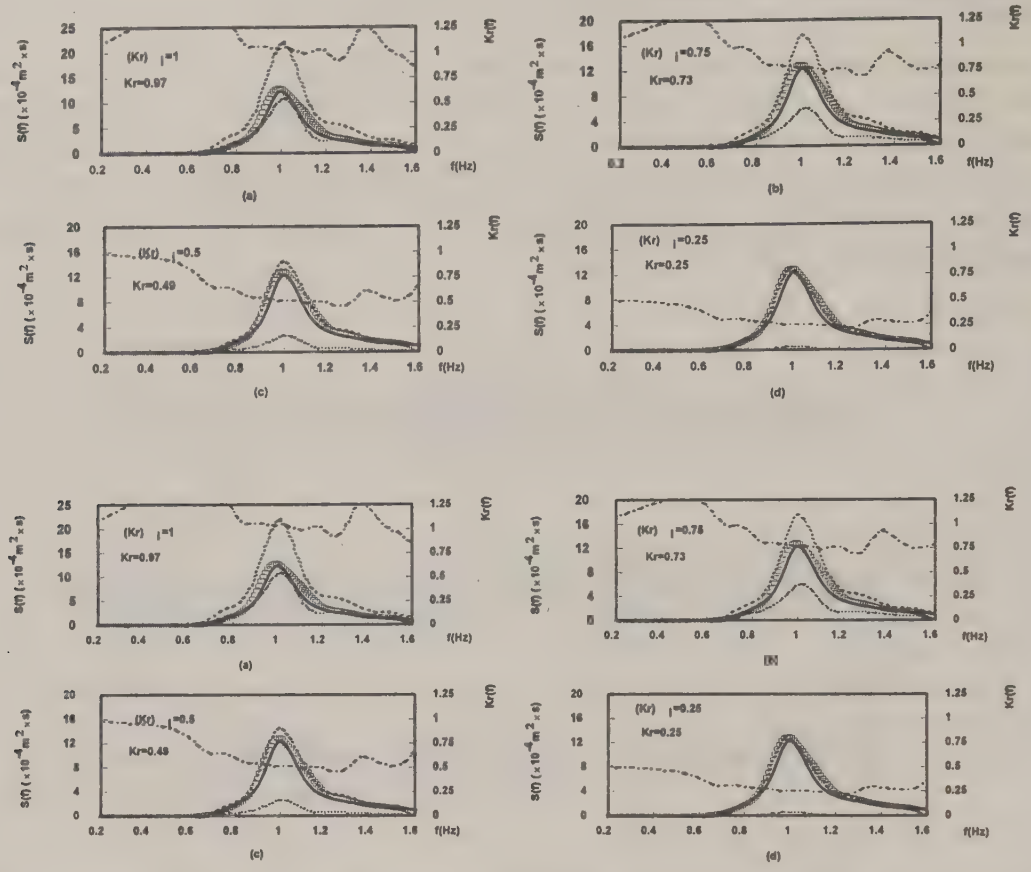

Fig. 3 The computed frequency spectra of the incident waves, reflected waves and the synthetic waves and the spectra of the reflection coefficient

(Kr)i the input reflection coefficient, Kr the computed reflection coefficient

——Spectrum of input incident wave, □□□Spectrum of computed incident wave, ……Spectrum of computed reflected wave, -------- Spectrum of computed resultant wave, -·-·-· Spectrum of computed reflection coefficient

Linmited by the singular point, the correct separated result can not be achieved by each composition of two probes. Only when the most part of the separated power spectra is within the range of f_{min} and f_{max}, is the result credible. In this paper, the peak frequency f_p is 1Hz, its wave length L_p is 1.5m, and when L meets the need of $\triangle L/L_P$ = 0.05~0.45, especially in the middle of the range, the whole spectrum can be derived. For example, for normal incidence, the spectra are good when $\triangle L$= 0.267m by combining point 1 and point 4, $\triangle L$ = 0.279m by combining point 2 and point 4, while for inclined incidence and the incident angle is 15°, the $\triangle L$ = 0.301m by combining point 1 and point 5, $\triangle L$ =0.348m by combining point 4 and point 5. In the study of mathematical and physical model, because the wave length of peak frequency can be known in advance, the locations of two measured points can be designed beforehand. While in field, the wave length range of the peak frequency can not be known in advance. If the measured points are not located well, good separated spectra can not be achieved. In order to solve the problem, it is better to estimate the wave length range of the peak frequency and to dispose several wave gauges at different intervals, then better separated combination can be chosen.

Tab. 1 Comparison of the spectrum factors and the statistic parameters

	Angle of incident wave	K_r	H_s cm	S_{max} $10^{-4}m^2s$	f_p Hz	Q_p	M_0 10^{-4} m^2	T_{02} s	ε	Two probes combined
Spectral parameters of input incident waves	0°	1.0	8	13.02	1.0	3.44	4.32	0.89	0.55	
	15°	1.0	8	12.99	1.0	3.43	4.32	0.89	0.29	
	30°	0.75	8	12.94	1.0	3.43	4.32	0.89	0.54	
	45°	0.5	8	12.87	1.0	3.42	4.31	0.89	0.53	
	60°	0.25	8	12.84	1.0	3.41	4.31	0.89	0.49	
Spectral parameters of separated incident waves	0°	0.96	8.12	13.05	1.0	3.80	4.11	0.92	0.35	1,4
	15°	0.97	8.04	13.22	1.0	3.99	4.03	0.93	0.32	1,5
	30°	0.73	7.65	12.98	1.0	4.60	3.65	0.97	0.25	1,3
	45°	0.49	7.76	12.78	1.0	4.35	3.75	0.95	0.27	1,2
	60°	0.26	8.10	12.77	1.0	3.74	4.09	0.92	0.36	1,2
	0°	0.97	8.10	12.86	1.0	3.77	4.09	0.92	0.35	2,4
	15°	0.97	7.89	13.18	1.0	4.24	3.89	0.95	0.28	4,5
	30°	0.73	7.64	12.97	1.0	4.69	3.62	0.97	0.24	1,5
	45°	0.49	7.70	12.93	1.0	4.49	3.70	0.96	0.26	1,4
	60°	0.25	7.97	12.77	1.0	3.96	3.97	0.93	0.32	2,3

2.2 The comparison of the spectral factors and the statistic parameters

In order to further verify the reliability of the separating method , the spectral parameters of the mathematical model are compared quantitatively with the real values. The calculated spectral parameters are listed in Tab.1, in which, K_r is the bulk reflection coefficient, H_s is the potential height of the incident waves, S_p is the spectrum of the peak frequency, f_p is the peak frequency, Q_p is the spectral sharp degree, M_0 is the zero order moment, T_{02} is the average period, and ε is the parameter of the spectral width. The incident angles of the inputting incident waves are 0°~60°, the reflected coefficients are 1.0, 0.75, 0.5 and 0.25 respectively. From Tab.1, it can be seen that for different incident angles and reflection coefficients, the main spectral parameters of the inputting incident waves are approximated to the corresponding parameters of the separated incident waves. For example, the peak frequency is 1 Hz, the potential height is 0.08m, the spectrum is $0.0013m^2s$, the average period is 0.9s and the coefficient of spectral sharp degree and the zero order moment are also Identical. The smaller the inputting reflection coefficientis is, the more approximate the calculated reflection coefficientis is, thus indicating that the separated results are right.

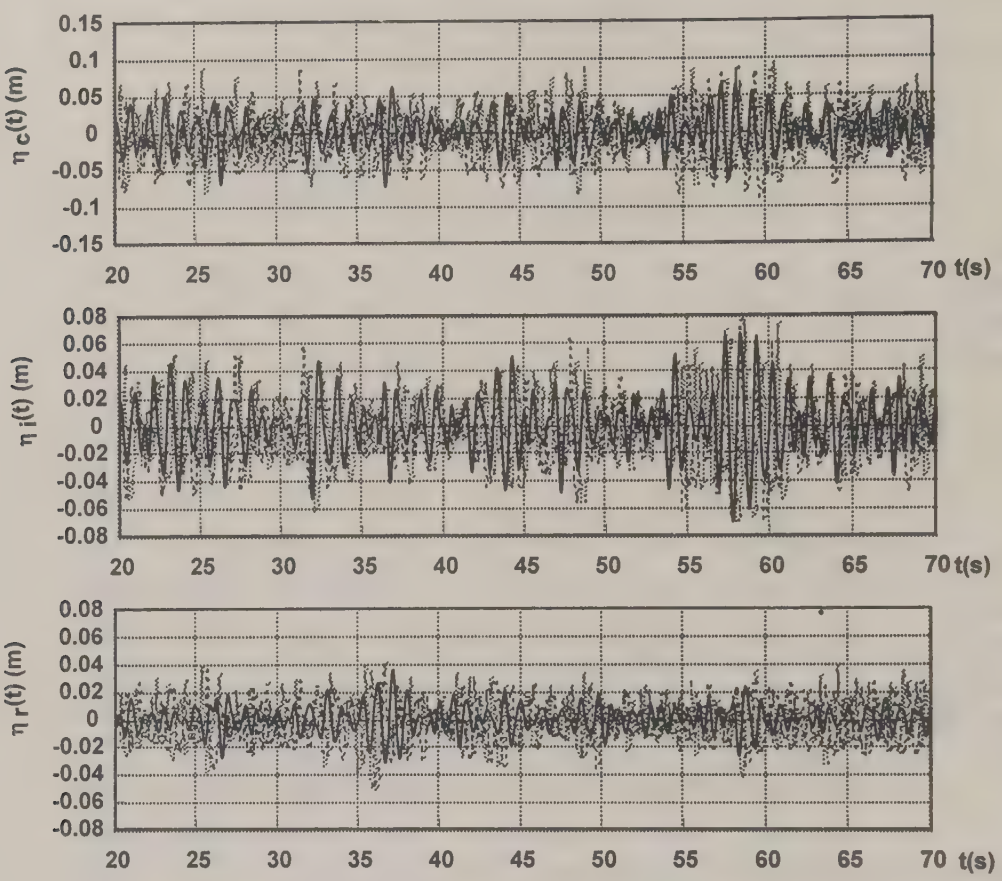

—— The input wave train, — — — The output wave train at probe 1, ·····The output wave train at probe 3

Fig. 4 The comparison of the separated wave trains and the input wave trains

Tab. 2 Statistic characteristics of wave trains

			The trains of input incident wave							The trains of separated incident wave						
θ	K_r	probe	$H_{1/3}$ cm	$T_{1/3}$ s	H_{ave} cm	T_{ave} s	H_{max} cm	H_{min} cm	Hr_{ns} cm	$H_{1/3}$ cm	$T_{1/3}$	H_{ave} cm	T_{ave}	H_{max} cm	H_{min} cm	Hr_{ns} cm
0°	1.0	1	8.0	0.94	5.0	0.84	13.4	0.4	5.7	7.9	0.93	5.3	0.92	12.3	0.6	5.7
	0.5	2	8.1	0.94	5.1	0.86	13.5	0.7	5.7	8.1	0.94	5.0	0.90	14.1	0.6	5.6
15°	1.0	1	8.1	0.93	5.1	0.87	13.4	0.8	5.8	8.0	0.94	5.0	0.93	13.1	0.2	5.7
	0.5	4	8.2	0.93	5.1	0.87	13.6	0.9	5.8	7.9	0.95	4.8	0.92	12.7	0.3	5.5
30°	1.0	1	8.1	0.93	5.1	0.85	13.6	0.9	5.7	7.7	0.98	4.7	0.94	11.6	0.3	5.3
	0.75	1	8.2	0.93	5.1	0.87	13.5	0.9	5.8	7.6	0.98	4.7	0.94	13.2	0.1	5.4
45°	1.0	1	8.1	0.94	5.0	0.85	13.4	0.5	5.7	7.7	0.96	4.9	0.96	11.6	0.7	5.5
	0.75	2	8.1	0.95	5.1	0.86	14.3	0.1	5.7	7.7	0.96	4.9	0.94	11.4	0.2	5.5
60°	0.5	1	8.1	0.95	5.0	0.85	14.3	0.2	5.7	7.9	0.94	5.0	0.90	14.6	0.5	5.6
	0.25	2	8.0	0.95	5.0	0.85	15.2	0.5	5.7	7.6	0.95	5.0	0.90	13.6	0.7	5.5

2.3 The comparison of the separated wave trains and the input wave trains

According to the separated frequency spectra of the incident waves, the reflected waves and the synthetic waves, the wave elevation in all measured points can be calculated by the formulae (14) and (15). Under the condition of different reflected coefficients and different incident angles, the wave elevation of the measured points are compared with the inputting incident wave elevation, the reflected wave elevation and the synthetic wave elevation. Fig.4 shows the elevation of the wave gauge 1 and gauge 3 and the inputting wave elevation when the incident angle is 30 and the reflection coefficient is 0.5. It can be seen from Fig.4 that the wave train measured at gauge 1 and gauge 3 are approximate and the incident and synthetic wave trains at the two measured points approach the corresponding inputting wave trains, but there is no complete agreement. Fan Qijin (1985) by analyzing the real data concludes that the wave processes of the synthetic waves derived by separating the normal incident and reflected waves are approximate. The separated wave train will be affected because of the singular limitations. In addition, the analysis of time domain is sensitive to the phase and the accumulated errors also have influence on the result of separation. Besides the above, the inputting wave trains are quantitatively consistent with the separated wave trains in the statistic characteristics of average wave height and its period, the average wave height of 1/3 large waves and its period, the average wave height of 1/10 large waves and its period, the maximum wave height and its period, the minimum wave height and its period and the average square root wave height (Tab.2). These statistic characteristics are obtained by the method of up-cross zero through the inputting wave trains and the separated wave trains. From the above, it is proved that the analytical method provided in this paper is also correct in the analysis of time domain.

3 Physical Model Experiment

According to the improved method of separating the incident and reflected waves, the physical model tests of the three-dimensional waves are conducted. The sea wall with bottom bed is adopted as the physical model. The model dimension is $0.36 \times 0.53 \times 9.2$(m), the height of the bed is 0.15m, the slope of bed is 1:2. The depth of water is 0.3m, the ratio of the water depth of the bed to the actual water depth is 0.5 and the distance between the reflector and the wave maker is 14m. The wave properties in the experiment are as follows: the potential height is 0.06m, the peak period is 0.99s, the changing range of the wave-making direction is from -15° to 45° and the interval is 15°.

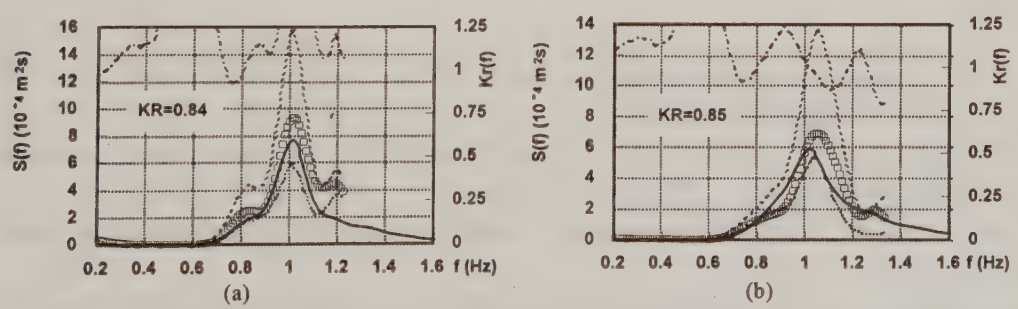

Fig. 5 Spectral density of separated incident and reflected waves of physical model tests

The pentagon array of wave gauges is disposed in front of the model and the radius of the pentagon is 0.5m. The sampling interval is 0.05s and the total length of sample is 2 048, which can make sure that the measured irregular waves are over 100 waves and meets the need of standard design. The center of the pentagon is 1.45m from the middle point of the structure model. The experimental results are shown in Fig.5. In Fig.5(a), the incident wave direction is 0° and in Fig.5(b), 45°. From Fig.5, it can be seen that, by using the improved method, the frequency spectra of the incident and reflected wave trains measured can be separated and the separated incident wave spectra are approximate to the input frequency spectra on condition that no structures are present. The calculated bulk reflection coefficients are reasonable. The separated wave spectra are truncated in the high frequency band because of the singular. Therefore, in practice, the location of the instrument array should be adjusted in such a way that the frequency spectra separated are in the range of the limited frequency band.

4 Conclusions

(1) The improved method of separating frequency spectra of oblique irregular waves and calculating the reflection coefficient is indicated and it can be applied to the separation of frequency spectra of incident and reflected waves in any angles, and also the two wave gauges used to measure waves can be arranged in any direction. The two-point method of Goda is a special example of the methods introduced in this paper.

(2) The new method is verified by the numerical calculation that separated the frequency spectra of the incident and reflected waves by the simulated synthetic wave trains. It suggested that the separated frequency spectra of the incident waves agree well with the inputting target spectra and the calculated bulk reflection coefficients are consistent with the inputting reflected coefficients. Therefore the new method can be applied in the practical projects.

(3) The calculated spectrum of reflected coefficient agree well near the main peak and more departure occurs on the two sides far from the main peak.

(4) The singular phenomenon will occur when the project distance of two measured points on the incident line is multiple of half wave length of the incident wave. The range of the peak frequency is good in the middle of f_{min} and f_{max}, in which, f_{min} can be expressed as $\triangle L/L_{max} = 0.45$ and f_{max} is $\triangle L/L_{min} = 0.05$, $\triangle L$ is the project distance of the two measured points on the incident line.

References

[1] Thornton,E B , Calhoun, R J (1998) Spectral resolution of breakwater reflected waves. J.Wtrwy., Harb., and Coast. Engrg. Div., ASCE, **98** (4), 443 ~ 460.

[2] Goda Y , Suzuki Y (1976) Estimation of Incident and Reflected Waves in Random Wave Experiments. Proc., 15th Int. Coast. Engrg. Conf., . Vol. 1, 828 ~ 845.

[3] Mansard E , Funke E (1980) The Measurement of Incident and Reflected Spectra Using a least Squares Method. ICCE, **80** (1), 154 ~ 172.

[4] Zelt, J A , Skjelbreia J (1992) Estimating Incident and Reflected Wave Fields Using an Arbitrary Number of Wave Gauges. ICCE, **92** (1), 777 ~ 789.

[5] Frigaard P , Brorsen M. (1993) A Time-domain Method for Separating Incident and Reflected Irregular waves. *Coastal Engineering*, **24** (3)(4).

[6] Yu Yuxiu (1985) Laboratory Simulation of Irregular Waves.*Coastal Engineering*, **4** (2), 1 ~ 9.

[7] Huang Peiji, Zhang Lipeng and Guo Dayong (1989) Separation of the Incident and Reflected Waves of Oblique Waves in Front of a Model Structure. *Acta Oceanologica Sinica*, **11** (3), 659 ~ 667.

[8] Yu Yuxiu, Liu Shuxue and Li Li (1992) Namerical Method for the Generation of Multidirectional Irregular Waves. *Acta Oceanologica Sinica*, **14** (4), 143 ~ 169.

[9] Zhu Liangsheng, Sui Shifeng (1997) Research on the Calculation Methods for the Incidence and Reflection of Irregular Waves Along the Sea Dyke. *Proceedings of the Eighth National Coastal Engineering Conference*, 786 ~793.

[10] Sun Zhaochen and Wang Lisheng (1999) Separation of Oblique Incident and Reflected Waves. *Acta Oceanologica sinica*, **21** (4), 114 ~120.

[11] Fan Qijin (1985) Separation of the Wave Forms of Incident cond Reflected Waves.*Harbour Engineering*, (3), 19 ~ 26.

Studies on the Ecology of Fouling Community in Daguanban Reclamation Area of Luoyuan Bay

Zhou Shiqiang（周时强）[1], Ke Caihuan（柯才焕）[1], Lin Dapeng（林大鹏）[2]

1 *Institute of Subtropical Oceanography, Xiamen University,* 361005

2 *Fishery Office of Lianjiang County, Fujian, China,* 350003

Abstract The test panels have been set for one year in the waters of Daguanban reclamation area of Luoyuan Bay to investigate the ecology of fouling community. 39 species of animals and 8 species of algae have been recorded during the investigation. The main period of settlement extends from May to October. The peak periods of biomass and covered area rate of the panels have been observed from June to September.*Balanus reticulatus, Bugula neritina, Molgula manhattensis, Tubularia mesembryanthemum and Enteromopha interstinalis* are the dominant species in the fouling community. Species diversity index, species richness, species evenness and environmental factors are determined, the results of which indicate that water flow speed is the most important factor influencing the species and quantity composition of the fouling community. As to the mariculture production in the reclamation area, the main harmful period ranges from June to September.

Keywords test panel, fouling community, ecology, reclamation area

Introduction

Enclosed in 1975, the Daguanban reclamation area is located on the southern coast of Luoyuan Bay (E119°42', N26°18') in Fujian Province, China, and has a 27.5 km^2 of water area. The reclamation area seawater is exchanged back and forth with coastal seawater through the Qingyu Island gate, Tayu Island gate and Zhuyu Island gate (Fig.1). There is no natural tide in the reclamation area. Freshwater does not flow into the area. Salinity ranges from 24.82 to 31.76. The area and other nearby waters are the important culture bases for economic fish, shrimps, mollusca and algae in Lianjiang County. Test stations were chosen and test panels have been set for one year (1998.1~1999.1) in the reclamation area and the nearby waters to investigate the species composition, the settlement seasons and the biomass of the fouling organism community as well as the relationship between environmental factors and the community. The main purpose of this study is to provide scientific data for prevention and elimination of the fouling organisms, which are harmful to mariculture in the reclamation area.

The test panel investigation on fouling organisms has been mostly conducted in the coastal waters and inside the bays at home and abroad (Huang and Cai, 1984; Zhou et al, 1989). However, this kind of investigation in a semi-closed reclamation area with a special ecosystem has not been reported so far.

Materials and Methods

The test panels are set according to the marine survey investigation standard. The classification and statistics of the fouling organism quantity are carried out on the basis of the methods proposed by

Pastula (1970) and Huang and Cai (1984)[1,3]. Species diversity index (H'), species richness (SR) and species evenness (V) of the community are expressed as follows:

$H' = -\Sigma p_i \lg p_i$, (Shannon and Weaver, 1949)

$SR = (S-1) / \ln N$, (Margalef, 1958)

$V = (H' - H_{min}) / (H_{max} - H_{min})$, (Hurlbert, 1976)

Where S is the number of species, N the biomass, H the observed diversity, H_{max} the maximum possible diversity, and H_{min} the minute possible diversity.

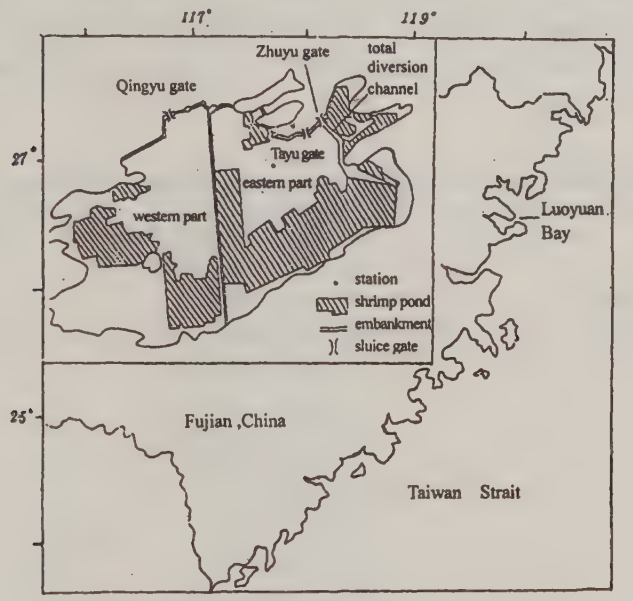

Fig. 1 Map of Daguanban reclamation area

Results

1 Species and settlement seasons

142 pieces of test panels are regained at the end of the investigation and 39 species of animals and 8 species of algae have been recorded (Tab.1). *Balanus reticulatus, Bugula neritina, Molgula manhattensis* and *Tubularia mesembryanthemum* are the dominant species of the fouling animal community on the bottom panels. The common species are *Balanus cirratus, Saccostrea cucullata, Bugula californica, Stylella plicata, Caprella scaura, Corophium uenoi*and *Potamilla myviops*, etc. *Enteromorpha intestinalis* is the dominant species of the fouling algal community on the surface panels. The common species are*Ulva linza, Enteromopha protifera* and *Gelidium divaricatum*,etc. Fouling animals are not observed on the test panels in February and fouling algae are not found on the test panels in January and February, either. There are rare species observed in the months of low temperature (December and January). The settlement periods for the most species range from May to October. The

settlement species and quantity in each month are shown in Table 1 and Table 2. The peak settlement period for *Tubularia mesembryanthemum* ranges from March to April. The normal settlement periods for *Balanus reticulatus* and *B. cirratus* extend from May to October, with a peak period from June to September. The settlement density of these two species reaches 1356.2 ind./m^2 and they cover 69.5% of the panel area in August. *Bugula neritina* appears monthly, with the largest quantities in May, June, November and December, except January and February. *Molgula manhattensis* starts appearing in May and reaches a peak at a settlement density of 773.6 ind/m^2 in June, which is higher than those in other months. The settlement density of the species is still high in November (Fig.2, Tab.2). Fouling organisms on surface panels are observed during March and December. Among them the dominant species is *Enteromorpha intestinalis*. Its peak settlement period extends from the end of spring to the beginning of summer. A mean area of 80.1% of a panel is covered by this species during May and July, with a peak area of 87.4% in May (Fig.2, Tab.3).

Tab. 1 The list of the fouling species on the test panels in Daguanban reclamation area, Louyuan Bay

Coelenterata	23. *Musculus senhousis*
1. *Eudendrium capillare*	24. *sAnommia chinensi*
2. *Tubularia mesembryanthemum*	25. *Mytilus edulis*
3. *Obelia gracilis*	26. *Saccostrea cucullata*
4. *Anthopleura pacifica*	27. *Trapezium japonicus*
Platyhelminthes	**Crastacea**
5. *Psseudoceros exoptotu*	28. *Balanus reticulatus*
Nemertinea	29. *B. cirratus*
6. *Nemetea sp.*	30. *Caprella scaura*
Polychaeta	31. *C. eguilibra*
7. *Harmotoe imbricata*	32. *Corophium uenoi*
8. *Eulalia viridis*	33. *Gammarus sp.*
9. *Nectoneanthes oxypoda*	34. *Pisidia serratifrons*
10 *Perinereis nuntia*	35. *Nanosesarma minutus*
11 *Syllis sp.*	36. *Sphaerozius nitidus*
12 *Potamilla myviops*	37. *Xantho sp.*
13 *Megalomma cingulata*	**Protochordata**
14 *Hydroides elegans*	38. *Styella plicata*
Ectoprocta	39. *Molgula manhattensis*
15. *Bugula neritina*	**Algae**
16. *B. californica*	40. *Enteromopha protifera*
17. *Schizoporella nivea*	41. *E. intestinalis*
18. *Membranipora amoyensis*	42. *Ulva linza*
Mollusca	43. *U. lactuca*
19. *Repana thomasiana*	44. *Ectocarpus confervoides*
20. *Pyrene sp.*	45. *Gelidium divaricatum*
21. *Modiolus barbatus*	46. *G. amarsii*
22. *Adula atrata*	47. *Polysiphonia sp.*

Tab. 2 The biomass and composition percentage of the fouling community on the bottom panels

Month	No. of species	Covered area(%)	Wet wt. (g/m^2)	Composition percentage (%) in wet weight							
				Hydr-oid	Tube-worm	Bryo-zoan	Biv-alve	Bar-nacle	Tubi-culou	Tuni-cate	Others
1	1	0.2	1.3								100
2											
3	4	7.5	20.5	70.7		19.8			6.8		2.7
4	6	11.6	83.4	88.4	2.2	2.9			3.9		2.6
5	9	33.5	145.6	43.2		27.0		8.8	1.5	12.2	7.3
6	11	52.4	454.8	14.5		22.0	0.9	14.1		40.5	7.9
7	10	63.4	661.0	8.0		12.3	1.9	43.0		28.1	1.4
8	13	81.6	1002.5		5.3	2.6	1.6	78.1		13.7	0.8
9	12	77.4	880.0	1.2	3.2	3.8	1.5	65.1	0.3	19.1	5.7
10	8	46.5	418.2		3.3	14.0		40.2		35.5	0.9
11	5	10.6	44.1		9.6	29.0		1.0	0.1	59.2	8.7
12	1	6.5	11.9		2.0	84.0					4.1
3-5	10	82.8	603.4	23.8		47.3		7.2	1.6	8.3	9.8
6-8	15	100.0	1488.0		2.0	3.1	4.4	41.2		41.4	2.1
9-11	14	84.0	1723.9		7.8	3.3	0.1	32.6		59.7	1.9
12-2	7	19.2	95.6	3.3	4.2	83.1			2.6		11.1
12-11	16	88.4	1502.8		14.8	5.8	2.3	20.4			0.8

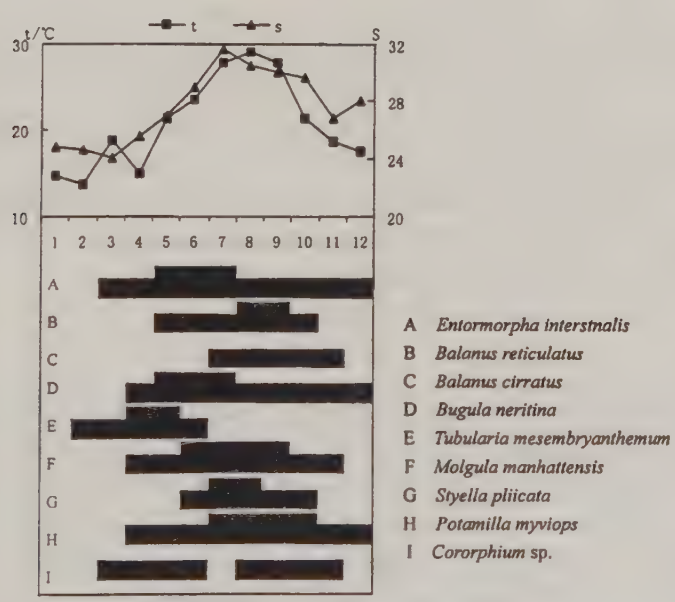

Fig. 2 Settlement periods of the main fouling species in the Daguanban reclamation area, Luoyuan Bay

Tab. 3 The settlement months and biomass of algae on the surface panel

Month	1~2	3	4	5	6	7	8	9	10	11	12
Number of species		1	4	6	6	6	5	6	3	2	2
Settlement area (%)		7.5	21.4	87.5	77.0	77.8	43.9	50.1	33.2	20.2	26.1
Wet weight (g/m^2)		13.5	66.7	187.5	145.9	163.6	90.5	104.8	64.9	32.6	34.5

2 Quantity

Monthly average biomass is 318.6g/m^2 and the average settlement area is 29.1% on the bottom panels. Both of them are obviously higher from June to October. In August the biomass reaches 1002.5g/m^2 and the settlement area comes up to 81.0%, which are the highest in the test year. This is mainly because of the fact that a large number of barnacles settle down and grow rapidly in the high temperature months. Two species of barnacles make up 78.0% of the total biomass in August, 65.0% in September and 43.0% in June, respectively. *Molgula manhattensis* dominates considerably in the composition of the total biomass due to its large size. Seasonal average biomass on the bottom panels is 977.78g/m^2. Seasonal variation ranked in the order of the biomass is 1 723.90g/m^2 in autumn, 1 488.0g/m^2 in summer, 603.41 g/m^2 in spring and 95.60 g/m^2 in winter, respectively. Obviously, the biomass in winter is significantly low. Average seasonal coverage of the panel area is 71.5%. The highest coverage of 100% is observed in summer, followed by 84.0% and 82.8% observed in autumn and in summer. The lowest coverage of 19.2% appears in winter. Yearly total biomass is 1 502.8g/m^2, which is less than those in summer and winter. The coverage of the panels is 88.4%, which is also less than that in summer (Tab.2).

Monthly average biomass of algae on the surface panels is 75.44g/m^2 and the coverage of panel area is 37.1%. The biomasses are significantly higher from May to July, with an average biomass of 165.7 g/m^2. The monthly variation of the biomass depends on the settlement and growth of the dominant species *Enteromopha intestinalis* (Tab.3). Seasonal average biomass of the panels is 124.7g/m^2. Seasonal variation ranked in the order of the biomass is 229.6 g/m^2 in spring, 126.6 g/m^2 in summer, 96.3 g/m^2 in autumn and 46.2 g/m^2 in winter, respectively. The seasonal variation is significant. The seasonal coverage of the panels reach 96.6% in spring, 64.0% in summer, 61.2% in autumn, and 27.6% in winter, respectively, with an average rate of 59.8% in the test year. The total yearly biomass of algae on the surface panels is 110.2g/m^2, which is less than the seasonal average biomass. The yearly coverage of the panels is 46.5%, which is less than the seasonal average covering rate.

Discussion

The green mussel (*Mytilus edulis*) is a cold-temperate species, which is restrictively distributed to the north of Changjiang River estuary in China. Its appearance on the test panels is the result that it shifts from artificial ropes to the test panels. The green mussel is introduced from Jiangsu Province to the reclamation area. Compared with the results obtained from test panels set outside the reclamation area, the panel fouling species of the reclamation waters are the same as those of outside panels except the green mussel (*Mytilus edulis*). The settlement seasons, the dominant and main species of community inside the reclamation area are in accord with those outside the reclamation area, which indicates that the fouling species composition of the reclamation is controlled by the water of Luoyuan Bay.

Species diversity is a biological characteristic which can be determined at the level of community ecology (Cox, 1972; Pielou, 1988). Species diversity index, species richness and species evenness are all measurements to describe the species diversity. They describe the composition relationship between the species and the quantity of a community in different aspects. They are widely used to analyze the time-space variation of a community at the present time. Table 4 shows that the species diversity index (*H*)

and species richness (*SR*) of the seasonal panel community are obviously higher in summer and winter, which relates closely to the fact that the settlement periods of most species extend from May to October. During summer and autumn the evenness decreases as the species increase, which indicates that the biomass of the increased species is lower. As a result, the unevenness of the biomasses of the different species appears and the dominant species are obviously superior in number. Higher diversity of species composition in a community illustrates that a community has higher ability to sustain the relationship between species and quantity and to resist the change of the community within a certain period. Therefore, summer and autumn are the two main seasons when biofouling is serious for the culture production and seawater device, such as floating rafts and net cages. The measures of fouling prevention should be directed mostly at the dominant species.

Tab. 4 Species diversity measurement of the fouling community on the bottom panels in Louyuan Bay

		Spring Mar -May.	Summer Jun.-Aug.	Autumn Sept.-Nov.	Winter Dec.-Feb.	Whole year Jan.-Jan.
Inside the reclamation area	*H'*	0.6477	0.6807	0.6505	0.5826	0.7314
	RS	1.4056	1.7910	1.6102	1.3157	2.0505
	V	0.6374	0.5703	0.5676	0.6873	0.6074
Outside the reclamation area	*H'*	0.6701	0.8359	0.7424	0.6010	0.8633
	RS	1.5181	2.9460	2.5198	1.7254	3.1904
	V	0.6209	0.6056	0.5615	0.5569	0.6101

It can be figured out from Table 5 that some important factors, such as water temperature, primary productivity and phytoplankton quantity inside the reclamation area are obviously higher than those outside the reclamation area. These conditions should be suitable to the growth and reproduction of the fouling organisms, but as a matter of fact, the fouling organism species number, the yearly biomass on the bottom panels, the average biomass of seasonal panels and the covering area rate inside the reclamation water only constitute 48.9%, 21.2%, 55.8% and 83.4% respectively of those outside the reclamation area water. Species diversity of the community inside the reclamation is also lower than that outside the reclamation area (Tab.4). All these data suggest that the developmental level of fouling community inside the reclamation is evidently lower than that outside the reclamation area. The reason is that there exists tidal current outside the reclamation area. Many scientists (Huang and Cai, 1984; Zhou and Li, 1993) agree that water current is a favorable condition for fouling larval settlement and growth under normal conditions, since it facilitates clearing away waste materials on the test panels and provides the fouling organisms with food and oxygen. The stronger the current, the more the species number and the biomass, vice versa. The reclamation area is a semi-closed one. When the sluice gates open for

Tab. 5 Comparison of main factors inside the reclamation area with those outside the reclamation area in the Luoyuan Bay

Factors	Inside the reclamation area			Outside the reclamation area		
	Apr.	July	Average	Apr.	July	Average
T(℃)	17.9	29.8	23.9	14.2	27.6	20.9
S	25.61	31.42	29.01	28.78	30.46	30.65
pH	8.65	8.18	8.42	8.28	8.30	8.29
TR[1] (m)	2.50	1.50	2.00	1.00	1.20	1.10
PP[2] ($mgC/m^2.d$)	138.6	7315.0	3726.8	48.5	264.2	156.4
Phytoplankton($10^4 ind./m^3$)			20.5			11.3

1) TR: transparency of seawater, 2) PP: primary productivity

seawater to enter or drain off, the canal and its nearby waters flow faster, while the levels of most waters of the reclamation area rise or drop very slowly. The water inside the reclamation area flows more slowly than that outside the reclamation area, which is the major factor restricting the development of the fouling community in the reclamation area.

Conclusion

1. The Daguanban reclamation area of Luoyuan Bay, China is a special semi-enclosed environment. During the investigation 39 species of animals and 8 species of algae are found on the test panels. The main period of settlement extends from May to October. The peak periods of biomass and the rate of covered area extend from June to September.

2. The dominant species of the fouling community are *Balanus reticulatus, Bugula neritina, Molgula manhattensis, Tubularia mesembryanthemum and Enteromopha interstinalis.*

3. The fouling species composition in the Daguanban reclamation area is controlled by the Luoyuan Bay. The number of species and biomass of the fouling in the reclamation area is evidently lower than that outside, the results of which indicate that the motive power of the water is the most important factor influencing the development of the fouling community.

4. As to the mariculture production in the reclamation area, the main harmful period ranges from June to September.

References

[1] Cox, G. W. (1972) Laboratory manual of general ecology. Brown Company Press, 120-123.

[2] Huang, Z. G. and Cai, R. X. (1984) Marine fouling organism and its prevention. China Ocean Press, p352.

[3] Hurlbert, S. H. (1977) The non-concept of species diversity: a critique and alternative parameter.*Ecology*, 52:577 - 586.

[4] Margalf, D. R. (1958) Information theory in ecology. *General System,* 3:36 - 71.

[5] Pastula, E. J. (1970) World atlas of coastal biological fouling. USA Naval Oceano. Office, IR NO. 70 - 51.

[6] Pielou, E. C. (1968) Mathematical ecology. John Wiley and Sons, New York, p551.

[7] Shannon, C. F. and Weaver, W. (1949) The mathematical theory of communication. Univ. Of Illinois Press, Urbana, p177.

[8] Woods Hole Inst. Res. (1952) marine fouling and prevention. 203 - 240.

[9] Zhou, S. Q., Li, F. X. and Lin, D. P., Studies on the ecology of fouling organisms in nearby waters of Daguanban reclamation area in the Luoyuan Bay. *J. Xiamen Univ.* (Nat. Sci. Ed.), 28: 139-143 (in Chinese with English abstract).

[10] Zhou, S. Q. and Li, F. X. (1993) Ecological studies on mangrove fouling animals in Jiulong River estuary, Fujian, China. *Taiwan Straits*, **12** (4), 336 - 341 (in Chinese with English abstract).

Isolated Cells of *Porphyra yezoensis* Cultured on Solid Medium

Shen Songdong（沈颂东）
Department of Biology, Life Sciences College, Suzhou University, Suzhou, Jiangsu 215151
Dai Jixun （戴继勋）
Marine Life Sciences College, Ocean University of Qingdao, Qingdao, Shandong 266003

Abstract Vegetative cells of *Porphyra yezoensis* are isolated with sea snail enzyme and cultured on the solidified agar medium. The results of experiments show that the isolated cells can survive, divide and regenerate well on the medium solidified with agar. The first division on the solid medium starts after 7 days' culture, 4 days later than the liquid culture. The survival rate of isolated cells is 71.3% on the solid medium, lower than the 86.2% of that in seawater. Thalli, thalloids, conchocelis, spermatangia and multicellular masses are developed on the solid medium in the first month, slowly but normally. Spermatangia sacs disappear within 4 weeks. Without adding nutrient liquid onto the surface of solid medium or injecting seawater under the agar layer in order to keep moisture, the thalli and cell groups release monospores to form new thalli instead of enlarging their areas after 5 weeks' culturing. Some monospores regenerate new thalli. Other monospores lose their pigments and minimize their volume and divide quickly to form light pink calli. After 16 weeks, numerous calli can be seen on the solid medium and after 24 weeks' culturing, almost only calli and conchocelis can be seen. If the calli are immersed in seawater, the monospores are released and may develop into young thallus.

Keywords Solid culture, *Porphyra yezoensis*, thallus, callus, multicellular mass, development

Introduction

Cell isolation and culture research in seaweeds is a relatively new field and lags far behind that of higher plants[1]. There are two problems that restrict the blossom of seaweeds cell culture. One is lack of suitable materials. For seaweed thallus appearing seasonally, it is impossible to obtain the materials all the year round except *Porphyra carolinensis* which persists in the blade phase throughout the year without an intermediate conchocelis phase[2]. The other is lack of isolation methods. The cell wall of seaweeds contains several kinds of polysaccharide and is difficult to digest. Some phycologists have attempted to grind the *Porphyra thallus* and isolate cells for culturing, but it can't isolate thick thalli of green and brown algae[3].

After the sea snail enzyme is found and applied in macroalgae cells and protoplasts isolated[4~5], a lot of seaweed cells are isolated and cultured with shellfish digestive enzymes, such as, green algae *Monostroma*[6~7] and *Ulva*[8], red algae *Chondrus*[9], *Porphyra*[10~11] and *Gelidium*[12] and brown algae *Undaria*[13]. The growth and development of isolated cells and protoplasts of *P. yezoensis* and *P. haitanensis* are studied in detail. The regenerated seedlings are cultivated at sea in China. Also the

* This work was supported by a fund for doctorate candidate scientific research from the Ministry of Education (98042303) and doctor start fund of Suzhou University (Q4114928)

cryopreservation technique has made great headway for seaweeds.The thalli of *P. yezoensis* could be preserved in the freezing condition for more than 2 years' and still keep cells viable just after 2 days' recovery[14]. But almost all of the seaweed cells and protoplasts cultures are in liquid medium. The cells of higher plants are always cultured in solid media in order to observe cell growth and development. Solid medium is seldom applied in the seaweed cell culture except Polne-Fuller & Gibor[15] to grow and select calli developmental seaweed.

In order to clarify the isolated cell development process of *Porphyra*, and understand the nutrients influences, the cells must be located at a certain position for position investigation, so that the algae solidified medium is applied in this research.

1 Materials and Methods

1.1 Treatment of explant

The young thalli of *Porphyra yezoensis* were collected along the coast of Huiquan Bay, Qingdao on March 1, 1999. The average length of thalli ranges from 2.0~5.0 cm. After being dried in shade 8 hours at 20℃ with good ventilation, the thalli were preserved at the -20℃ refrigerator. Two days before the experiment, a little of the freezing thalli was brought out and recovered in cool boiled sea water in 20℃. Both surfaces of the recovered thalli were washed with brushes many times in order to remove sand and microalgae. Then the thalli were immersed in the solution of seawater with 0.7% KI and was changed 0.1% Penicillin for 10 minutes to kill the bacteria and eggs of parasites. The cool boiled seawater was changed many times to remove the medicines.

1.2 Cell isolation with enzyme

Sea snail enzyme is obtained from the Ocean University of Qingdao. The thallus was cut into pieces, then incubated in 2% enzyme solution adding 2mol L^{-1} glucose at 20℃ for 2 hours. The separated cells and digestive solution are filtered through nylon mesh (40 μm) to remove the tissue debris and centrifuged at 1000 rpm for 5 minutes to collect isolated cells.

1.3 Solid medium preparation

Seawater enriched with 10mg L^{-1} of KNO_3-N and 1mg L^{-1} of KH_2PO_4-P is boiled for 10 min. with 1.0 g agar powder and 0.1g per 100mL of active carbon added. Keep the solution boiling for 10 minutes in order to melt the agar powder fully. The medium was dispensed into 9 cm (10 mL) or 5cm (5 mL) sterile Petri dishes. After cooling, the dishes are sealed with Parafilm and the film is renewed after the experiment has been started.

1.4 Cell Culture

The isolated cells are prepared as above, evenly on the surface of solid medium with the density of 1,000 cells cm^{-2}. Petri dishes are placed in 20℃ illuminating incubator. The white fluorescent light intensity is adjusted to 30 μm ol photon m^{-2} s^{-1} and the light period is 12L:12D.

2 Results

2.1 Early development on the solid medium

The viability of isolated cells is indicated by phycoerythrobilin content (red color). The initial viability of isolated cells is more than 90% (Figure 1). They survive on the solidified agar surface at the rate of 71.3%, lower than the 86.2% achieved in seawater. First cell divisions occur within seven days on

the solid medium, 4 days later than that in liquid culture. Cells grow slowly but normally during the first month and develop into physiological stages. The younger vegetative cells polarize firstly by increasing their diameter and then dividing into two cells along the long axis. The lower cell next enlarges its volume with the vacuole bulging and then forms the strong, round structure with a short rhizoid at the end. The upper cell divides several times in a line and develops into monostromatic thallus directly (Figure 2). Some cells develop into thalloids without rhizoid or with thin filaments. Although maintaining a layered shape, thalloids has different forms, long, round or irregular, but not the normal leaf-like shape (Figure 3). The other kind of vegetative cell forms a transparent membrane surrounding itself before the first division and then divides many times in all directions inside the membrane, developing into multicellular masses (Figure 4). The white spermagonium cells start dividing earlier than the vegetative cells. Ten days later, the spermatangium sacs are formed. Sperms are emitted from the spermatangium sac and stay in the vicinity for a short time, then die away. The sperm and spermatangium sac vanish in the 4th week. Although the thallus is young, there are a few carpospores on the solid medium. Some of the carpospores germinate unipolarly within 7 days and the conchocelis grow slowly and continuously throughout the culturing process (Figure 5). The conchocelis remains alive for half a year on the solid medium without any nutrients added. There are also some carpospores, which enlarge their volume steadily with infra-cell division. Enlarged carpospores develop into conchosporangia branches directly, 10~15 days after the normal conchocelis develops.

If the Petri dishes have been sealed well with parafilm, or the surface of solidified medium is moist, there is no need to add liquid medium. But with frequently opened dishes, or poorly sealed ones, moisture is restored by injecting 50% diluted sea water under the agar layer, so as not to disturb the growth and development of cells. Thallus, thalloid and multicellular mass grow well in the early 4 weeks' culturing with 20~100 cells in each individual.

2.2 Release of monospores and callus formation

After 4 weeks in culture, the nutrients of solid medium become limited and/or the toxic metabolite begins to accumulate, limiting further growth of thallus or irregular masses. Large amounts of monospores are released by the decomposing of multicellular masses and part or all of thallus and thalloid after 5~10 weeks in culture (Figure 6). The monospores are of uniform size, with centric pigments. When transferred to the fresh medium, they develop into new thalli in normal morphology. Ten weeks after the transfer, the monospores shrink and lose the stellate pigments whether released or not (Figure 7). The monospores divide fast, forming light pink masses on the solid medium. The masses grow rapidly so that within 3~4 weeks, each develops into callus with a diameter of 3~5 mm. After 16 more weeks, there are many calli on the solid medium. After 24 weeks' culturing, almost only calli and conchocelis can be seen on the agar medium (Figure 8). If the calli are immersed in seawater, the monospores are released (Figure 9) and may develop into young thalli (Figure 10).

3 Discussion

Chen indicates that there is no single developmental pattern common to *Porphyra* species[16]. We find even in the same species that there are several developmental pathways. There are different cells in different parts of an adult thallus of *Porphyra yezoensis*. In the lower part, near the rhizoid area, there are large gray-green cells, each with a long tail. The diameter of these cells ranges from 10~20 μm. The rhizoid cells divide slowly, and can only divide a few times to form irregular masses, which can not

release monospores and disappear within 5 weeks on the solid medium. The upper middle areas near rhizoid are the youngest vegetative cells, round, red and with a diameter of only 7~10 μm, they develop into thalli directly in culture. On the upper edge and in the youngest vegetative area are adult vegetative cells, which form thalloids and multicellular masses. Higher in the adult vegetative area, there are very complex cells, including vegetative cells and reproductive mother cells which develop into irregular masses, spermatangonia and carposporangia respectively. On the edge and top of the thallus, there are carpospores, small white spermatangonium cells and vegetative cells. When these cells are cultured on the solid medium, vegetative cells develop into cell masses, then release monospores to grow normal thalli. Spermatangium cells form colorless sacs, then release sperms, and carpospores germinate filamental conchocelis. The above description applies to most but not all of the *Porphyra yezoensis* thallus considering all of the areas. The young thallus contains only rhizoid and vegetative parts without reproductive cells. It is found that carpospores germinate conchocelis, although in the material used here only reaching 5 cm in length.

For all kinds of cells in digested solution, they are confused in seawater so that it is difficult to observe the development in point. From comparing the solid culture with the liquid culture, it is found that the cell development pathways are the same. Solid culture can meet the requirement of point observation, and develop callus without hormone inducement. But there are some disadvantages in solid culture. First of all, it takes a long time to divide and develop, so that it will need more time in culture and investigation. Secondly, the solid medium needs axenic culture, in order to avoid the pollution of bacteria or fungi. Thirdly, it is said, there are many toxic materials produced and can not be diluted on the solid medium, so that they will change the normal development pathway, such as forming callus. We want to decrease the possible influence of toxic materials by adding active carbon in solid medium. The result shows there are not obvious influence on solid culture.

Callus is described as the induction of a disorganized growth of cells in a differentiated tissue (or dedifferentiation) as a result of wounding[17]. But the lower algae, such as *Porphyra yezoensis*, just have a layer of cells without any differentiated tissue developing into callus directly from a single cell. It indicates the limitation of definition of callus. When the medium, solid or liquid, is full of nutrients, the thallus and cell masses develop from vegetative cells. Only when the medium lacks nutrients, will the callus appear, meaning the callus is a kind of growth in stress condition. If the stress enhances, only callus can survive on the solid medium. In this paper, when it is cultured more than 6 months without any nutrients added, all the vegetative cells may develop into callus.

References

[1] Cheney D P, Mar E, Saga N, Van de Meer J(1986) Protoplast isolation and cell division in the agar producing seaweed *Gracilaria* (Rhodophyta). *J. Phycol.*, 22: 238-243.

[2] Freshwater D W, Kapraun D F (1989) Spheroplast isolation and propagation of *Porphyra carolinensis* Coll et Cox for mariculture. Aquaculture, 81: 101-110.

[3] Zhao H D, Zhang X C (1981) Isolation and culture of the vegetative cells of *Porphyra yezoensis* Ueda. *J. Shandong Coll Oceanology*, **11** (1): 61-65 (In Chinese).

[4] Tang Y L (1982) Isolation and cultivation of the vegetative cells and protoplasts of *Porphyra suborbiculata*. *J. Shandong Coll. Oceanology*, 12: 37-50 (In Chinese).

[5] Liu W S, Tang Y L, Liu X W, Fang Z X (1984) Studies on the preparation and on the properties of sea snail

enzymes. *Hydrobiologia*, 116/117: 319-320.

[6] Zhang D L (1983) Study on the protoplast preparation, culture and fusion of somatic cells of two species of green algae *Ulva linza* and *Monostroma angicava* Kjellm. *J. Shandong Coll Oceanology*, 13: 57-65 (In Chinese).

[7] Saga N, Sakai Y (1984) Protoplasts from*Laminaria* and *Prophyra*. *Bull Jap Soc Fish.* 50: 1085.

[8] Fujimura T, Kawai T, Shiga M, et al. (1989) Regeneration of protoplasts into complete thalli in the marine green alga *Ulva perutusa*. Nippon suisan Galkaishi. 55: 1353-1359.

[9] Zhang Q Q (1987) Studies on isolation, culture and regeneration of protoplasts of *Chondrus osculates* Holm. *J. Ocean Univ. Qingdao.* 21: 52-62 (In Chinese).

[10] Dai J X, Bao Z M, Tang Y L, et al. (1988) Studies on isolation of *Porphyra thalli* cells with enzymes and cell cultivation. *Chinese J. Biotechnol.* 4: 127-133 (In Chinese).

[11] Dai J X, Zhang Q Q, Bao Z M (1993) Genetic breeding and seedling raising experiments with *Porphyra* protoplasts.*Aquaculture*, 111: 139-145.

[12] Chen L C M (1989) Cell suspension culture from *Porphyra linearis* (Rhodophyta), a multicellular marine red alga. *J. Appl. Phycol.* 1: 153-159.

[13] Wu S B (1987) Isolation and culture of protoplasts of *Undaria pinnatifida* (Harv.) Suringar. *J. Ocean Univ. Qingdao.* **18** (2): 57-65 (In Chinese).

[14] Shen S D, Dai J X (2000) The study of cell viability of *Porphyra yezoensis* with various recover treatments. *J. Ocean Univ Qingdao.* 30: 292-296 (In Chinese).

[15] Polne-Fuller M, Gibor A (1984) Developmental studies in *Porphyra*. I. Blade differentiation in *Porphyra perforata* as expressed by morphology, enzymatic digestion and protoplast regeneration. *J. Phycol.* 20: 609-616.

[16] Chen L C M (1986) Cell development of *Porphyra miniata* (Rhodophyceae) under axenic culture. Bot Mar. 29: 435-439.

[17] Yeoman M M. (1987) Bypassing the plant. Ann Bot. 60: 157-174.

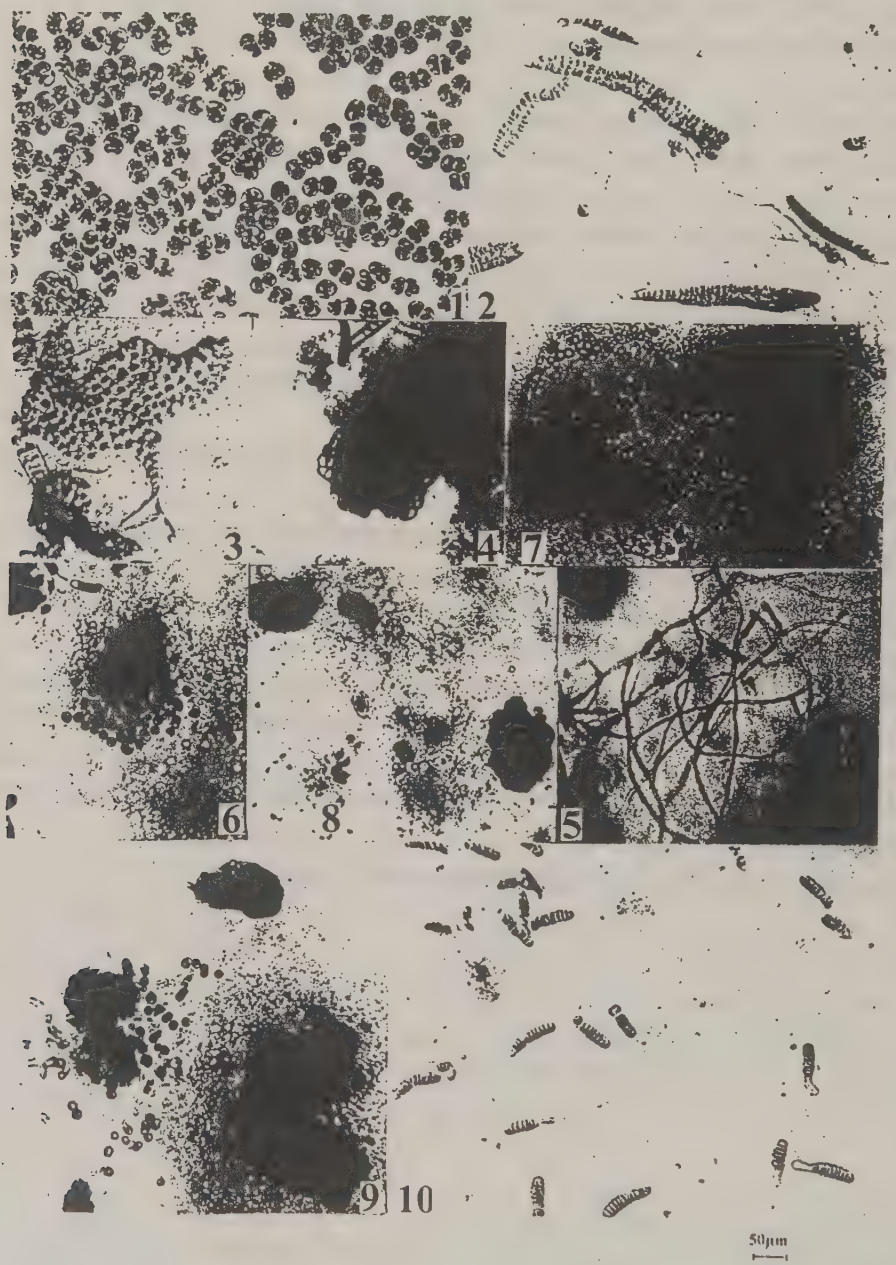

Fig. 1 Isolated Cells with high viability; Fig. 2 The younger vegetative cells developedinto monostromatic thallus directly; Fig. 3 The cells developed into irregular thalloid; Fig. 4 The cells developed into multicellular masses; Fig. 5 Filamental conchocelis appeared and grew steadily on solid medium; Fig. 6 Monospores releasd from multicellular masses with normal pigments; Fig. 7 Monospores minimized the volume and lost the stellate pigments; Fig. 8 Callus appeared at 7 weeks in culture; Fig. 9 Callus release monospores when imersed with seawater; Fig. 10 Monospores from callus can develop into thalli (Bar = 50 μm)

Toxicity Study of Anti-HABs Agents on *Penaeus chinensis**

Sun Xiaoxia（孙晓霞）**, Zhang Bo（张 波）, Yu Zhiming（俞志明）
Institute of Oceanology, Chinese Academy of Sciences, Qingdao, 266071

Abstract In order to study the effect of anti-HABs agents on *Penaeus chinensis*, the toxicity experiments on clay, $Ca(ClO)_2$, $FeCl_3$, and $AlCl_3$ to *Penaeus chinensis* are carried out. The results show that: (1) the clay isn't toxic to *Penaeus chinensis*; (2) $Ca(ClO)_2$ has no toxicity to *Penaeus chinensis* at low levels, but has acute and chronic toxicity at high levels; (3) *Penaeus chinensis* can accumulate Fe and Al. The toxic effect needs further study.

Keywords HABs, anti-HABs agents, *Penaeus chinensis*, toxicity

In recent years, with the development of industry and agriculture, coastal eutrophication has been more serious than before, resulted in frequent occurrences of Harmful Algal Blooms (HABs), seriously damaged the aquatic ecosystems, and brought great economic loss on aquacultural industry. Therefore, people have made extensive studies on HABs mitigation. Clay coagulation method is considered as a kind of promising method, but needs a large amount of material and accordingly results in much residue in application. In order to resolve this problem, Yu Zhiming et al.[1] have proposed modified clays for HABs prevention and obtained better results. Based on the studies, this paper studies the toxicity of the clay, kaolin, and modification agents, $Ca(ClO)_2$, $AlCl_3$ and $FeCl_3$ to *Penaeus chinensis* respectively. The results show that kaolin isn't toxic to *Penaeus chinensis*, $Ca(ClO)_2$, $AlCl_3$ and $FeCl_3$ are good anti-HABs agents at present, can be used in clay modification, thereby providing basis for HABs prevention with modified clays.

1 Materials and methods

1.1 Experimental materials

The biological body length of *Penaeus chinensis* ranges from 7.4cm to 10.0cm, and averages at 8.6cm. The clay mineral kaolin is collected from Wuxian, Jiangsu, and $Ca(ClO)_2$, $AlCl_3$ and $FeCl_3$ are all A.R. agents.

1.2 Experimental methods

Experiments are conducted in big tanks, while control groups are set up at the same time. The volume of experimental water body is $0.5m^3$, with 20 shrimps in each tank. The tanks are aerated fully and shrimps are fed with mixed diet. The seawater is exchanged regularly, the water temperature kept at 25.2~26.1 °C, pH at 7.83~8.12 and salinity at 32. The $Ca(ClO)_2$ experiments are conducted twice, 3 concentration groups each time. At the start of the experiments, the seawater is sampled every hour to determine the content of free chlorine. There are 3 concentration groups for $FeCl_3$ and one for $AlCl_3$

* Supported by National Natural Scientific Foundation (40025614 and 39790110) and Knowledge Innovation Project of Chinese Academy of Sciences (KZCX2-206).

** E-mail: sunxiaoxia@ms.qdio.ac.cn

experiment to determine their accumulation in *Penaeus chinensis*.

Analysis method of Al in shrimps: put some pretreated samples of shrimp in a 50ml color comparison tube , add 5ml EDTA-Zn solution and exactly 2ml Chromazurine-S solution, then 5ml Hexamethylene-tetramine buffer, colormetried in 550nm after 10minutes.

The analysis method for free chlorine is iodimetric method and for Fe is cinefaction-acidation method.

2 Results and discussion

2.1 Effect of kaolin on *Penaeus chinensis*

Kaolin is a kind of silicate mineral with 1:1 layered structure, and its structural unit layer is composed of Si-O tetrahedra and Al-O-(OH) octahedra. Yu Zhiming et al.[2] found that the coagulation ability of kaolin is much greater than that of montmorillonite for the first time and got the conclusion that kaolin was a kind of more efficient clay to remove HAB organisms. The removal efficiency of 1g/L kaolin achieves lmost 100% on *Skeletonema costatum*, and approaches 90% on *Noctiluca scintillans*. The toxicity experiments show that *Penaeus chinensis* wasn't affected by 1g/L kaolin, kept a good growth state and none died during the 5-day experimental period, which further indicates the broad future for HABs prevention in aquaculture water with this kind of clays.

2.2 Effect of $Ca(ClO)_2$ on *Penaeus chinensis*

This experiment was conducted twice. For the first time, the concentration of $Ca(ClO)_2$ was 5, 10, 15mg/L respectively. We observed the change of *Penaeus chinensis* and determined the content of free chlorine in seawater regularly. The shrimps all died in one hour at the concentration of 15mg/L, 11 shrimps died at 10mg/L and one died at 5 mg/L. The degradation process of free chlorine is shown in Figure 1. According to the above results, we decreased the $Ca(ClO)_2$ concentration and did the second experiment. The concentrations of $Ca(ClO)_2$ were 3mg/L, 4mg/L and 7mg/L respectively, and the results are shown in Table 1. After 5 hrs, no shrimps died at the concentration of 3 mg/L, 6 shrimps died at 4 mg/L and all died at 7mg/L. After 24hrs, shrimps in the 3mg/L group showed ingestion after exuviating, and 3 shrimps died in the 4mg/L group, maybe due to the chronic toxicity effect resulted from the low concentration of free chlorine. This result may be slightly different from that of Zhao Zengyuan[3], perhaps because of the difference in the body length of the experimental objects. Comparing our results with reference [4, 3], we can get the conclusion that in the process from fertilized egg to nauplius and the body length of 4.5cm-8.5cm, the tolerant ability of shrimp for free chlorine decreased gradually. According to our results that 0.5 mg/L free chlorine (3mg/L $Ca(ClO)_2$) couldn't result in the death of shrimps, the degradation rate of free chlorine was rather high (figs. 1 and 2) and the large amount of algae and organic matter could decrease the toxicity of free chlorine when HABs break out, we suggest that the concentration of free chlorine be lower than 0.5mg/L in application, which is the same as the conclusion of Zhao Zengyuan.

Tab. 1 Effect of $Ca(ClO)_2$ concentration and time on the mortality of *P. chinensis*

$Ca(ClO)_2$ ($mg \cdot L^{-1}$)	Mortality of *P. chinensis*				
	5h	24h	48h	72h	96h
3	0	5	5	1	0
4	6	3	3	2	3
7	20	0	0	0	0

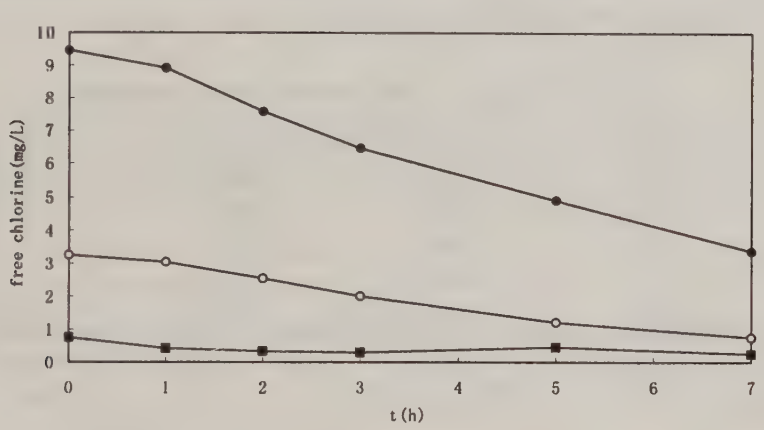

Fig. 1 Degradation of free chlorine at high $Ca(ClO)_2$ concentrations

■5mg/L ○ 10mg/L ● 15mg/L

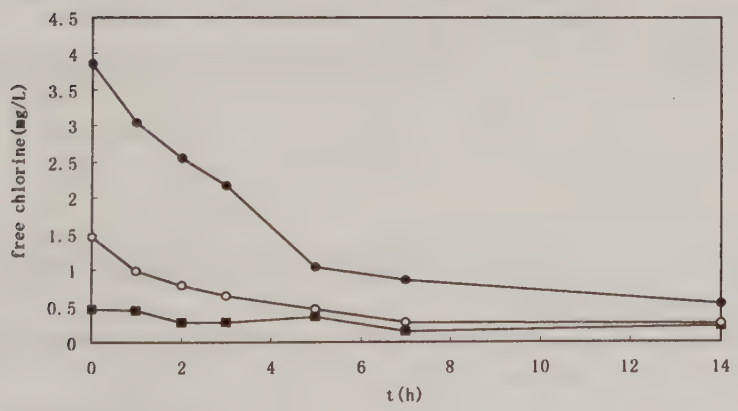

Fig. 2 Degradation of free chlorine at low $Ca(ClO)_2$ concentrations

■ 3mg/L ○ 4mg/L ● 7mg/L

2.3 Accumulation of Fe and Al in *Penaeus chinensis*

There has been no report on content and accumulation study of Fe and Al in shrimp until now. As

shown in Table 2, the accumulation concentration of Fe in shrimp increases with time and Fe concentration, and the accumulation factors of Fe in shrimp increase with the concentration of $FeCl_3$. There was no death of shrimps during the experimental period. They kept normal swimming, ingestion and exuviation except appearing red in gills due to adsorption of Fe. The accumulation of Al in shrimps showed the same trend as that of Fe. The concentration of Al in shrimps increased markedly with time and was almost 3 times that of the control group after 12 days, and the shrimps grew well, showed no abnormal phenomena, but the toxic effect needs further study. The above results indicate that the concentration of $FeCl_3$ and $AlCl_3$ used in HAB prevention wouldn't affect the growth of *Penaeus chinensis* and could be applied in clay-modification safely.

Tab. 2 Accumulation of Fe and Al in *Penaeus chinensis*

Items	Contents of Fe, Al / $\times 10^{-6}$ dry weight			
	Control	Aug. 31	Sep. 6	Sep.12
Fe/60g • m^{-3}		36.96	49.44	75.51
Fe/120g • m^{-3}	39.18	38.09	75.13	98.78
Fe/180g • m^{-3}		46.70	92.16	131.16
Al/54g • m^{-3}	0.824	0.8966	1.694	2.4015

3 Conclusions

In short, we can draw the following initial conclusions:

(1) 1g/L kaolin isn't toxic to *Penaeus chinensis.*

(2) $Ca(ClO)_2$ shows no toxicity to *Penaeus chinensis* at low concentrations, but acute toxic effect at high concentrations, and the safe concentration of free chlorine in application is 0.5 mg/L.

(3) *Penaeus chinensis* has relatively strong ability to accumulate Fe and Al, and the concentration in shrimps increases with time and Fe concentration.

(4) $Ca(ClO)_2$, $FeCl_3$ and $AlCl_3$ can all be used in the modification of clay minerals, and are safe anti -HAB agents.

References

[1] PAN Luqing (1997) The influential studies of several disinfectants to the eggs and nauplius of *Penaeus chinensis. Marine Sciences*, 1: 7-9.

[2] YU Zhiming, ZOU Jingzhong and MA Xinian (1994) A new method to improve the capability of clays for removing red tide organisms. *Oceanologia et Limnologia Sinica*, **25** (2): 226-232.

[3] YU Zhiming, ZOU Jingzhong and MA Xinian (1994) A more effective clay for removing red tide organisms. *Journal of Natural Disasters*, **3** (2): 105-109.

[4] ZHAO Zengyuan, LI Tianbao, GUO Wen et al. (1995) On using bleaching powder to improve water environment in ponds for prawns. *Shandong Fisheries*, **12** (3): 27-31.

Maltivariate Analysis of the Occurring Process of *Skeletonema costatum* Red Tide in the Changjiang Estuary

Huang Xiuqing (黄秀清), Jiang Xiaoshan (蒋晓山), Tao Ran (陶然), and Hong Junchao (洪君超)
East China Sea Monitoring Centre, SOA, Shanghai 200137

Abstract Using the SAS software, the data of environmental factors vs. red tide biomass were analysed during the process of *Skeletonema costatum* red tide which broke out in the Changjiang Estuary on June 9~15, 1990. The results of the multivariate statistical analysis show that the environmental factors are similar in their developing and maintenance periods and that the values of environmental factors begin to be restored to normal levels during the disappearing period. The results obtained from using the methods of correlation, variable cluster and main component analyses are basically identical. The important factors contributing to the occurrence of this red tide are atmospherical pressure, water temperature, salinity, pH, No_3^-, -N, Po_4^{3-}-P and Fe, among which, salinity, Fe and PO_4^{3-}-P are the leading factors which have triggered the occurrence of the red tide as determined by the step-by-step regression analysis. Meanwhile, the linear discrimination functions have been established for the red tide. The environmental factor data of another occurring process of *Skeletonema costatum* red tide in the Changjiang Estuary have been chosen for red tide discrimination with satisfactory results.

Keywords Changjiang Estuary, *Skeletonema costalum*, red tide, multivariate analysis, leading factors, discrimation functions

The red tide is closely related to the environment. The environmental factors may induce a red tide while the formation of a red tide may in turn bring about change in the environmental factors,the growth and decline relationship between the two being rather complicated. How to seek the leading factors affecting the red tide has become one of the subjects of strong interest.[1-3]

Using the SAS (statistical analysis system) software[4], this paper makes multivariate statistical analyses of cluster, correlation as well as regression, main components and discrimination for the data of environmental factors vs. red tide biomass during the whole process of *Skeletonema costatum* red tide which broke out in the first and middle ten-day periods of June, 1990 in an attempt to seek the important and leading factors affecting the occurrence of the red tide. In the meanwhile, preliminary discussions have been made of the red tide forecast through research into the red tide linear discrimination model.

1 Materials and methods

1.1 Sampling

The survey station is set up at the C_{13} observation station within the red tide-prone area in the Changjiang Estuary (Fig.1) and the survey time is June 6~15, 1990. The survey covers the environmental factors (wind speed (u_w),wind direction, current speed (u_c), current direction and atmospheric pressure (p)), physical-chemical factors (water temperature (t), salinity (S), turbidity (Tu),

DO, pH, NO_3^--N, NO_2^--N, NH_4^+-N, PO_4^{3-}-P, SiO_3^{2-}, Fe and Mn) and the variety and quantity of phytoplankton. The water temperature, salinity, turbidity, DO and pH are sampled every two howrs at the 0, 5, 10, 15 and bottom layers while the surface layer is sampled for 69 times; During the red tide, the nutrient is sampled every two hours at the surface, 4m and bottom layers (20m in depth).

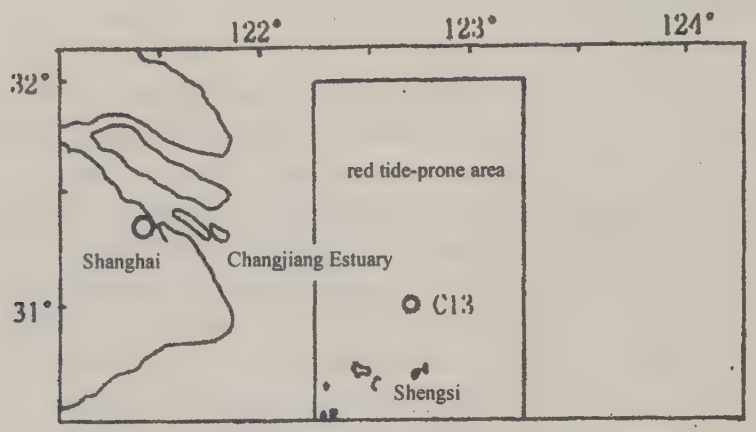

Fig. 1 Location of red tide observation station in the Changjiang Estuary

1.2 Data processing

In terms of the variety composition, quantity variation and changing characteristics of physical-chemical factors of phytoplankton in the course of its occurrence, the red tide is divided into four periods: the beginning period (20:00, June 6~16:00, June 11), developing period (18:00, June 11~ 10:00, June14), maintenance period (12:00, June 14～00:00, June 15) and declining period (02:00, June 15~12:00, June 15)[3,6~8]. According to these four periods of development, the paper divides the data set into four subsets, the sample numbers of the subsets being1~24, 25~56, 57~63, and 64~ 69 respectively. In establishing the database, the relational database structure is adopted, with each line as a record and each column as a field, which are known in the SAS as the observation value and the variable respectively. The methods of analysis are mainly the cluster,correlation and regression,main components and discrimination analyses used in the maltivariate statistical analysis.The cluster analysis includes the observation value and variable cluster analyses while the regression analysis adopts the step-by-step regression method. In calculating the data of *Skeletonema costatum* biomass, the logarithm is taken while the data of wind and current directions are rejected.

2 Resnlts and discussion

2.1 Cluster analysis

2.1.1 Observation values cluser

The final results are shown in Fig.2. The observation values are obviously divided into two types: Type A is mainly composed of the merging samples (sample Nos. 1 ~ 24, 64 ~ 69) during the beginning and declining periods, which indicates that the environmental factors begin in the declining period to be

restored to the level before the occurrence of the red tide; Type B is mainly constituted by the merging samples (sample Nos. 25~56, 57~63) in the developing and maintenance periods, showing that the environmental conditions required for the maintenance of the increment of red tide and the huge species are more or less alike. In Type A, 34% of the samples belongs to Type B while in Type B, 25% of the samples to Type A. This result points to the complexity of the environmental factors during the occurrence of the red tide.

a. 5, 6, 7, 8, 9, 10, 11, 12, 16, 18, 19, 20, 21, 22, 23, 24, 28, 30, 31, 34, 35, 36, 42, 43, 48, 52, 66, 67, 68. __ :representing the samples of Type B. b. 1, 2, 13, 14, 25, 26, 32, 37, 38, 44, 49, 50, 57, 60, 61, 62. __ :representing the samples of Type A. c. 47, 55. d. 4, 51, 53, 54. e. 45, 64. f. 3, 33, 40, 46, 56, 59, 39. g. 15, 17, 65, 69. h. 27,29, 39, 58, 63.

Fig.2 Cluster dendrogram of sampling data

2.1.2 Variables cluster

Based on the results of the observation values cluster,we choose the environmental factors in the maintenance and developing periods for the oblique cluster of main components,whose results are (see Table 1 for the inter-cluster correlation coefficient): Type 1: atmospheric pressure, water temperature, salinity, NO_3^--N, PO_4^{3-}-P, SiO_3^{2-}-Si; Type 2: wind speed, turbidity, Fe and Mn; Type 3: DO, pH, NO_2^--N and NH_4^+-N.

This result seems to have run counter to our conventional knowledge and it is difficult to give a reasonable explanation for the aforementioned three types just from the angles of hydrology,meteorology and chemistry. When comparing the emvironmental factors in Type 1 with the factors with greater correlation coefficients, we find that in this type, except SiO_3^{2-}-Si, the atmospheric pressure, water temperature, salinity, NO_3^--N and PO_4^{3-}-P are just the important environmental factors obtained from the correlation analysis. The reason why these environmental factors are clustered to constitute a type may reflect the degree of similarity with respect to their influence on the red tide.

Tab. 1 Inter-cluster correlation coefficient

Type	1	2	3
1	1.000	−0.272	0.415
2	−0.271	1.000	−0.030
3	0.415	−0.030	1.000

2.2 Main components analysis

The basic idea of the main components analysis is the reduction of dimensions, a method of using smaller synthetic variables to express a number of observation variables while these synthetic variables often cannot be observed directly, but they usually reflect the essence of a thing[4].

Through calculation, we choose the first three components

$f_1 \sim 0.95x_t - 0.95x_s + 0.85x_{pH} - 0.78x_p + 0.81x_{NO_3^-} - 0.74x_{PO_4^{3-}} + 0.93x_{sio_3^{2-}} - 0.70x_{Fe}$

$f_2 \sim 0.74x_{DO} + 0.92x_{Tu} + 0.74x_{Mn}$

$f_3 \sim 0.71x_{u_w} - 0.79x_{NO_2^-} - 0.83x_{NH_4^+}$

See Table 2 for the cumulative percent of the first three main components.

Tab. 2 Cumulative percent of main components

Type	First main component	Second main component	Third main component
Percent	44.57	23.78	18.36
Accumulative percent	44.57	67.55	85.91

It can be found by carefully examining the first main component f_1 that, except SiO_3^{2-}-Si, the rest environmental factors are all important factors, which, together constituting the first main component, show that they affect the formation of red tide in a combined way.

2.3 Correlation and regression

2.3.1 Coefficient of correlation

Coefficients of correlation are obtained by making a correlation analysis of the environmental factors and the red tide biomass (Table3).The formation of red tide is closely related to atmospheric pressure, water temperature, salinity, pH, NO_3^--N, PO_4^{3-}-P and Fe. When the atmospheric pressure is lower, the high-temperature, low-salinity seawater environment is favourable to the formation of the *Skeletonema Costatum* red tide. For example, around the occurrence of this red tide, the ranges of increase and decrease for temperature and salinity are 2.01 and −6.15 respectively. And, during the *Skeletonema costatum* red tide which occurred in the Shengshan waters in August, 1991, the increase and decrease ranges of temperature and salinity were 1.3 and −2.6[3,7]. In the nutrients, the correlation of NO_3^--N, NO_2^--N and PO_4^{3-}-P to the red tide are much higher than NH_4^+-N and SiO_3^{2-}-Si; And the correlation of the micro metal element Fe to the red tide is higher than Mn.

Tab. 3 Coefficient of correlation between red tide and environmental factors

Environmental factors	r	Environmental factors	r
p	−0.877	NO_3^--N	0.606
u_w	−0.396	NO_2^--N	0.602
u_c	−0.250	NH_4^+-N	0.072
t	−0.851	PO_4^{3-}-P	−0.826
S	−0.979	SiO_3^{2-}-Si	−0.080
DO	0.576	Fe	0.686
pH	0.798	Mn	−0.490

The results obtained by integrating the three methods of variables cluster, main component analysis and correlation indicate that the important environmental factors contributing to the occurrence of this red tide are atmospheric pressare, water temperature, salinity, pH, NO_3^--N, PO_4^{3-}-P and Fe. The role of

SiO_3^{2-}-Si in this red tide is hard to determine and its coefficient of correlation to the red tide biomass is very small, but in the cluster and main components analysis, it is merged into the category of important environmental factors.

2.3.2 Step-by-step regression analysis

By using the method of step-by-step regression analysis we may screen out independents, from which the factors having significant effect on the dependent variables may be selected. Taking the red tide biomass in the developing and maintenance periods as dependent variable and the environmental factor as independent, under the significance level of 0.15, the step-by-step regression equation is obtained as follows:

$$y = 29.9 - 0.69x_s + 2.4x_{Fe} - 6.74x_{PO_4^{3-}\text{-P}},$$

$$r = 0.9452.$$

It is known from the above equation that the leading factors contributing to the formation of this *Skeletonema costatum* red tide are salinity, Fe and PO_4^{3-}-P. This is because *Skeletonema costatum* is a low-salinity planktonic diatom. Just as reported by Guo Yujie[9], this species is concentrated in the Huanghe and Changjiang estuaries in summer with a water temperature of about 25℃ and a salinity of 12~20. It can also survive in the mixed salt water (with salinity of 5~18) in the Jiulongjiang estuary of Xiamen[10]. Fe is the most important trace element affecting the growth of phytoplankton[12]. It has been often reported that Fe is the nutrition restriction factor in the ocean.The Fe brought by the river and the surface runoff has an obvious relationship with the occurrence of the local red tide. Fe is a cofactor in the enzyme system on which photosynthesis depends. In addition, in the reduction process of nitrite, Fe is a component of the reductase system and plays a significant role in augmenting reduction of the nitrogen in nitrous acid state by algae[11]. The conclusion that PO_4^{3-}-P is one of the leading factors contributing to the formation of this red tide is identical with the one drawn previously by Hong Junchao et al.[8] according to the Redfield rate.

2.4 Discrimination analysis

In this statistics, the linear discrimination functions are constructed in two ways. In making the discrimination, the variable data of sample are substituted and those with greater calculation values y are classified into the corresponding type.

2.4.1 Linear discrimination functions of five items of nutrient

The discrimination functions constituted by the nutrients NO_3^--N, NO_2^--N, NH_4^+-N, PO_4^{3-}-P and SiO_3^{2-}-Si are chosen as follows:

Non- red tide type:

$$y_1 = 24.35 + 0.34x_{NO_3^-} + 21.93x_{NO_2^-} + 0.46x_{NH_4^+} + 12.57x_{PO_4^{3-}} + 0.31x_{sio_3^{2-}} \quad (1)$$

Red tide type:

$$y_2 = 28.45 + 0.30x_{NO_3^-} + 25.24x_{NO_2^-} + 0.53x_{NH_4^+} + 14.78x_{PO_4^{3-}} + 0.35x_{sio_3^{2-}} \quad (2)$$

2.4.2 Linear discrimination functions of eleven items of environmental factor

The environmental factors of water temperature, salinity, DO, pH, NO_3^--N, NO_2^--N, NH_4^+-N, PO_4^{3-}-P, SiO_3^{2-}-Si, Fe and Mnare chosen and the linear discrimination functions obtained are calculated as follows:

Non-red tide type:

$$y_1 = -29.8 + 0.27x_t + 0.27x_s - 0.25x_{DO} + 5.84x_{pH} + 0.022x_{NO_3^-} - 2.8x_{NO_2^-} + 0.27x_{NH_4^+} + 1.87x_{po_4^{3-}} + 0.08x_{sio_3^{2-}} - 1.67x_{Fe} + 0.29x_{Mn} \quad (3)$$

Red tide type:

$$y_2 = -32.0 + 0.26x_t + 0.28x_s - 0.26x_{DO} + 6.1x_{pH} + 0.023x_{NO_3^-} - 2.9x_{NO_2^-} + 0.28x_{NH_4^+} + 1.9x_{PO_4^{3-}} + 0.09x_{SiO_3^{2-}} - 1.71x_{Fe} + 0.34x_{Mn} \quad (4)$$

2.4.3 Discrimination

Choose the environmental factors in the whole occurrence process of red tide in the Changjiang Estuary and substitute them into the equations (1) and (2), (3) and (4) for discrimination. See Table 4 for the results of discrimination.

In the case of making discrimination by using five items of nutrient, the rate of correct discrimination is extremely high for the non-red tide type, reaching 100% while that for the red tide type is 62.5%. As for the discrimination made by using the functions constituted by eleven environmental factors, the rate of correct discrimination is as high as 100% for the red tide type while that for the non-red tide type is relatively lower, only 33.3%. This is in coincidence with the conclusion of the observation values cluster, i.e., in the cluster of environmental factors, there exists the phenomenon that non-red tide type factors occur in the red tide type while red tide type factors occur in the non-red tide type.

3 Conclusions

(1) The common multivariate methods of analysis such as cluster, main components analysis, correlation and regression may be used to extract the environmental factors affecting the formation of red tide. (2)The results of observation values cluster show that in the occurrence process of the red tide, the environmental factors are similar in the developing and maintenance periods while in the declining period, the values of environmental factors begin to be restored to the normal levels. (3) The results obtained by using the methods of correlation, variables cluster and main components analysis are basically identical, from which it can be seen that the important factors affecting the occurrence of this red tide are: atmospheric pressure, water temperature, salinity, pH, NO_3^--N, PO_4^{3-}-P and Fe. (4) The step-by-step regression analysis establishes salinity, PO_4^{3-}-P and Fe as the leading factors affecting the occurrence of this red tide. (5) The analytical results of environmental factors by applying the linear discrimination functions in the occurrence of this red tide are satisfactory.

Acknowledgements

Our thanks go to Prof. Li Xianping from Fudan University, who provided us with guidance and Li Jianbin, who gave us support and help in the data processing and application of this paper.

Tab. 4 Discrimination results by using the data of No.2 observation station in the Changjiang Estuary[1)]

Type	Period	Time	Using Equations(1)and (2)				Using Equations(3)and (4)			
			Type 1	Type 2	Rate of correct discrimination (%)	Rate of wrong discrimination (%)	Type 1	Type 2	Rate of correct discrimination (%)	Rate of wrong discimination (%)
Type 1 (non-red tide type)	Declining Period 08-19 ~ 08-22	08-19 08:50	V[2)]				na: Fe, Mn			
		16:30	V					V		
		08-20 08:30	V				na: Fe,Mn			
		11:40	V		100	0		V	33.3	66.7
		08-21 07:10	V				na: Fe, Mn			
		08-22 08:20	V				V			
Type 2 (red tide type)	Developing Period 08-11 ~ 08-15	08-11 10:30		V				V		
		16:30		V				V		
		08-13 05:20		V				V		
		11:30		V			na: Fe, Mn			
		08-14 06:15		V			na: Fe, Mn			
		12:20		V						
		08-15 07:00		V	62.5	37.5	na: Fe, Mn	na: Fe, Mn	100	0
	Maintenance Period 08-16 ~ 08-19	08-16 07:30	V					V		
		09:30	V				na: Fe, Mn			
		11:30	V					V		
		13:30	V					V		
		15:30	V					V		
		17:30	V				na: Fe, Mn			
		9:30		V				V		
		21:30		V				V		
		08-17 08:30	V					V		

1) No.2 observation station (31°35'N, 122°33'E) is an auxiliary station in the C[13] continuous observation stations. During Aug16~22.1990, a *Skeletonema* costatum red tide occurred in this area,with a maximum bio-density of 18.2×10^6/dm^3.

2) "V"indicates correct discrimination.

References

[1] Qi Yuzao, Hong Ying, Lu Songhui et al. (1994) *Chattonella marina* Red Tide in the Dapeng Bay, South China Sea and its Origin [J]. *Oceanology and Limnology*, **25** (2): 132-138.

[2] Lin Yu, Zhuang Dongfa, Chen Xiaolin et al. (1994) Results of Enclosure Experiment for Preliminarily Analysing the Origin of Red Tide—Relationship between Several Physical-Chemical Factors and the Diatom Red Tide [J]. *Oceanology and Limnology*, **25** (2): 139-145.

[3] Huang Xiuqing Jiang Xiaoshan, Wang Guilan et al. (1994) Analysis of Environmental Factors in the Process of the *Skeletonema costatum* Red Tide in the Changjiang Estuary:Water Temperature, Salinity, DO and pH Characteristics [J]. *Marine Science Bulletin*, **13** (4): 35-40.

[4] Dong Dajun (1993) Guide to the Application of the SAS Software, Beijing: Electronics Industry Publishing House.

[5] Xu Ren, Hong Junchao, Wang Guilan et al. (1994) Red Tide Phenomena in the Changjiang Estuary and Its Adjacent Sea Areas [J]. *Marine Science Bulletin*, **13** (5): 25-29.

[6] Shen Hong and Hong Junchao (1994) Survey Report on the Whole Process of Occurrence of the *Skeletonema costatum* Red Tide in the Changjiang Estuary- Research on the Community Structure and Cytomorphology of phytoplankton[J]. *Oceanology and Limnology*, **25** (6): 591-595.

[7] Hong Junchao, Huang Xiuqing, Jiang Xiaoshan, et al. (1993) Analysis of the Leading Factors of the Occurrence Process of Skeletonema costatum Red Tide in the Shengshan Waters [J]. *Acta Oceanologica Sinica*, **15** (6): 135-141.

[8] Hong Junchao, Huang Xiuqing, Jiang Xiaoshan, et al. (1994) Survey Report on the Whole Process of Occurrence of the *Skeletonema costatum* Red Tide I. Condition of Nutrients [J]. *Oceanology and Limnology*, **25** (2): 179-184.

[9] Guo Yujie and Yang Zheyu (1992) Analysis of Phytoplanktonic Quantity Variations and Ecology in the Changjiang Estuary Region[J]. *Collected Marine Science Papers*, **33**: 167-189.

[10] Jin Dexiang, Chen Zhenfen, Liu Shicheng,et al. (1965) Effect of Temperature and Salinity on the Growth and Reproduction of Three Marine Planktonic Diatoms[J]. *Oceanology and Limnology*, 7(4): 373-384.

[11] Zhu Congju, Qi Yuzao, Guo Changbi, et al. (1994) Effect of Iron, Nitrogen, Phosphorus, Vitamin B_1 and B_{12} on the Growth of Marine *Prorocentrum*. *Oceanology and Limnology*, **25** (2): 168-172.

[12] Yamochi S. (1983) Mechanisms for the Outbreak of *Heterosigma akashiwo* Red Tide in the Osaka Bay, Japan Pt. I, Nutrient Factors Involved in Controlling the Growth of *Heterosigma akashiwo* Heda [J]. *J. Oceanogr. SOC Japan*, 39: 310-316.

Production of Aneuploid *Pinctada martensii* Dunker in Tetraploid Induction

He Maoxian（何毛贤）, Lin Yueguang（林岳光）, Shen Qi（沈琪）, Hu Jianxin（胡建兴）, Jiang Weiguo（姜卫国）
South China Sea Institute of Oceanology, Chinese Academy of Sciences, Guangzhou 510301

Abstract Aneuploidy embryos of *Pinctada martensii* Dunker are produced during tetraploid induction by inhibiting the first polar body in eggs from triploid fertilized with haploid sperms with cytochalasin B treatment. Chromosome analysis reveals that there are 88.18 ± 6.79% aneuploidy embryos, and 28.70% aneuploids in pearl oysters of one-year age. These aneuploids have five chromosomal conditions, such as 2n + 1(29), 2n + 2 (30), 3n − 2 (40), 3n − 1(41) and 3n + 1 (43). Results of growth measurement show that there is no significant difference between aneuploids (as a group) and diploids in body size and weight ($p > 0.10$), but the aneuploide is obviously different from triploid ($p < 0.01$). The mean body size and weight of aneuploids in diploid condition (2n ± 1 and 2n ± 2) are significantly smaller than those of diploids ($p < 0.01$), but aneuploids within triploid condition (3n ± 1 and 3n ± 2) are not smaller than diploids in body size and weight ($p > 0.1$).This study indicates *Pinctada martensii* Dunker could tolerate aneuploidy by 7 ~ 14% of the haploid genome, and that aneuploids of this species are viable under certain conditions.

Keywords aneuploid, triploid, *Pinctada martensii* Dunker

1 Introduction

Aneuploids are organisms in which member chromosomes of the haploid set are present in an unequal number of copies. In higher animals, aneuploids are often lethal or associated with growth retardation. In plants and lower animals, effects of aneuploids are less deleterious, many types of aneuploids are viable and could provide a rare opportunity for genetic analysis and breeding. For example, trisomics (2n+1) and monosomics (2n -1) could be used for chromosome genome manipulation and gene identification.

Although aneuploidy in molluscs is not well understood, preliminary data indicates that molluscs can tolerate some aneuploidy. Viable aneuploids have been identified among induced gynogenetic abalone *Haliotis discus hannai* (Fujino *et al*, 1990). Aneuploid mussels in natural population have been found (Martines-Exposito *et al.*, 1992). In the Pacific oyster (*Crassostrea gigas*), aneuploid cells have been observed in diploid individual, with higher frequencies found in smaller animals (Thiriot-Quievreux *et al.*, 1988). Viable aneuploid Pacific oysters have also been produced during polyploid induction (Guo and Allen, 1994; Guo *et al.*, 1998; Wang, 1998; Wang*et al.*, 1999). Aneuploid pearl oysters (*Pinctada martensii* Dunker) have been produced as by-products of tetraploid induction by crossing triploid females and diploid males with inhibition of the first polar body (PB1) and cytochalasin B (CB) treatment.

This study aims to study the incidence of aneuploid pearl oysters and the chromosome condition of

aneuploids. The growth measurement of aneuploids has also been made.

2 Materials and Methods

Triploid pearl oysters were produced by blocking PB1 with 0.5mg/L CB treatment in 1996. Ploidy of triploids was determined by counting the chromosome number of gill cells prior to spawning. Gametes were obtained by stripping. Eggs from triploid females were fertilized with sperm from normal diploid males in filtered seawater containing 0.06% ammonia and treated with 0.5mg/L CB to block the release of PB1. The treatment started 6 minutes after fertilization and lasted 15 minutes. Ploidy of embryos was determined by orcein stain (Hiroshi and Akihiko, 1974). Polidy of embryos was determined according to 2n=28, 3n=42, 4n=56, others as aneuploids (normal diploid has 28 chromosomes). About 100embryonic cells with good chromosome metaphases were counted for chromosome analysis in each group. The experiment was conducted on April 23, 1998.

On June 6, 1999, 230 pearl oysters were sampled. Each was numbered and measured for shell length (SL) and the whole body weight (BW) was weighed. A piece of gill was removed for chromosomal analysis. Ploidy was confirmed by examining no less than five chromosome metaphases with the same chromosome numbers from gill cells. Individuals with 28, 42 and 56 chromosomes were classified as diploid, triploid and tetraploid respectively; any derivation from the euploid chromosome numbers was classified as aneuploid. Growth comparison between aneuploid and euploid was conducted by Student's *t-test.*

3 Results

3.1 Frequency of aneuploids

Chromosome examination shows that most of embryonic cells are aneuploids, averagely 88.18 $\pm$6.79% (Table 1), and the chromosome number ranges widely.

Tab. 1 Ploidy rate of embryos in induced groups of triploid female-diploid male

	Diploid/%	Triploid/%	Tetraploid/%	Aneuploid/%
Group1	10.28	2.80	4.67	82.24
Group 2	5.88	2.94	8.82	82.35
Group 3	1.96	0.00	3.92	94.12
Group 4	2.00	0.00	4.00	94.00

There are 230 samples numbered to conduct examining ploidy. One hundred and fifteen pearl oysters have good chromosome metaphases and their ploidy is determined, the ploidy of others could not be confirmed due to few metaphases. Among these 115 pearl oysters, thirty-three pearl oysters are aneuploids, up to 28.70%, 33 (28.70%) have 28 chromosomes, 47 (40.87%) have 42 chromosomes, and 2 (1.74%) have 56 chromosomes (Table 2).

Tab. 2 Ploidy rate of adult pearl oysters in induced group of triploid female-diploid male

	Aneuploid	Diploid	Triploid	Tetraploid
Individuals	33	33	47	2
Percentage (%)	28.70	28.70	40.87	1.74

3.2 Types of aneuploids

In these aneuploids, there are ten pearl oysters with 29 chromosomes (2n+1), five with 30 chromosomes (2n+2), two with 40 chromosomes (3n-2), thirteen with 41 chromosomes (3n-1) and three with 43 chromosomes (3n+1)(Table 3). Representative metaphases from aneuploid *Pinctada martensii* are presented in Figure 1.

Tab. 3 Chromosome numbers of aneuploids and numbers of individuals observed

	2n + 1 (29)	2n + 2 (30)	3n - 2 (40)	3n - 1 (41)	3n + 1 (43)
Individuals	10	5	2	13	3
Percentage (%)	30.30	15.15	6.06	39.39	9.09

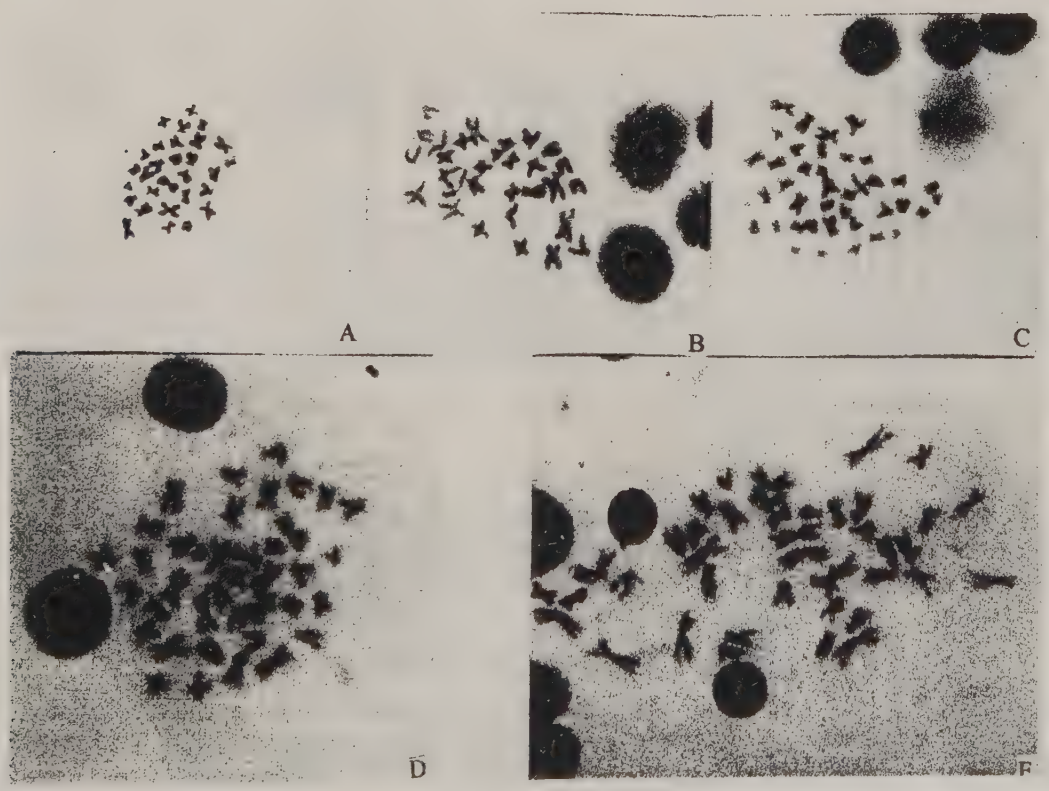

Fig. 1 Representative chromosome metaphases of adult aneuploid *Pinctada martensii* Dunker
A : 2n + 1 = 29; B : 2n + 2 = 30; C : 3n—2 = 40; D : 3n—1 = 41; E : 3n + 1 = 43

3.3 Growth comparison

Measurement of the body size and weight of *Pinctada martensii* Dunker shows that aneuploids (as a group) weighs 20.62g, and the shell length averages 4.91cm. Aneuploids are not significantly different from diploids in body size and weight ($p > 0.1$), but smaller than triploids in the mean shell length ($p < 0.01$) and body weight ($p < 0.001$). Triploids are bigger than diploids in SL ($p < 0.05$) and BW ($p < 0.01$). Aneuploids in triploid condition are smaller than triploids in BW ($p < 0.05$), almost identical to triploids in SL ($p > 0.1$), but not different from dipoids ($p > 0.1$). There are significant differences between aneuploids in diploid condition and diploids in SL and BW ($p < 0.01$). No difference is detected between aneuploids in triploid condition and aneuploids in diploid condition (Table 4). Tetraploids are not listed and examined due to their fewer numbers.

Tab. 4 Growth comparisons between aneuploids and euploids in *Pinctada martensii* Dunker

	Chromosome numbers	Individuals observed	Body weight (SE) /g	Shell length (SE) /cm
Diploid	28	33	23.38(4.75)	5.07 (0.40)
Triploid	42	47	28.01 (7.80)	5.37 (0.65)
Aneuploid		33	20.62 (7.83)	4.91 (0.78)
	29	10	20.19 (5.48)	4.84 (0.41)
	30	5	14.82 (5.27)	4.44 (0.58)
	40	2	21.65 (11.81)	5.18 (1.12)
	41	13	20.94 (7.44)	4.90 (0.91)
	43	3	29.63 (13.45)	5.90 (1.26)

No conclusion could be drawn concerning the effect of a particular aneuploid on the growth due to the small number of aneuploids observed. It is interesting to note, however, that an aneuploid with 43 chromosomes is the largest in body size (shell height 7.25cm), and the second largest in whole body weight (45g). Besides, pearl oysters with 30 chromosomes are the smallest of all aneuploids in body size. The whole body weight distribution of 115 samples except tetraploids is presented in Figure 2.

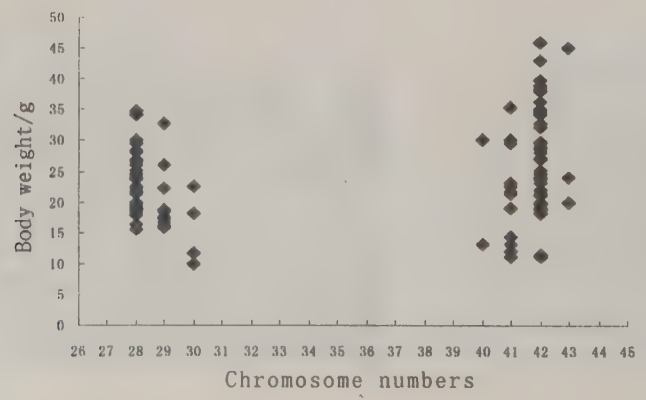

Fig. 2 The distribution of body weight of *Pinctada martensii* with different chromosome numbers

4 Discussion

4.1 The viability of aneuploids

In this study, aneuploid *Pinctada martensii* Dunker has been identified by crossing triploid females and diploid males with inhibition of PB1, and could survive to adult age, which indicates that aneuploid *Pinctada martensii* Dunker is viable. Viable aneuploids have also been found in a few species, such as abalone (Fujino *et al.*, 1990), Pacific oyster (Guo and Allen, 1994; Guo *et al.*, 1998; Wang *et al.*, 1999). These research findings suggest that molluscs can tolerate aneuploidy.

4.2 Tolerance to chromosome loss and gain

The percentage of aneuploid embryos is very high, about 88.18±6.79%, and their chromosome numbers distribute widely . But when they grow adult, the percentage of aneuploids decreases greatly, only 28.70%, and only five types of aneuploids do survive. These data reveal that the majority of aneuploids, especially those with chromosome numbers losing or gaining greatly do die during rearing. That is, *Pinctada martensii* Dunker can tolerate certain chromosome numbers (1~2 chromosomes) losing or gaining, about 7~14% of the haploid genome. Pacific oyster can tolerate 5~10% of the haploid genome loss and gain (Wang, 1998).

4.3 Growth comparison

The data of Table 4 show that the body size and weight of aneuploids are smaller than those of triploids, but not smaller than those of diploids. Aneuploids in diploid condition are smaller than diploids in SL and BW, which implies that aneuploid *Pinctada martensii* is possibly associated with growth retardation. Thiriot-Quievreux (1988) also reported that there are a lot of aneuploid cells in natural population (*C. gigas*) growing more slowly. But Wang (1998) reported that aneuploid oysters are bigger than normal diploids.

Although aneuploids in diploid condition are smaller than diploids in body size and weight, aneuploids in triploid condition are not smaller than diploids. It maybe shows that 1~2 chromosome loss and gain is well within the tolerated range for triploids and therefore have no observed effects on the body size. Aneuploids with the same number of chromosomes vary considerably in the body size and weight, which is maybe caused by different genes on the different chromosome. But there may be other reasons. The comprehensive study on the effect of different aneuploids on the organism will be a very important research task in future.

4.4 Incidence of aneuploids

In this study, aneuploid pearl oysters are produced by inhibiting PB1 in eggs from triploids with CB treatment. CB treatment changes greatly the meiotic segregation, and the imbalance segregation of chromosomes in meiosis II may result in aneuploids (unpublished). The same results have been reported on Pacific oyster (Que *et al*, 1997). Although aneuploids could be produced during the induction of triploid from diploid-diploid cross in Pacific oyster (Wang, 1998), there have been no similar reports on *Pinctada martensii*. In tetraploid-diploid cross, Wang (1998) detected aneuploid Pacific oyster, and suggested that aneuploids are resulted from the erroneous meiotic segregation in paternal tetraploids. In addition, water pollution, radiation, chemical induction in natural environment may cause the production of aneuploids (Dixon, 1992).

4.5 Importance of aneuploids

Certain aneuploids may be useful for genetics analysis, such as gene transfer and gene location.

Sears (1956) reported that aneuploids help the transfer of rust resistance from a wild grass (*Aegilops umbellulata*). The gene of LC_2 was located on chromosome NO 6 by use of a particular monosomic in cotton (Endrizzi and Kohd, 1966). Besides, certain aneuploids may be useful in breeding. Guo and Allen (1994) discovered that an aneuploid with 38 chromosomes is the largest individual among a cohort of 30 polyploid oysters. An aneuploid with 29 chromosomes is also the largest oyster in one group of tetraploid crossing diploid (Wang *et al.*, 1999). In this study, an aneuploid with 43 chromose is the largest in size. This suggests that some aneuploids possibly have the growth advantage and the potential application to aquaculture through breeding and selection. So it is of great theoretical and practical importance to study aneuplooids.

Acknowledgments

This study is supported by the "863" Project in China (#863-819-01-03) and the Natural Science Foundation of Guangdong, China (#990315).

References

[1] Dixon D R (1982) Aneuploidy in mussel embryos (*Mytilus edulis* L.) originating from a polluted dock. *Mar. Biol. Lett.*, 3: 155-161.

[2] Endrizzi J E and Kohd R J (1966) Use of telosomes in mapping three chromosomes in cotton. Genetics, 54: 535-550.

[3] Fujino K, Arai K, Wadarl K, *et al.* (1990) Induction of gynogentic diploid by inhibiting 2nd meiosis in the Pacific abalone. *Bull. Jap. Soc.Sci. Fisheries*, (56): 1755-1763.

[4] Guo X and Allen Jr S K (1994) Viable tetraploids in the Pacific oyster (*Crassostrea gigas* Thunberg) produced by inhibiting polar body 1 in eggs from triploid. *Mol. Mar. Biol. Biotechnol.*, **3** (1): 42-50.

[5] Guo X, Yang H, Landau B J, *et al.* (1998) The creation of aneuploid families in the Pacific oyster, *Crasso strea gigas* Thunberg. *J. Shellfish Res.*, **17** (1): 328.

[6] Hiroshi I, Akihiko I. (1974) Chromosome numbers of ten species in four families of Preriomophia (Bivalvia). *Venus*, **33** (3): 129-137.

[7] Jing W G, Li Y, Lin Y G, *et al.* (1990) Observation on the gonad of pearl oyster *Pinctada martensii* (D.). *Tropic Oceanology*, **9** (1): 24-30.

[8] Martines-Exposito M J, Martines-Large A, Pasantes J, *et al.* (1992) A preliminary study of aneuploidy in natural population in the G.[genus] *Mytilus*. Cuad. Area Cienc. Mar. Semim. Estud Galegos., 6: 49-55.

[9] Que H, Guo X, Zhang F, *et al.* (1997) Chromosome segregation in fertilized eggs from triploid oysters, *Crassostrea gigas* (Thunberg) following inhibition of polar body 1. *Biol. Bull.*, 193: 14-19.

[10] Sears E R. (1956) The transfer of leaf rust resistance from*Aegilops umbellulata* to wheat. Brookhaven Symp.Biol., 9: 1-22.

[11] Thiriot-Quievreux C, Noel T, Bougrier S, *et al.* (1988) Relationships between aneuploidy and growth rate in pair matings of the oyster *Crassostrea gigas*. *Aquaculture*, **75** (1-2): 89-96.

[12] Wang Z P (1998) Basic study on genetics in triploid Pacific oyster (*Crassostrea gigas*). Dissertation of doctor, Ocean University of Qingdao.

[13] Wang Z, Guo X, Allen S K, *et al.* (1999) Aneuploid the Pacific oyster, *Crassostrea gigas* (Thunberg) as incidental from triploid production. *Aquacuture*, 173: 347-357.

Application of Microbial BOD Sensors in Marine Monitoring

Zhang Yue (张 悦), Wang Jianlong (王建龙), Li Huazi (李花子),
Shi Hanchang (施汉昌), Zhu Jianrong (竺建荣)
State Key Joint Laboratory of Environment Simulation and Pollution Control, Department of Environmental Science and Engineering, Tsinghua University, Beijing 100084

Abstract A strain of yeast, which can endure high osmotic pressure, is employed for the sensitive material of the microbial BOD sensor. Two immobilization methods are used, i.e. calcium alginate gel beads and PVA gel beads. The results show that the PVA gel beads is better. The influences of osmosis and heavy metal ions on the yeast entrapped in the PVA gel beads are also studied in the experiment.

Keywords Biochemical oxygen demand, microbial sensor, yeast, immobilized cells, marine pollution, monitoring

The pollution in water and sewage by various organic matters is difficult and unnecessary to analyse individually, so biochemical oxygen demand (BOD) is a widely used parameter for the determination of biodegradable organic compounds. The conventional method to determine BOD_5 which needs 5 days' incubation at 20 ± 1 ℃ in the dark, is universally accepted. Dissolved oxygen is measured initially and after incubation, and the BOD_5 is computed from the difference between initial and final DO[1]. Although BOD_5 is a good indicator of the organic pollutant concentration level in the water, this method has many shortcomings, such as complicated procedure, poor reproducibility, too much consumption of time and manpower. It is therefore necessary to develop the new methods that could determine BOD rapidly, simply, adequately and automatically, and the sensors that could be widely used in the in situ monitoring.

The sensor is an apparatus that can detect the monitoring matters and then convert them into the quantitative signals. It is usually composed of detecting element, converting unit, corresponding mechanical construction and electronic circuit[2]. The detecting elements of the biosensor are immobilized live materials such as enzyme, microbe, animal or plant cell, animal or plant tissue, antigen or antibody. Different from computing the absolute oxygen consumption of 5-day BOD method, the BOD sensor only cares about the initial rate of assimilation of the substrate by the microbial system. Since the rate of assimilation is a function of the BOD of the solution, the linear relationship between the sensor BOD and the 5-day BOD can be determined by estimating the standard solution.

Up to the present, the studies on BOD sensors have mainly been focused on the determination of municipal sewage and natural fresh waters. However the reports on the special BOD sensor for seawater have not been seen. Therefore, aiming at the high saline concentration of seawater, we develop a microbial BOD sensor. A strain of yeast, which can endure high osmotic pressure, is employed for the detecting material. The characters of operational simplicity and portability make it available for the marine monitoring.

1 Experimental Equipment

1.1 Experimental equipment

Figure 1 shows the schematic construction of the microbial BOD sensor used in the present study. Its working system comprises magnetic stirrer (TB-600), self-made isothermal water bath, micro aeration pipe (CTB-208), monitoring cell (150ml), DO instrument (YSI-58) and recorder.

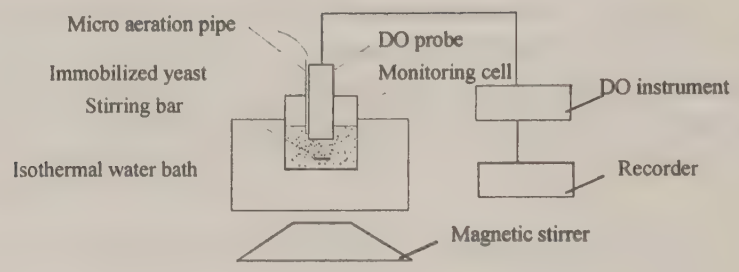

Fig. 1 Experimental set-up for BOD measurement

1.2 Experimental procedure

15 g wet immobilized yeast and 100 ml deionized water are put in the measuring cell, then stirred by a magnetic stirrer and aerated by a micro aeration pipe at a constant flow rate of 24L/h. After DO in the mixed solution is in a steady state under pH5.0, 30℃, 10 ml solution to be determined is put in the mixed solution until the DO is in a new steady state. The difference between the two DOs is thought the sensor's BOD. The experimental results indicate that the calibration curve has good linearity and reproducibility.

1.3 Yeast

The microorganism employed is a strain of aerobic yeast with good fermentation ability, which has the characters of a large spectrum of substances and osmotic pressure endurance. In addition, the yeast can be stored under drying air and its enzyme activity can also maintain for a long time The yeast multiplies by budding, and its lifetime is 1.5~2.0h[3].

The potato-glucose medium is employed as the culture medium[4]. The yeast is incubated at 30°C, 200r/min for 48h in a rotating shaker. Then it is gathered by being centrifuged at 3000r/min for 10 min, and washed twice with deionized water.

1.4 Immobilization of yeast

Calcium alginate gel method: Yeast with 5g wet weight is suspended in 10ml of 0.9% NaCl solution and then mixed up with 12.5ml of 2% sodium alginate solution. This mixture is then dropped into a 1% calcium chloride solution to form 2mm diameter spherical beads with syringes (0.40mmI.D. needle). The beads are taken out and washed with 0.9% NaCl solution after 1h[5].

PVA gel method: Yeast with 5g wet weight is suspended in 5mL deionized water and then mixed up with 10ml aqueous solution containing 10% PVA and 1% sodium alginate. This mixture is then dropped into a saturated boric acid solution with 1% calcium chloride to form 2mm diameter spherical beads with syringes (0.40mm I.D. needle). In order to complete gelation inside the beads, these beads

are kept in this solution for 24h, then taken out and washed with 0.9% NaCl solution[6].

The two kinds of immobilized yeasts can both be preserved after being dried and used after being activated for 24h in the aerated nutrient solution.

1.5 BOD5 standard solution

A solution containing glucose (150mg/L) and glutamic acid (150mg/L) with a BOD value of (198 ± 30.5) mg/L BOD is employed as a standard solution (GGA) for calibration of the BOD sensor (APHA, 1995). Different BOD concentrations can be obtained by diluting with deionized water[7].

2 Experimental results

2.1 Comparison of the materials for immobilization of cells

The experiment shows that the preparation of Calcium alginate gel is relatively simple, but it has some shortages as follows: (1) It can't endure high temperature. The gel beads swell and dissolve at 35℃; (2) It can't endure acid and alkali. When pH is under 3 or over 11, the beads' diameter increases from 2mm to 4mm, and the weight increases 3 times; (3) It can't endure osmotic pressure. The gel beads become soft after being immersed in the 0.5% NaCl solution for 30min, break when being immersed in the 1% NaCl solution, and dissolve entirely after being immersed in the 3% NaCl solution for 30min. The gel beads become soft after being placed into the seawater for 24h and the gel strength becomes weak. (4) It can swell gradually by absorbing the water. The gel beads' weight increases from 15g to 23.11g after 20-day usage; (5) It can adsorb heavy metal ion and color seriously, and it will swell and break by absorption; (6) It is difficult to dry and restore.

These weaknesses do not appear at PVA gel beads, except for the coloring. But its preparation is relatively complex.

The conclusion is that PVA is better as the material of immobilization of cells for the sensor.

2.2 Effect of osmotic pressure

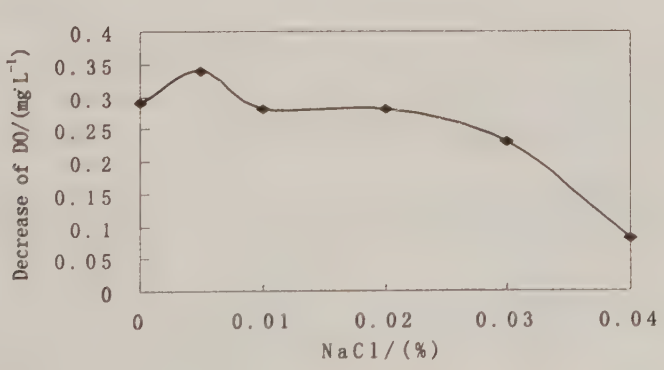

Fig. 2 Effect of NaCl on the sensor response

The yeast's metabolism is usually affected by the high osmotic pressure of seawater, so the effect of the concentration of NaCl solution on the biosensor is measured. The result is showed in Fig. 2.

2.3 Effect of heavy metal ion

Lots of industrial waste water contains the heavy metal ion and the activity of microbe is usually inhibited by the heavy metal ion due to its toxicity. So, it is necessary to study the effect of the heavy metal ion on the BOD sensor. The effect of Cu^{2+}, Cd^{2+}, Ni^{2+}, Mn^{2+}, Zn^{2+}, Fe^{2+}, Al^{3+} on the activity of immobilized yeast has been studied. The effect of the metal ion on the BOD measurement can be best seen from the current response curve of the sensor as shown in Fig.3. 10mg/L of cupric ion significantly suppresses the microbial assimilation of the substrate resulting in a lower measured BOD value of the substrate. The inhibition of Cu^{2+} on immobilized yeast is showed in Fig.4, and the effect of other heavy metal ions on the immobilized yeast is showed in Table 1.

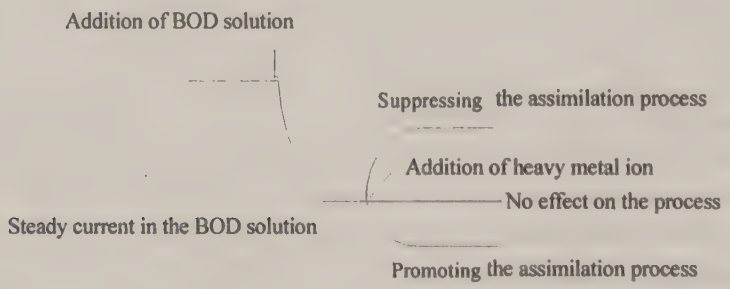
Addition of BOD solution
Suppressing the assimilation process
Addition of heavy metal ion
No effect on the process
Steady current in the BOD solution
Promoting the assimilation process

Fig. 3 Typical sensor current-time curve during BOD measurement in the presence of heavy metal ions

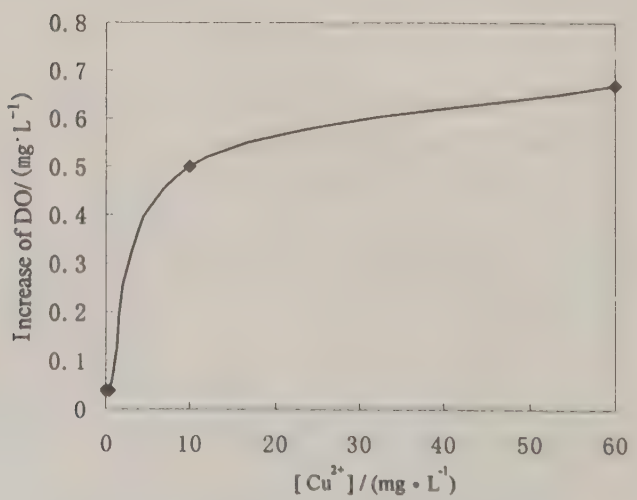

Fig. 4 Effect of Cu^{2+} on the sensor response

Tab. 1 Effect of metal ion concentration on the sensor response

Metal ion concentration /(mg • L^{-1})	Increase of DO /(mg • L^{-1})					
	Cd^{2+}	Ni^{2+}	Mn^{2+}	Zn^{2+}	Fe^{2+}	Al^{3+}
10	0.07	0.06	0.05	0.03	0.00	0.13
20	0.07	0.13	0.05	0.09	0.00	0.19
30	0.11	0.14	0.15	0.10	0.02	0.31
40	0.38	0.59	0.16	0.51	0.20	0.50

3 Conclusions

(1) The detection of BOD is difficult in the marine pollution monitoring, for it is far from the municipal sewage treatment plant that can provide the seed microbe. The yeast can be stored for a long period after being dried and restored immediately after being immersed in nutrient solution. This feature makes it suitable for marine monitoring.

(2) The transmitting performance of the cell membrane is affected by salt solution, which makes the activity of yeast increase or decrease. Because of the 10 times dilution of the sample, the saline concentration of real seawater is lower than 4 in the monitoring cell. This concentration is far lower than the endurance of the yeast, so it can work normally in the marine monitoring.

(3) The PVA-boric acid can endure osmotic pressure as the material of immobilized yeast. The gel beads does not swell and its strength does not decrease after being immersed in the seawater for 10 days. Therefore, it can be used as the immobilizing material for monitoring the BOD of seawater.

(4) Although the immobilized yeast has some degree of endurance to various heavy metal ions, they can have long-term effect on the yeast. They can reduce the activity of yeast and shorten the lifetime of the immobilized yeast.

References

[1] Zhanpeng J, Wanpeng Z (1990) Monitoring for Environmental Engineering. Tsinghua University Press, 304.

[2] Chunxiang X, Yuanming L, Yuqi L, et al. (1993) Biosensor and its Application. Science Press, 1-2.

[3] Hao X, Junhua H, Guoqiang C, et al. (1991) Fundamentals and Application of industrial Microorganism. Science Press, 110-112.

[4] Tianchou C (1995) Preparation and Application of Microorganism Medium. Chinese Agricultural Press, 494.

[5] Nomura Y, Lkebukuro K, Yokoyama K, et al. (1995) A Novel Microbial Sensor for Anionic Surfactant Determination. *Analytical Letters*, **27** (15) 3095-3108.

[6] Haobin Y, Xinghua G, Daiwen L, et al. (1996) Lactic Acid Bacteria — Biological Fundamentals and Application. Chinese Light Industry Press, 215.

[7] American Public Health Association, American Water Works Association, Water Environment Federation, (1995) Standard Methods for the Examination of Water and Wastewater. American Public Health Association Publication Office, 5-6.

Species and Distribution of Mangroves in the Fujian Coastal Area

Wang Wenqing（王文卿）, Zhao Mengli（赵萌莉）, Deng Chuanyuan（邓传远）, and Lin Peng（林鹏）
School of Life Science, Xiamen University, Xiamen 361005

Abstract On the basis of an investigation on the mangroves in Fujian from November 1998 to January 1999, the species composition, area, distribution, artificial afforestation of mangroves and the factors restricting the development of mangroves in Fujian are discussed in the paper. Some suggestions on how to develop mangroves in Fujian have been put forward.

Keywords Fujian, mangroves, distribution, area, afforestation, investigation

As all circles of the society have attached more and more importance to the mangroves in recent years, not only the original mangroves have been better conserved, but also mangrove afforestation activities have been conducted on various scales in different localities, which have made a number of achievements. However, to plant mangroves on the beach tidal flat is a new subjuect for the forestry department, the afforestation activities in various places lack the necessary techniques and are carried out with some blindness, thus causing some undue losses and also dampening the enthusiasm for afforestation in some localities. How much area of mangrove is left now in Fujian? How are the mangroves distributed ? How effective is the mangrove afforestation in various places? What are the main factors restricting the development of mangroves in Fujian? What kind of counter-measures should be taken? With these questions in mind, we conducted this investigation from the last ten days of November, 1998 to January, 1999, lasting 75 days. The area of mangroves mentioned in this report has been estimated according to the data provided by the local forestry department and the on-the-spot observations made by the investigators.

1 Species and Distribution of Mangroves in Fujian

1.1 Species and distribution of mangrove plants in Fujian

See Table 1 for the species and distribution of mangroves in Fujian. During this investigation, the coastal counties and cities, especially Fuding, Fu'an, Changle, Fuqing and Tong'an, all pose the same question: How to enrich the species of mangroves for afforestation. At present, except the School of Biology of the Xiamen University which has planned to plant *Bruguiera gymnorrhiza*, *Rhizophora stylosa* and *Sonneratia apetala* in Haicang, Xiamen, all the other mangrove afforestation plans which have been or are to be implemented use *Kandelia candel*. Although *Kandelia candel* is the most cold resistant among all mangrove species, it has a low salt tolerance so that it may grow well on the tidal flat near the estuary with freshwater supply, but cannot grow well on the tidal flat without freshwater sources, where the rate of afforestation success is low. Moreover, in some places, such as Fuding and Fu'an, it may be subjected to serious insect pests.

Tab. 1 Species and distribution of mangrove and semi-mangrove species in Fujian coastal area

	Family	Species	Distribution area
Mangrove species	Acanthaceae	*Acanthus ilicifolius*	Longhai, Yunxiao
		A. xiamenensis	Longhai
	Myrsinaceae	*Aegiceras corniculatum*	Hui' an, Quanzhou,Xiamen, Longhai. Yunxiao
	Rhizophoraceae	*Bruguiera gymnorrhiza*	Longhai, Yunxiao
		*B. sexangula**	Longhai
		B. s. var. *rhynochopetala**	Longhai
		Kandelia candel	Costal areas throughout the province
		*Rhizophora stylosa**	Longhai
	Verbenaceae	*Avicennia marina*	Hui'an, Quanzhou,Xiamen, Longhai, Yunxiao
	Sonneratiaceae	*Sonneratia apetala**	Longhai
Semi-mangrove species	Barringtoniaceae	*Barringtonia racemosa**	Campus of Xiamen Univercity
	Malvaceae	*Hibiscus tiliaceus*	Coastal areas throughout the province
		*H. hamabo***	Yunxiao
	Apocynaceae	*Cebera manghas**	Xiamen Botanical Garden

Note: *Introduced from outside the province. ** Found in this investigation.

Fujian is the northernmost province in China where mangroves are naturally distributed, and also one of the earliest provinces known so far in China to plant mangroves artificially. According to the account in the "Forestry Chronicles" of Zhangzhou compiled in 1933, as early as 1882, overseas Chinese brought mangrove seeds from southeast Asia to plant them in Zhangzhou. In the 1920s, in oredr to change the condition of his hometown, Liaodong Village of Jiaomei Town, being attacked all the year round by storm surges, Guo Chunyang, an Indonesian overseas Chinese, brought *Kandelia candel* seedlings from Indonesia and planted them on the tidal flat beyond the coastal dyke of Liaodong Village, which turned out to be a success. In 1932, Guo Meicheng et al., overseas Chinese residing in Singapore, brought back *Kandelia candel* seedlings and successfully planted them in Xiaguo Village of Fugong Town[1]. In the late 1980s, based on the numerous in-situ investigations and painstaking laboratory researches, the mangrove scientific research group of Xiamen University successfully introduced *Bruguiera gymnorrhiza*, *Rhizophora stylosa*, *B. sexangula* and *B. s.*var.*rhynochopetala*, among which *Bruguiera gymnorrhiza*, *B. sexangnla* and *B. s.*var. *rhynochopetala* can now blossom, bear fruit and reproduce progeny. The semi-mangrove plant,*Cebra manghas*, introduced by the Wanshi Botanical Garden in the 1980s, has now grown to a height of 3m and has blossomed and borne fruits. In 1992, the Mangrove Scientific Research Group of Xiamen University introduced from Hainan the semi-mangrove plant *Barringtonia racemosa*, which blossomed, bore fruits and reproduced progeny two years later and for which the reproductive technologies such as seeds sowing and making a cuttage have all been solved[2]. *Barringtonia racemosa* has been brought to the attention of the horiculture department due to its high ornamental value. In 1997, the Mangrove Scientific Research Group failed in their attempt to introduce the mangrove species *Nypa fruticans* of palmae, but this work is being continued. What is worth mentioning is *Sonnerata apetala*. In 1996, the Mangrove Scientific Research Group of Xiamen

University introduced it from Hainan, planted it on the tidal flat of Fugong Town, Longhai City, where it has now grown to as high as 5m and can blossom and bear fruits. During this investigation, we didn't find *Acrostichum aureum* and *Excoecaria agallocha*, but they were reported to have been distributed in Fujian before[3,4,5]. *Hibiscus tiliaceus*, a highly salt-tolerant semi-mangrove plant, has been widely cultured in the coastal counties and cities of Fujian as an afforested tree. *H. hamabo* is a new distribution species of Fujian found in this investigation and a small number of them are distributed in Dongqi Village of Dongxia Town at the estuary of Zhangjiang River, Yunxiao County. This species is naturally distributed in the Zhoushan Archipelago, where it is widely cultured as an afforested tree due to its large and beautiful flowers. Besides, it is a good kind of trees for resisting the tide and protecting the coastal embankment[6].

Now Fujian has 10 species of mangrove plants in seven genuses, 5 families (of which 4 species are introduced ones), 4 species in 2 genera and 1 family more than those before the 1990s, and 4 species of semi-mangrove plants in three genera, 3 families (of which 2 species are introduced ones). The varieties of mangrove species in Fujian decreases from south to north, the most in the Zhangzhou region with 10 species (including the introduced ones), 3 species in Xiamen, Quanzhou and Putian respectively, and only one species, *Kandelia candel*, to the north of Putian. Thus it can be seen that Zhangzhou has become the distribution centre of mangrove species in Fujian.

1.2 The way out for solving the shortage of species in the course of mangrove afforestationin Fujian

In order to solve the shortage of species in the mangrove afforestation in Fujian, it is necessary to take measures in two ways: firstly, to tap the available germplasm resources of mangroves in Fujian, which is a cost-effective way; secondly, to lose no time in introducing new species from outside the province. More specifically, we may start with the following:

(1) Strengthening research on the seedlings raising and afforestation technologies for the successfully introduced varieties such as *Rhizophora stylosa*, *B. sexangula*, *B.s.*var.*rhynochopetala*, *Bruguiera gymnorrhiza* and *Sonneratia apetala*, so as to expand the area of cultivation;

(2) Carrying out follow-up research on the varieties which have been successfully introduced, such as phenological observation, physiological and ecological variations after introduction, etc., so as to tap their potentialities and make preparations for their migration to the north;

(3) Introducing again *Excoecaria agallocha* and *Acrostichum aureum* which used to be distributed in Fujian but are now seldom found, carrying out researches on the seedlings-raising and afforestation technologies and expanding the area of cultivation;

(4) Conducting research on the seedlings-raising and afforestation technologies of *Avicennia marina* and *Aegiceras corniculatum*, which are the most cold resistant mangrove species except *Kandelia candel*. And *Avicennia marina*, which is highly salt tolerant, may be distributed in Fuqing in the northernmost[5]. As suggested by Lin Huilai with the Third Institute of Oceanography, State Oceanic Administration, *Aegiceras corniculatum* used to be distributed in Nanzheng near Jiangjing of Fuqing in the 1960s, but now *Avicennia marina* and *Aegiceras corniculatum* no longer exist in Fuqing. Now near Luoyangqiao of Hui'an there are *Avicennia marina* and *Aegiceras corniculatum* forests which are distributed northernmost in China. In the 1960s, the Subtropic Crops Research Institute of Zhejiang Province introduced *Avicennia marina* from Fujian to Rui'an of Zhejiang, where it could grow slowly and still survive half a year later, but then during the "Cultural Revolution", it gradually died out due to lack of management[1]. It is not certain whether it is because of artificial destruction or unfavourable

natural conditions. Thus it can be seen that *Avicennia marina* and *Aegiceras corniculatum* in Fujian have the potentialities of being moved further north;

(5) Continuing to do the work of introducing mangroves and giving full play to the advantages of Xiamen University in the mangrove research to introduce new species from the South. More promising varieties to be introduced include *Heritiera littoralis, Lumnitzera racemosa, Ceriops tagal, Pongamia pinnata* and *Thespesia populnea.*

2 Mangroves in Fujian (including the natural forest and the forest which is artificially planted, but closed to become forest)

Yunxiao: On the both banks of the Zhangjiang River estuary is distributed a large area of mangrove forest, with an area of nearly 53.3hm^2. The main species include *Kandelia candel, Aegiceras corniculatum, Avicennia marina, Bruguiera gymnorrhiza* and *Acanthus ilicifolius.* In the forest there is trifoliate jewelvine (*Derris trifoliata*), but no *Excoecaria agallocha* and *Acrostichum aureum* were found during the investigation. Local residents said that some people once had come specially from Guangdong to Yunxiao to gather *Acanthus ilicifolius. Bruguiera gymnorrhiza* which used to be a dominant species several dozen years ago is now seldom found and its individual number is less than 200. Besides, its plant is low and it seldom blossoms and bears fruits, so it has become an occasional species. In Dongqi Village of Dongxia Town nearly 6 km away from Zhuta Village, there is a large individul of *Bruguiera gymnorrhiza,* whose trunk diameter exceeds 20cm for the larger ones but the plant is not coming along fine. The local mangroves include mainly: the *Avicennia marina* formation, the *Kandelia candel* formation, the *Aegiceras corniculatum* formation and the *Aegiceras corniculatum* + *Kandelia candel* formation, with a forest height of 1.5~2m, the highest being 3m and a canopy density of over 95%. The mangroves at the Zhangjiang River estuary, Yunxiao are now the most complete natural mangrove vegetation with the largest area joined together in Fujian. They are also the northern boundary of the naturally distributed *Bruguiera gymnorrhiza* and possess some value for scientific research. Thanks to the great efforts made by the Forestry Bureau of Yunxiao County, a nature reserve was established in 1997 for this mangrove forest, which has since been under good protection.

Longhai: The Jiulong River estuary is an area in Fujian where more mangroves are distributed. The existing mangrove plant species include *Kandelia candel, Aegiceras corniculatum, Avicennia marina, Acanthus ilicifolius* and *A · xiamenensis.* Besides, the Mangrove Scientific Research Gronp of Xiamen University has opened up an introduction garden in Fugong Town of Longhai City and has successively introduced *Bruguiera gymnorrhiza, Rhizophora stylosa, B. sexangula, B.s.*var. *rhynochopetala* and *Sonneratia apetala,* which turned out to be a success. This has greatly enriched the mangrove species in Fujian, thus making it an area with the most mangrove species in Fujian. The main communities are: *Kandelia candel* forest, *Aegiceras corniculatum* forest, *Avicennia marina* forest and*Aegiceras corniculatum* + *Kandelia candel* forest. In February, 1988, upon approval by the Provincial Peoples Government, the Longhai Mangrove Nature Reserve at the Jiulongjiang Estuary was established. With a total area of about 106.7hm^2, the mangroves are distributed in Fugong, Zini, Jiaomei and Gangwei. As the first mangrove reserve in Fujian, it is one of the world's *Kandelia candel* centres. According to records, *Kandelia candel* here can grow to as high as 10m[1], which is rarely seen in other places both at home and abroad. Since the establishment of the nature reserve, afforestation activities of various scales have been carried out every year and the area of forest land has now amounted to 233.3hm^2.

Xiamen: Xiamen boasts a coastline as long as 254 km and a wide area of tidal flat. Besides, situated at the outlet of the Jiulong River eestuary, it has sufficient freshwater supply. So it is very favourable for the growth of mangroves and used to have a large area of mangroves. In 1979, Xiamen still had nearly 106.7hm^2 of mangroves. In recent years, however, the area of mangroves has dramatically decreased. It can be seen from Table 2 that only 31.8hm^2 of the natural mangrove forests in Xiamen City have left with their total area less than 1/3 of that in 1979. Moreover, the largest *Avicennia marina* forest at the Dongyu Bay, Haicong of Xiamen has been seriously damaged by engineering construction and its area has witnessed a sharp decline.

Tab. 2 Distribution of mangroves in Xiamen area

Place	Area (hm^2)	Community type	Height	Condition of conservation
Dongyu Bay, Haicang	23.3	*Avicennia marin* forest	1.0	seviously damaged
Haicang wharf	0.3	*Avicennia marina+Aegiceras can* forest	1.5	enclosed inside the ship lock
Houjing Village, Haicang Town	0.1	*Kandelia candel* forest	1.5 ~ 2.0	mediocre
Qingjiao, Haicang	0.3	*Kandelia cande* forest	2.0	good
Xinglin	0.4	*Avicennia marin* forest	1.5	mediocre
Fenglin, Jimei	7.3	*Avicennia marin* forest	1.4	good
Eyu, Tong'an	0.1	*Avicennia marin* forest	1.0	mediocre
Total	31.8	–	–	–

Quanzhou: Now only *Avicennia marina, kanedlia candel* and *Aegiceras corniculatum* are left alive near Houzhu Harbour. There is only one *Kandelia candel* , which is about 40cm high and is doing well. *Avicennia marina* is 0.5m high with developed aerating roots which cover an area of about 50m^2 and it is coming along fine. For *Aegiceras corniculatum*, there are only about twenty clusters left, which are 0.5m high and are gowing well. These mangrove plants are protected from the damage by refuse as they are enclosed within the dykes. As seen from the beach face distribution, there used to be large areas of mangrove distributed, which were later damaged due to harbour construction. This has been borne out by the stubs existing in the tidal flat and the introduction given by the local people. In addition, the invasion of spartina into the beach face is one of the causes for the dying-out of mangroves.

Hui'an: Mainly distributed near Luoyangqiao, the mangrove species include *Avicennia marina, Kandelia candel* and *Aegiceras corniculatum.* Here the area of mangroves is large and the area of forest land is estimated at about 33.3hm^2. The communitys types are many, including the pure *Aegiceras corniculatum* forest, the pure *Avicennia marina*forest and the *Aegiceras corniculatum+Avicennia marina* forest with a coenosium height of 1~1.5m. *Kandlia candel* is scattered in between *Aegiceras corniculatum* and *Avicennia marina* with its maxinum height reaching 2m. The pure *Aegiceras corniculatum* forest is mostly distributed over the inner beach and the pure *Avicennia marina* forest mostly over the outer beach, but there are some pure *Avicennia marina* forests distributed over the inner beach. The physiognomy is neat and the cover degree may reach over 90% and the natural regeneration is fine. The mangroves here have been seriously damaged due to aquaculture. Now the main problem lies in the fact that the culture of the razor clam and other clams vies with mangroves for land. But in recent years, the aquaculture industry tends to decline and many fish ponds, razor clam and oyster farms

now lie waste and are occupied by the mangrove plants again. The tidal flat here has a large area and the surface is smooth, and here is also the northern boundary of natural distribution of *Avicennia marina* and *Aegiceras corniculatum* in the mainland. It is adjacent to the major historical and cultural sites under state protection —Luoyangqiao and the famous historical and cultural city Quanzhou, and the Fuzhou-Xiamen Expressway passes through near the mangrove forest. If the damage to the mangroves could be checked and appropriate artificial measures could be taken to recover the mangroves, the mangrove forest would become one of the mangrove forests in Fujian with the largest area joined together. This is of great scientific significance and there is also hope of developing tourist projects. Besides, in Jingfeng Town, there's also 0.1hm^2 of mangroves.

Fuzhou: The natural *Kandelia candel* forest used to be distributed in Changle, Fuqing, Lianjiang and Pingtan of Fuzhou, where, in the 1 950s and 1 960s, *Kandelia candel* forests were planted, but now they no longer exist. The forestry department of Pingtan planted 33.3hm^2 of trees in 1995, which have now been closed to become a forest. The tallest *Kandelia candel* reaches 2m and the average height is 1m. In 1998, it began to blossom and bear fruits.

Ningde region: The coastal counties and cities in the Ningde region include Fuding, Fu'an, Xiapu, Ningde and Luoyuan. In this region, there is only *Kandelia candel,* covering an area of 88.9hm^2. See Table 3 for its distribution. The *Kandelia candel* forest with the largest area joined together is located at Yaojiadu Village, Qianqi Town of Fuding, covering an area of 8.8hm^2. With a height of 1.5~2.0m, a canopy density of 80% and the maximum base measurement of 150cm, the trees are growing well, but the insect pest is serious. At present, this forest is under good protection as a major seed-collecting base for mangrove afforestation in Fuding. The 2.0hm^2 of *Kandelia candel* forest on the edge of Tianluo Village, Zhangwan Town of Ningde has seriously degenerated and nearly 6.7hm^2 of *Kandelia candel* forest on Mount Song in Luoyuan was being enclosed for cultivation at the time of investigation.

Tab. 3 Distribution of natural mangroves in Ningde area

Place	Area	Community type	Height	Condition of conservation
Fuding	48.8	*Kandelia candel* forest	1.5~2.5	good
Zhangwan, Ningde	2.0	*Kandelia candel* forest	0.5~2.5	bad
Badu,Ningde	1.3	*Kandelia candel* forest	1	mediocre
Feiluan,Ningde	0.1	*Kandelia candel* forest	1	mediocre
Xiapu salt pan	5.3	*Kandelia candel* forest	4	good
Xiapu salt pan	4.7	*Kandelia candel* forest	1~1.5	good
Fu'an*	20.0	*Kandelia candel* forest	1.5	good
Mount Song, Luoyuan	6.7	*Kandelia candel* forest	1	being enclosed for cutivation
Total	88.9	—	—	—

Note: * includes Wanyu, Xiwei, Xiabaishi and Saiqi.

Fujian has a mangrove area of 467.2hm^2 which has been closed (Nearly 6.7hm^2 of mangroves on Mount Song in Luoyuan was being enclosed for cultivation at the time of investigation, so it was not counted).The mangrove is mainly distributed in Zhangzhou, covering an area of 286.6hm^2 and accounting for 61.3% of the total. The areas of mangroves in Xiamen, Quanzhou, Fuzhou and Ningde are 31.8hm^2, 33.3hm^2, 33.3hm^2 and 82.2m^2 respectively.

3 Afforestation of Mangroves in Fujian in Recent Years

In recent years, with the gradual deepening of people's awareness of the mangrove's importance, an upsurge of mangrove afforestation has been set off in the coastal area of Fujian. The following is a brief account of mangrove afforestation in the major counties and cities:

Fuding: Fuding is the northern boundary of natural distribution of China's mangroves. In 1995 when we were conducting an investigation, we found some people destroying the mangrove forest. But during this investigation, we found such destruction has been completely stopped. Since 1997, organized by the forestry department, nearly 80.0hm^2 of mangroves have been planted in various places along the Shacheng Bay and the mangroves are growing well. And in some places, the local residents plant mangroves on their own initiative. In Yaojiadu Village, Qianqi Town of Fuding, there is a *Kandelia candel* forest with an area of 8.8hm^2, which has become the main source of seeds for mangrove afforestation in Fuding.

Lianjiang: In April and May, 1998, the villages and towns of Guanfan, Guantou, Xiao'ao and Toubao planted 8.0 hm^2 of mangroves. As these villages and towns are situated at the Minjiang estuary , the freshwater supply is sufficient. Besides, the soil and the salinity of the water body are favourable. So the surrival rate of mangroves is over 90%, and the afforestation of mangroves is planned to be popularized at a rate of 6.7hm^2 every year.

Fuqing: In 1997, about 13.3hm^2 of mangroves were planted in Chengtou and other places, which were growing well with a survival rate of 80%. The three-year seedlings were as high as 60cm with 5~10 pairs of blades. Encouraged by this success, 10 villages and towns of Gangtou, Longtian, Gaoshan, Jiangyin, Xincuo, etc., planted about 100hm^2 more of mangroves, of which nearly 87hm^2 survived at the time of check and acceptance. This became a piece of major news in Fuqing and was reported by newspapers, television and other media one after another. But in some sections, the seedlings did not survive and the *Kandelia candel* seedlings are attached with close and numerous barnacles, which suggests that the ambient salinity in here is high. So whether the seedlings can grow up into a wood still awaits further observation.

Putian: A total of 13.3hm^2 of mangroves were planted in 1998, of which 6.7hm^2 in Pinghai Town had a survival rate of 95% while the other half did not survive.

Xiamen: In 1997, 20 000 seedlings were raised in Qingjiao, Haicang, in an area of about 1 hm^2, but 30% of them died after transplantation in 1998 and now 14 000 seedlings are left. In May, 1998, 23.3 hm^2 and 2.7hm^2 of mangroves were planted in Dadeng and Xike respectively, and were coming along fine at the time of check and acceptance, which was reported by newspapers and television. But with the lapse of time the seedlings began to die and, by the end of 1998, 2.7hm^2 of seedlings in Xike had all died and only about 0.2hm^2 of 23.3hm^2 in Dadeng was left, but was doing bad.

Longhai: Located at the Jiulongjiang estuary, Longhai boasts favourable conditions for afforestation and is a region in Fujian with the longest history of mangrove afforestation. In the early 1980s, about 100hm^2 of mangroves were planted and basically all grew up to woods. Since 1997, the Forestry Department in Longhai planted in succession about 33.3hm^2 of *Kandelia candel* on the idle tidal flat, which survived well due to their location at the Jiulongjiang estuary.

Pingtan: In 1995, 33.3hm^2 of mangroves were planted in Jianglou, which have now been closed to become a forest. The highest ones are 2m with 1 m in height on the everage. Encouraged by this, another

33.3hm^2 of mangroves were planted in Su'ao in 1996, but all died. So there was no plan of expanding the afforestation in 1997.

Besides, since the 1990s, afforestation activities of certain scale have been carried out one after another in Ningde, Jinjiang, Shishi and Zhangpu.

Since 1995, the coastal counties and cities in Fujian have planted a total of 593.3hm^2 of mangroves, but only about 326.7hm^2 have actually survived, so the rate of success in afforestation is only 55%. Our investigation was carried out mainly in November, 1998 when the new seedlings had not yet wintered, so the survival rate may be lower than anticipated.

4 Results of Investigation and Suggestions

(1) Since the 1990s, much more importance has been attached to the mangroves in Fujian. Except in individual places, damage to the mangroves has been checked in the main and all localities in the province are actively constructing the mangrove forests. According to preliminary statistics, the area of mangroves in Fujian has come to 467.2hm^2 or so and the newly constructed mangrove forest in recent years amounted to nearly 600hm^2, and the planned afforestation area is increasing year by year. A certain district plans to build a mangrove shelter forest belt, 30km in length, 30m in width and 93.3hm^2 in area as one of the practical things done by the district government for the people in 1999. Fu'an plans to build a coastal mangrove shelter forest belt, 114km long, 10～30m wide and 270~330hm^2 in total area at an annual speed of planting 33.3hm^2.

(2) Changing the situation of constructing the single *Kandelia candel* forest. Although the dominant position of *Kandelia candel* brooks no shaking at present, many tidal flats, especially the soil and the high-salinity water body in some sections are not suitable for the growth of *Kandelia candel,* but are fit for the afforestation of highly salt-resistant species such as *Avicennia marina.* Moreover, *Kandelia candel* in some places suffer seriously from diseases and insect pests. In Matou Village, Fu'an Bay, for example, almost all the leaves of *Kandelia candel* have been eaten up by the mangrove night moths. In Xiamen, Longhai, Zhangpu, Yunxiao and Zhao'an, besides *Kandelia candel, Avicennia marina* and *Aegiceras corniculatum, Bruguiera gymnorrhiza, Rhizophora stylosa, B. sexangula, B.s.* var. *rhynochopetala* and *Sonneratia apetala* may also be considered. It is necessary to organize manpower as soon as possible to carry out research on the seedling-raising and afforestation technologies for the above-mentioned species.

(3) Increasing scientific and technological input into mangrove afforestation and protecting the initiative of various localities in mangrove afforestation. In the past, the forestry departments in various localities planted mangroves somewhat at will, finding a plot of land on which to plant the hypocotyl and that's all, almost without considering the problems such as soil, salinity of water body, height of tidal level and cold resistance. Since 1995, the total area of afforestation has reached nearly 600hm^2 throughout the province, but the area of survival had been less than 333hm^2. In May, 1998, 26hm^2 of mangroves were planted on the tidal flats of Dadeng Island and Xike in Tong'an, Xiamen and were doing well at the time of check and acceptance, which was reported by newspaper and television in succession. But with the passage of time, the seedlings gradually began to die and at last few have been left. In 1999, a certain district planned to construct a mangrove shelter forest belt of *Kandelia candel*, 30km long, 30m wide and 93hm^2 in area as one of the practical things done by the district for the people. If this were not carefully planned and something went wrong again, the confidence of various departments would be

affected. None of the 33.3hm^2 of *Kandelia candel* planted in Pingtan in 1996 survived, so in 1997, nobody dared to plant it any more. Of the 233.3m^2 of *Kandelia candel* forest constructed between 1996 and 1998 in Fu'an, only one third was left in the end. Therefore, how to raise the survival rate in afforestation and protect the initiative of various localities for afforestration is a matter that must be taken seriously by the department responsible for forestry. Planting trees on the coastal tidal flat is entirely different from that on land. On land, the growth of seedlings may be improved by watering and applying fertilizer while, on the tidal flat, these measures won't work. The only measure that could be taken is to do a good job of planning and to fully understand the habitat conditions of the tidal flat so that the right mangroves could be planted in the right places.

(4) The technical backbone of forestry in various coastal counties and cities should be organized as soon as possible to participate in the training courses on the basic knowledge of mangroves, in which they could exchange experience of various localities in mangrove afforestation and discuss the relevant knotty problems. This matter can be taken up by the Burean of Forestry and implementd by Xiamen University. At present, mangrove afforestation throughout the province lacks unified planning and technical guidance and basically relies on the fumbling of the forestry departments in various localities. Each locality has accumulated much experience in the course of afforestation and also come across many difficult problems. With a history of nearly 40 years in mangrove research, the Department of Biology, Xiamen University has accumulated rich theoretical knowledge and done some work in the introduction and afforestation of mangroves. Therefore, integration of the advantages of the local and scientific research departments is bound to benifit the development of mangroves in Fujian.

References

[1] Lin Peng and Fu Qin (1995) Environmental Ecology and Economic Utilization of Mangroves in China. Bejing: Higher Education Press, 30-32.

[2] Lin Xi (1998) *Barringtonia racemosa* —A Gardens Ornamental Plant with Great Value for Development. *Subtropic Plants Bulletin*, **27** (2): 45-47.

[3] Zhang Raoting and Huang Dunqin (1992) Account of the Mangrove Plant *Acrostichum aureum* in Fujian. *Journal of Oceanography in Taiwan Strait*, **11** (4): 372-373.

[4] Lin Laiguan and Huang Youru (1962) Mangrove community in Fujian. *Journal of Fujian Normal College*, (4): 87-104.

[5] Zhang Weiqiang and Huang Zhenguo (1996) Taiwan's Mangrove and Its Environmental Implications. *Tropical Geography*, **16** (2): 97-105.

[6] Wang Mingguo and Xu Shuhua (1997) *Hibiscus hamabo*. *Plants*, (1): 13.

Studies on Antineoplastic Constituents from Marine Bryozoan *Bugula neritina* Inhabiting South China Sea (III): Isolation and Structural Elucidation of Bryostatins 10, 11 and 18

Lin Houwen (林厚文)*, Yi Yanghua (易杨华), Yao Xingsheng (姚新生)[1], Wu Houming (吴厚铭)[2]
School of Pharmacy, Second Military Medical University, Shanghai 200433

Abstract Six active compounds are isolated from the marine bryozoan *Bugula neritina*, inhabiting the Nanwan Bay in the South China Sea, using the bioassay-guided method with a combination of extraction and partitionation with suitable solvents as well as multiple column chromatographies (Sephadex LH－20, ODS and preparative HPLC). Their structures are identified as known bryostatins-- bryostatins 4, 5, 6, 10, 11 and 18 through intensive analysis of the data of high resolution 2D NMR (600 MHz, DQF-COSY, TOCSY, HMQC and ROESY) and ESI-MS. Among them, bryostatins 10, 11 and 18 are for the first time obtained from this bryozoan in the South China Sea and they show significant antineoplastic activities *in vitro*.

Keywords *Bugula neritina*, antineoplastic activities, bryostatins

The marine bryozoan *Bugula neritina* is one of the common fouling organisms in our country as well as the most prominent bryozoa with a broad geographic range in the world. The author makes an extensive investigation of antineoplastic constituents from this animal collected off the Dapen Bay in the South China Sea. As a result, a new macrolide bryostatin 19 together with three known bryostatins have been isolated from this animal.[1, 2] In order to make the best of the marine resources in China, the investigation of the resource of *Bugula neritina* is carried out in some main harbors in Guangdong, Guangxi, Fujian and Hainan provinces. An intensive investigation of antineoplastic constituents from this animal collected off the Nanwan Bay in Guangxi province is carried out. Encouragingly, six active compounds are isolated from this specimen. Their structures are identified as bryostatins through intensive analysis of the data of high resolution 2D NMR and ESI-MS. Among them, bryostatins 4, 5 and 6 have been isolated from this animal in the South China Sea,[2] where bryostatins 10, 11 and 18 are for the first time obtained from this animal inhabiting the South China Sea.

1 Materials and Methods

1.1 Instruments

See ref. 2.

1.2 Sample collection

About 100kg (wet weight) of specimens was collected off the Nanwan Bay (Guangxi Province) in

* Author to whom correspondence may be addressed. Address: Department of Pharmacy, Shanghai Changzheng Hospital, Shanghai 200003, China
1 Department of Natural Products, Shenyang Pharmaceutical University, Shenyang 110015, China
2 Shanghai Institute of Organic Chemistry, Chinese Academy of Sciences, Shanghai 200032, China

March 1997 at a depth of 0~1.5 m. Taxonomic identification was performed by professor Li Chuanyan (Third Institute of Oceanography, State Oceanic Administration). The authentic samples *Bugula neritina* are preserved in our laboratory.

1.3 Extraction and isolation

Freshly collected animals (60Kg, dry weight) are extracted with 95% ethanol (500L) at room temperature for four times, each extraction taking one week. The resulting extract solution is removed, filtered and concentrated under reduced pressure to aqueous extracts (2 kg). The aqueous extracts are suspended into 9:1 methanol- water solution, and extracted with n-hexane (10L) for five times. The n-hexane phase is separated and concentrated in vacuum to give 560g n-hexane extracts (no active, P388). The methanol-water phase is adjusted to a concentration of 4:1 and partitioned with carbon tetrachloride (10L) for five times. The carbon tetrachloride phase is removed and concentrated in vacuum to give an active portion (60 g, $IC_{50} = 7\times10^{-1}$ μg/mL, P388).

A bryostatin-containing fraction 2BH-10 (2.7 g, $IC_{50} = 2.4\times10^{-2}$ μg /mL, P388) is obtained from the silica gel flash column chromatography with SiO_2 (200-300 mesh) using CH_2Cl_2 → MeOH-CH_2Cl_2 (1:9) as eluting solvent. 2BH-10 is subjected to chromatography on a column of Sephadex LH-20 (3.8 × 110 cm), using CH_2Cl_2 -MeOH (1:1) as eluting solvent. Fractions measuring 12 ml are collected at the rate of 60 ml/h. This procedure causes a rapid concentration in fractions A (1.7g, $IC_{50} = 3\times10^{-3}$ μg /mL, P388) and B (1.1g, $IC_{50} = 8\times10^{-3}$ μg /mL, P388) of the major active compounds. Further gel permeation-partition type chromatographic separation employing Sephadex LH-20 with n-hexane-CH_2Cl_2-MeOH (4:5:1) and (10:10:1) as eluting solvent leads to the purer and more active bryostatin-containing fractions of C (0.7 g, $IC_{50} = 1\times10^{-3}$ μg /mL., P388) and D (0.5 g, $IC_{50} = 0.8\times10^{-3}$ μg /mL, P388). These two fractions still contain some kinds of green pigments. Therefore, C and D are combined for further separation. Using intensive ODS flash column chromatographic method with solvent gradient of 50%→80% MeOH, a major bryostatin-containing fraction E (0.8 g, $IC_{50} = 2.4\times10^{-4}$ μg/mL, P388) is selected for further purification. The following silica gel column chromatography using n-hexane-acetone (5:1 → 1:1) as eluting solvent leads to two fractions F (0.4 g) and G (0.2g). F is subjected to HPLC using a Partisil C-18 reversed phase column with 83% MeOH as eluting solvent. In this manner, compounds 1 (10mg), 2 (65mg) and 4 (50mg) are obtained. G is still challenging mixtures that need further purification before HPLC separations. As a result of Lobar MPLC method with solvent gradient of 50%→80% MeOH, G_1(5 mg), G_2(12 mg) and G_3(34 mg) are obtained. G_1 is subjected to preparative HPLC using a Partisil C-18 reversed phase column with 75% MeOH as eluting solvent, compound 3 (2.1mg) is obtained. G_2 and G_3 are subjected to preparative HPLC using a Partisil C-18 reversed phase column with 85% MeOH as eluting solvent, compound 5 (5.8mg) and compound 6 (18mg) are obtained.

2 Results and Discussion

2.1 Structural elucidation

Compound 1 is obtained as a white amorphous powder, mp 156-159 ℃. The UV spectrum indicates the presence of α , β - unsaturated esters (λ_{max}^{MeOH} = 228.7 nm). The ESI mass spectrum of 1 (m/z 832 $[M+Na+H]^+$, 1641 $[2M+Na+2H]^+$) and its ultimate analysis indicate an empirical formula of $C_{42}H_{64}O_{15}$, which corresponds to that of bryostatin 10 and bryostatin 18. Bryostatins 10 and 18 prove to be geometrical isomers of the α , β - unsaturated ester at C-21 (Fig. 1)[3, 4, 5]

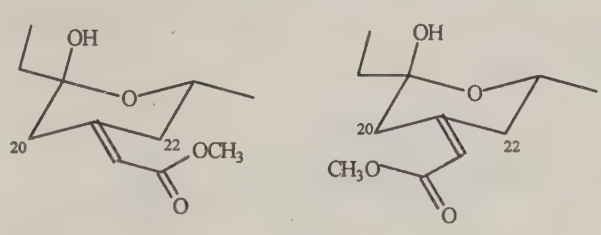

bryostatin 10 bryostatin 18

Fig. 1 Partial geometrical structures of bryostatins 10 and 18

The ^{1}H- and ^{13}C-NMR spectra of these two bryostatins are very similar, except for the chemical shifts at C-20 and C-22. In the ^{1}H-NMR spectrum of bryostatin 18, the two H-20 proton signals are at δ 3.79 and 2.10 where the two from H-22 are at δ 2.23 and 2.02. By comparison, the H-20 protons of bryostatin 10 appear at δ 2.73 and 2.20 and signals for the two H-22 protons at δ 4.00 and 1.95. The high unequivalence of these two protons at C-22 of bryostatin 10 and that at C-20 of bryostatin 18 are on account of the effect of the methoxyl or the carbonyl group of the α , β - unsaturated ester at C-21. Accordingly, the E or Z geometry of the double bond at C-21 can be determined by the observation of the high unequivalence of the two protons at C-21 or C-22. In addition, the ^{13}C-chemical shifts for the C-20 and C-22 carbons of bryostatin 18 appear at δ 33.70 and 43.13 while the C-20 and C-22 carbons of bryostatin 10 appear at δ 40.39 and 36.63, which is also owning to the effect of the methoxyl on C-35. The detailed structure of 1 is determined by direct comparison of its ^{1}H and ^{13}C-NMR data with those of bryostatin 10 and bryostatin 18. The ^{1}H- and ^{13}C-NMR data are almost the same as those of bryostatin 18 (Table 1).[3] Thus, compound 1 is identified as bryostatin 18 (Fig. 2).

The relative stereochemistry of 1 is settled by intensive interpretation of ^{1}HNMR coupling constants and ROESY data of 1. The E geometry of the $\triangle^{16,17}$ double bond are readable according to the coupling constant of 16.11 Hz between H-16 and H-17. The axial orientation of H-15 is supported by the NOE cross peak between H-17 and H-15 in the ROESY spectrum. In the same manner, H-11 is also assigned as axial on the basis of the NOE cross peak between H-15 and H-11. An intensive ROESY cross peak between H-5 and H-7 reveals their *cis* relationship. H-7 (δ 5.10, dd, J = 11.97, 4.95 Hz) is assigned as axial on the basis of the large coupling constant (*J*aa = 11.97 Hz) with the adjacent axial proton at C-6. Therefore, the orientation of H-5 is assigned as axial according to their *cis* relationship.

In the ^{1}H-NMR of 1, a doublet at δ 4.75 (*J* = 2.89 Hz) is unique. In the corresponding HMQC spectrum, no cross peak with the doublet can be observed. This indicates that the proton is not a carbon-conjugated proton (C - H). So the doublet has to be assigned to the hydroxyl group at C-19, or 25, or 9, or 3. Assigning the doublet to 25-OH, 9-OH and 3-OH seems to be impossible due to lack of the support of NOEs with its adjacent protons. In the ROESY spectrum of 1, a ROESY cross peak may be observed between the doublet and 23-H (δ 4.75/4.05). Therefore, the doublet is unambiguously assigned to 19-OH.

The geometry of the α , β - unsaturated ether at C-13 is strongly supported by the ROESY correlations as shown in Fig. 2.

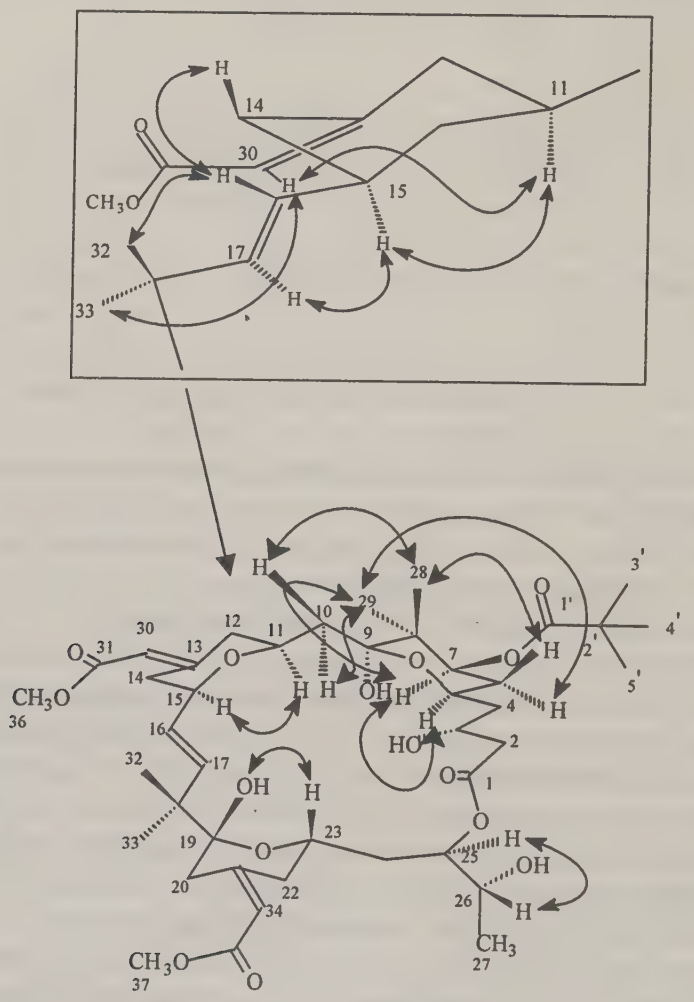

Bryostatin 18

Fig. 2 Summary of ROESY correlations observed for compound 1, t_m 300 ms, $CDCl_3$. Geminal and some vicinal correlations are omitted for clarity.

Compound 2 is obtained as a white amorphous powder, mp 160~164°C. The UV spectrum indicates the presence of α , β - unsaturated esters (λ max^{MeOH} = 228.7 nm). The ESI mass spectrum of 2 (m/z 832 $[M+Na+H]^+$, 1641[$2M+Na+2H]^+$) and its ultimate analysis indicate an empirical formula of $C_{42}H_{64}O_{15}$, which corresponds to that of bryostatin 10 and bryostatin 18. Bryostatins 10 and 18 prove to be stereoisomers of the α , β- unsaturated ester at C-21. The detailed structure of compound 2 is determined by direct comparison of its ^1H and ^{13}C-NMR data with those of bryostatin 10[4] The ^1H- and

^{13}C-NMR data are almost the same as those of bryostatin 10 (Table 2). Thus, compound 2 is identified as bryostatin 10 as depicted in Fig.3.

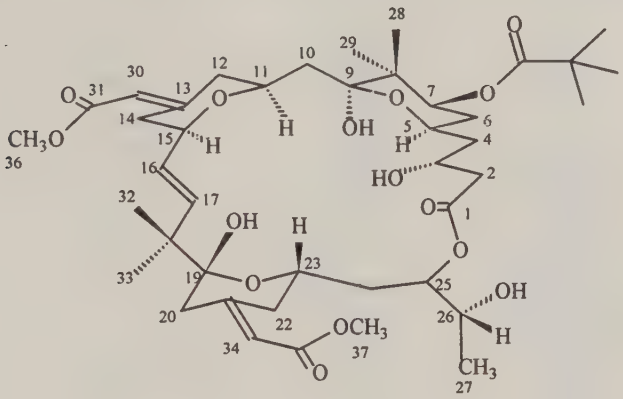

2

Bryostatin 10

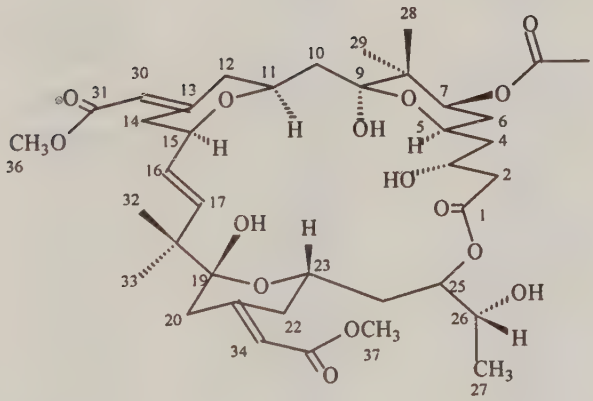

3

Bryostatin 11

Fig. 3 Structures of Compounds 2 and 3

Compound 3 is obtained as a white amorphous powder, mp 156~159℃. The UV spectrum indicates the presence of α , β - unsaturated esters (lmaxMeOH = 228.7 nm). The ESI-MS (m/z 790 [M+ Na + H]$^+$, 1557 [2M + Na + 2H]$^+$)and its ultimate analysis indicate an empirical formula of C_{39} H_{58} O_{15}, which corresponds to that of bryostatin 11.[5, 6] The data of ^{1}H-NMR and ^{13}C-NMR spectra are not determined for the scarce sample. By the chemical evidence and spectral data mainly based on ESI-MS, compound 3 is identified as bryostatin 11 as depicted in Fig. 3.

Compounds 4, 5 and 6 are identified as bryostatins 4, 5 and 6. See Ref. 2.

Tab. 1 ^{1}H-NMR and ^{13}C-NMR data for compound 1[a] and bryostatin 18[b]

Position	^{1}H-NMR		^{13}C-NMR	
	Compound (1)	Bryostatin 18	Compound (1)	Bryostatin 18
1			172.44	172.37
2a	2.50 m	2.50 brs	42.21	42.73
2b	2.46 m	2.50 brs		
3	4.11 m	4.04 m	68.16**	69.81
9-OH	3.99 m			
4a	2.0 (overlaped)[c]	1.80 *	39.70	40.95
4b (α)	1.55 (overlaped)	1.70 *		
5	4.22 brt	4.20 brt	65.69	66.70
6eq	1.70 (overlaped)	1.64 *	33.19	34.02
6ax	1.43 dt (11.5, 11.5)	1.45 dt (12, 12)		
7	5.10 dd (4.95, 11.97)	5.07 dd (5, 12)	72.46	73.20
10a	2.08 (overlaped)	1.99 *	42.08	42.73
10b	1.66 (overlaped)	1.73 *		
11	3.88 brt	3.92 *	71.31	73.44
12a (α)	1.72 m	2.17 *	44.74	44.71
12b	1.94 m	2.17 *		
13			156.71	158.89
14eq	3.66 (overlaped)	3.57 brd (12)	36.54	37.36
14ax	1.90 (overlaped)	1.91 *		
15	4.09 m (overlaped)	4.10 *	78.99	80.51
16	5.37 dd (8.67, 16.11)	5.31 dd (8, 16)	130.41	130.94
17	5.83 d (16.11)	5.87 d (16)	138.04	139.85
18			44.85	45.68
19			100.97	101.98
20a	3.67 s (overlaped)	3.79 d (12)	32.96	33.70
20b	2.05 m (overlaped)	2.10 *		
21			156.71	158.81
22a (β)	2.19	2.23 *	44.17	43.13
22b	2.02	2.02 *		
23	4.05 m	3.96 *	64.72	66.17
24a	1.90 m (overlaped)	1.95 *	36.16	36.03
24b	1.69 m	1.62 m		
25	5.13 m	5.12 *	73.53	73.25
26	3.78 m	3.75 *	70.14**	69.08
27	1.21 d (6.19)	1.07 d (6.7)	19.15	19.18
28	1.09	1.01 s	16.96	17.35
29	0.94 s	1.02 s	20.42	20.55
30	5.74 brs	5.76 brs	115.94**	114.52
31			166.87	167.73
32	1.02 s	0.89 s	21.02	21.33
33	1.10	1.09 s	24.44	24.75
34	5.68 brs	5.73 brs	114.28**	116.26
35			166.75	167.67
36	3.71 s	3.66 s	51.00	51.61
37	3.67 s	3.63 s	50.86	51.40
1'			178.01	178.54
2'			39.02	39.67
3'-5'	1.19 s	1.16 s	27.15	27.46
19-OH	4.75 d (2.89)	4.74 d (3)		

a Recorded on a Bruker AMX-600 (600 MHz) spectrometer in CDC_{13}

b Recorded on a Bruker AMX-400 (400 MHz) spectrometer in Deuterioacetonitrile

* Couplings for these signals are obscured.

Tab. 2 ^{1}H-NMR and ^{13}C-NMR data for compound 2[a] and bryostatin 10[b]

Position	^{1}H-NMR		^{13}C-NMR	
	Compound (2)	Bryostatin 10	Compound (2)	Bryostatin 10
1			171.60	172.64
2a	2.43 dd (2.3, 12.4)	2.44 d (11.7)	41.13	42.05
2b	2.53 t (12)	2.54 dd (12.2, 11.7)		
3	4.12 m	4.12 m	67.15	68.14
3-OH		4.03 s		
4a	1.54 m	1.54 d (14.7)	38.83	39.78
4b	1.97 m	1.97 m		
5	4.21 m	4.23 d (12.2)	64.58	65.64
6a	1.42 m	1.43 d	32.21	33.19
6b	1.71 m	1.71 brs		
7	5.12 m	5.10 ddd (11.9, 7.3, 4.4)	71.66	72.59
8			40.28	41.26
9-OH		4.81 s	100.78	101.79
10a	1.66 d (14.7)	1.62 brs	41.06	42.16
10b	2.08 m	2.08 m		
11	3.95 m	3.89 m	70.34	71.34
12a	2.06 m	2.06 m	43.20	44.19
12b	2.18 m (overlaped)	2.18 d(13.2)	43.20	44.19
13			156.15	157.04
14a	1.88 m	1.88 m	35.60	36.56
14b	3.66 m (overlaped)	3.66 m		
15	4.11 m	4.11 m	77.90	78.95
16	5.35 dd (8.5, 15.9)	5.36 dd (8.3, 15.6)	129.48	130.43
17	5.81 d (15.5)	5.81 d (15.6)	136.87	137.91
18			43.73	44.75
19-OH	5.04 d (2.7)	5.91 s	99.93	100.93
20a	2.16 m (overlaped)	2.14 m	38.77	39.78
20b	2.36 d (13.2)	2.35 d (14.2)		
21			156.00	157.04
22a	1.73 m	1.76 d (11.7)	35.11	35.72
22b	3.86 br d (13.2)	3.86 m		
23	3.98 m	3.98 m	63.62	64.61
24a	1.70 m	1.70 m	34.74	36.12
24b	1.95 m	1.95 m		
25	5.10 m	5.08 dd (14.2, 3.9)	72.79	73.83
26	3.74 m	3.75 m	69.18	70.23
27	1.20 d (6.2)	1.21 d (6.8)	18.63	19.68
28	1.03 s	1.03 s	16.05	17.06
29	0.93 s	0.94 s	20.05	21.07
30	5.67 brs	5.68 brs	113.12	114.19
31			165.97	167.01
32	1.03 s	1.03 s	19.38	20.39
33	1.08 s	1.08 s	23.45	24.45
34	5.69 brs	5.69 brs	114.71	115.73
35			165.78	166.81
36	3.70 s	3.71 s	50.03	51.08
37	3.66 s	3.67 s	49.79	50.84
1'			177.15	178.13
2'			38.04	39.05
3'-5'	1.18 s	1.19 s	26.14	27.16

a Recorded on a Bruker AMX-600 (600 MHz) spectrometer in $CDCl_3$

b Recorded on a JEOL JNM-EX400 (400 MHz) spectrometer in $CDCl_3$

2. 2 Results of cytotoxicities

The cytotoxicities of 1, 2 and 3 against U937 and K562 leukemia cell lines are measured by trypan blue dye exclusion or MTT (Microculture Tetrazolium) assay. As a result, three samples show strong cytotoxic activities against K_{562} leukemia cell line at an IC_{50} value of 2.2×10^{-3}, 2.6×10^{-3} and 3.4×10^{-4} μg/ml, respectively. They also exhibit prominent inhibitory activities against U937 cell line at an IC_{50} value of 1.8×10^{-2}, 2.0×10^{-4} and 5.2×10^{-4} μg /ml, respectively.

Acknowledgement

We appreciate the very necessary financial assistance provided by the National Natural Science Foundation of China (NNSFC, 29672050). Other helpful assistance has been contributed by Prof. Yoshiaki Kamano (Kanagawa University, Japan).

References

[1] Lin H. W., Yi Y. H., Yao X. S. et al. (1998) Bryostatin 19: A New Antineoplastic Component from *Bugula neritina* Inhabiting South China Sea. *Chinese Journal of Marine Drugs*, **65** (1) : 1-3.

[2] Lin H. W., Yi Y. H., Yao X. S. et al. (1998) Studies on Antineoplastic Constituents from *Bugula neritina* inhabiting South China Sea (1): Isolation and Structural Elucidation of Bryostatins 4, 5 and 6. *Chinese Journal of Marine Drugs*, **17** (3): 1.

[3] Pettit G. R., Gao F., Blumberg P. M. et al. (1996) Antineoplastic Agents. Isolation and Structural Elucidation of Bryostatins 16-18. *J. Nat. Prod*, 59: 286-289.

[4] Kamano Y., Zhang H. P., Hino A., et al. (1995) An Improved Source of Bryostatin 10, *Bugula neritina* from the Gulf of Aomori, Japan. *J. Nat. Prod*, 58: 1868-1875.

[5] Pettit G. R., Kamano Y., Herald C. L. et al. (1987) Isolation and Structure of Bryostatin 10 and 11. *J. Org. Chem*, 52: 2848-2854.

[6] Pettit G. R., Gao F., Sengupta D. et al. (1991) Isolation and Structure of Bryostatin 14 and 15. *Tetrahedron*, 47: 3601-3610.

Avoidance Reaction of *Penaeus Chinensis* to Heavy Metals (Pb, Cr, Zn) and Heavy Metal Mixtures (Pb-Cr, Pb-Zn)

Chen Minshan (陈民山)
Yellow Sea Fisheries Research Institute, CAFS, Qingdao 266071

Abstract Study on the avoidance response of *Penaeus chinensis* to heavy metals (Pb, Cr, Zn) and heavy metal mixtures (Pb-Cr, Pb-Zn) is carried out using a Y-model avoidance apparatus. The concentrations calculated to induce 50% avoidance rate by *Penaeus chinensis* are 11.4, 33.2 and 238.1mg/L for Pb, Cr and Zn, respectively. Mixtures of Pb-Cr and Pb-Zn produce additive effect in the avoidance test using *Penaeus chinesis*. But when the mixed Pb-Zn solution has 0.5 toxic unit Pb and 0.5 toxic unit Zn, the mixture seems to have synergistic effect.

Keywords *Penaeus chinensis*, heavy metal, avoidance reaction, joint action

Organisms of any kinds must position themselves, through their normal behavior in relation to the physical and chemical characteristics of their environments so as to favor their survival and reproduction. As early as the beginning of the century, fisheries biologists abroad began studies on the behavioral responses of fish to environmental stimulus to determine the optimal environment conditions. Afterwards, toxicologists also carried out experiments to study the behavioral responses of fish to harmful substances, aiming at finding the threshold concentrations of pollutants.

In order to understand the effects of pollutants on marine life, toxicologists in China have carried out studies on the avoidance response of fish to heavy metals and pesticides (Hu guoliang, 1983), and the avoidance response of *Penaeus chinensis* to heavy metals (Wu Zhangkuan, 1983). Reports on the investigation into mixed pollutants, however, have hardly been seen.

Penaeus chinensis is an economically-important species in China, migration being the prominent characteristics of its behavioral habits. It migrates from wintering grounds to estuaries and nearby sea areas to spawn in the spring every year. These areas are often heavily polluted, or prone to be polluted. If *Penaeus chinensis* cannot be adapted to the pollution changes physiologically and behaviorally, the affected populations most likely would sustain losses.

This study deals with the avoidance response of *Penaeus chinensis* to heavy metals (Pb, Cr, Zn) and heavy metal mixtures (Pb-Cr, Pb-Zn). The experiment was carried out in the laboratory in the Xiaomaidao research base of Yellow Sea Fisheries Research Institute from July to August of 1998.

1 Materials and methods

Penaeus chinensis artificially hatched and cultured by the Xiaomaidao research base of Yellow Sea Fisheries Research Institute is used as a test animal, the body length being 35cm. The test substances are Pb, Zn, and Cr in the form of lead nitrate ($Pb(N0_3)_2$), zinc sulphate ($ZnS0_4 \cdot 7H_20$) and potassium dichromate ($K_2Cr_20_7$), respectively.

A Y-model avoidance apparatus made of organic glass is employed. It consists of one primary

trough and two branch troughs. The primary trough is of cylinder pattern, 41 cm in diameter and 20 cm in height. A water control tube, 2cm in interior diameter and 9cm in height, is installed below the center of the primary trough. The branch troughs are equal in size. A fender is set up in the border between the primary trough and branch troughs. Two 20L wide-necked bottles are used as water storage tanks for keeping clean seawater and test solution, and connected with the inlet of the avoidance apparatus by plastic tubes. A schematic diagram of the avoidance system is given in Fig.1.

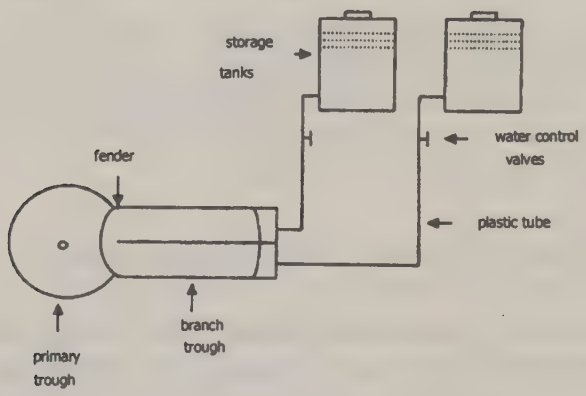

Fig. 1 Diagram of the avoidance test apparatus

Five concentrations in logarithmic series are set up for the single toxicant test. Put 15 shrimps into the primary trough with clean seawater, and keep them for 20 min. for adaptation. Then open the stop water valves. Both the clean seawater and test solution from the storage bottles flow into the primary trough at a velocity of 300ml/min. After 20 min., take off the fender, and note down the numbers of shrimp entering the different branch troughs every 5 min. for 4 times.

After the test is over, rinse the avoidance trough with clean water, and then start the second test by exchanging clean seawater trough and test solution trough. Repeat 4 times for each concentration.

Three concentrations are chosen for the test with mixed toxicants. Take the 50% avoidance rates of Pb, Cr, Zn calculated from the single toxicant test as each toxic unit.. Then educe the 3 concentrations of Pb-Cr mixture, in terms of 0.7, 0.5, 0.3 toxic unit Pb and 0.3, 0.5, 0.7 toxic units Cr. Similarly, educe the 3 concentrations of Pb-Zn mixture. Carry out the tests with the same method as that for the single toxicant test.

By adding up the results of 4 repeated tests for each single toxicant or mixed toxicants test, the avoidance rate is calculated according to the following formula,

$$\text{Avoidance rate (\%)} = \frac{E-A}{E} \times 100\%$$

Where E= No. of shrimp entering the clean seawater area.

A= No. of shrimp entering test solution area.

The 50% avoidance rate is calculated by using the probit method. Joint action is determined by using the equal toxicity solution method (Zhou Rongxin, 1989).

2 Results

The single toxicant test results are given in Tables 1~3. Using the probit method, the 50% avoidance rate of *Penaeus chinensis* to Pb, Cr and Zn are obtained. They are 11.4mg/L, 33.2mg/L and 238.1mg/L, respectively (see Fig.2).

Tab. 1 Avoidance reactions of *.Penaeus chinesis* to Pb

Concentration of test solution (mg/L)	No.of shrimp in clean seawater	No.of shrimp in test solution	Avoidance rate(%)
5.6	84	63	25
10	85	37	56.5
18	101	43	57.4
32	83	17	79.5

Tab. 2 Avoidance reactions of *Penaeus chinesis* to Cr

Concentration oftest solution (mg/L)	No.of shrimp in clean seawater	No.of shrimp intest solution	Avoidance rate(%)
3.2	38	54	0
5.6	54	86	0
10	67	61	8.9
18	87	75	13.8
32	93	42	54.8

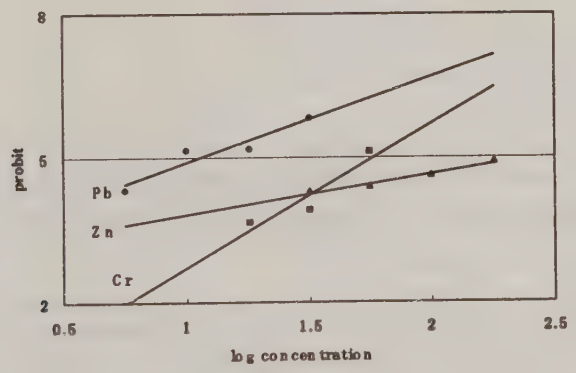

Fig. 2 Avoidance rates of *Penaeus chinensis* to Pb,Cr and Zn

Tab. 3 Avoidance reactions of *Penaeus chinesis* to Zn

Concentration of test solution (mg/L)	No. of shrimp in clean seawater	No. of shrimp in test solution	Avoidance rate(%)
10	68	74	0
32	96	73	24
56	88	64	27.3
100	67	43	35.8
180	91	54	40.7

The Pb-Cr mixture test results are given in Fig.3. The avoidance rates of *Penaeus chinensis* to 3 concentrations of Pb-Cr mixture at 0.7, 0.5, or 0.3 toxic unit of Pb with 0.3, 0.5, or 0.7 toxic unit of Cr are 51.5 %, 51.4 % and 51.9 %, respectively. Since the toxic units of the 3 concentrations are 1, their toxicity should be alike, equal to 1 toxic unit of Pb or Cr. If the avoidance rate to the toxicant mixture is above, or below the 50% avoidance rate line, then it indicates that the toxicant mixture presents synergism, or antagonism. If the avoidance rate of the toxicant mixture fluctuates at the 50% avoidance rate line, then it indicates that the toxicant mixture presents additive effects. As the avoidance rates of *Penaeus chinensis* to Pb-Cr mixture are all a little higher, but very close to the 50% avoidance rate line, the Pb-Cr mixture presents additive effects.

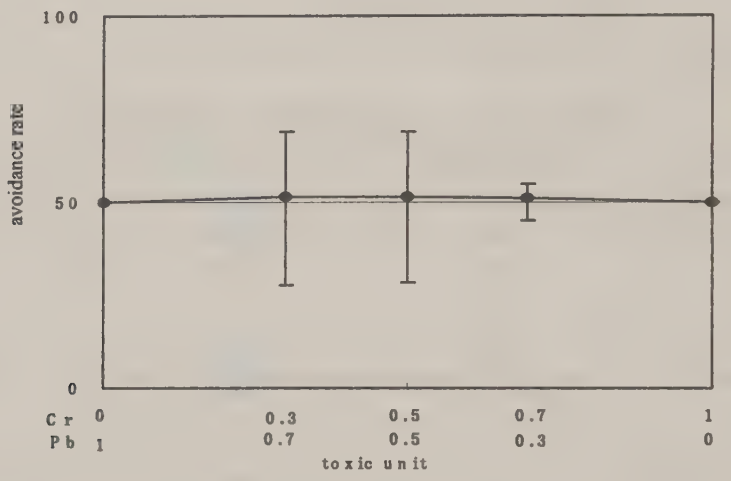

Fig. 3 Avoidance response of *Penaeus chinesis* to mixed toxicant(Pb and Cr) in different proportions (Vertical bars represent the range of 95% confidence limit)

The test results for mixtures of Pb-Zn are given in Fig.4. The avoidance rates of *Penaeus chinensis* to 3 concentrations of Pb-Zn mixture at 0.7, 0.5, or 0.3 toxic unit of Pb with 0.3, 0.5, or 0.7 toxic unit of Zn are 50.8 %, 59.4 % and 47.8 %, respectively. The avoidance rates of Penaeus chinensis to of Pb-Zn mixture at the concentrations of 0.7 toxic unit of Pb with 0.3 toxic unit of Zn and 0.3 toxic unit of Pb with 0.7 toxic unit of Zn are similar with those of Pb-Cr mixture, also presenting additive effects. But the avoidance rates of *Penaeus chinensis* to Pb-Zn mixture at the concentration of 0.5 toxic unit of Pb with 0.5 toxic unit of Zn are significantly greater than 50%, indicating that the Pb-Zn mixture presents synergic effect.

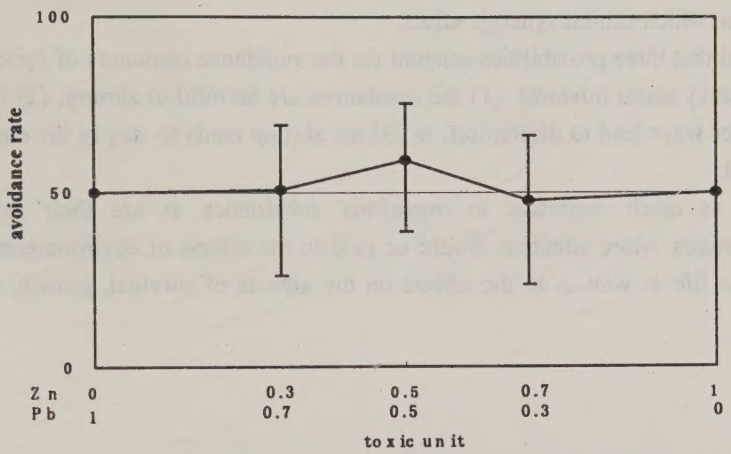

Fig. 4 Avoidance response of *Penaeus chinesis* to mixed toxicant (Pb and Zn) in different proportion (Vertical bars represent the range of 95% confidence limit)

3 Discussion

Penaeus chinensis is shown to avoid Pb, Cr and Zn, and the avoidance reaction is boosted up with the increase of the substances concentrations. Comparing the harmful effect of Pb, Cr and Zn on *Penaeus chinensis*, in terms of 50% avoidance concentration, it can be seen that Pb is the most toxic, Cr in the next place, and Zn last. It is worth pointing out that the effect sequence of toxicants based on 50% avoidance might not be in keeping with that based on LC_{50}.

Avoidance reaction is the integrated function responses of organisms to the environmental changes, so the avoidance threshold concentrations are normally lower than the lethal threshold concentrations. Studies have indicated that some fish species avoid pollutants having concentrations two orders of magnitude lower than the lethal threshold. But in some instances, organisms don't avoid polluted solutions at the incipient lethal level. It is presumably due to the difference of functioning mechanisms. Pollutant substances lead to the behavioral responses of organisms through their sense organs, while pollutant substances interfere with the morphological structures and physiological systems of organisms through their target organs.

Organisms of different kinds avoid polluted water with the same harmful substance variously. It is reported that both *Cyprinodonvariegatus* and *Gambusia affinis* exhibit marked alarm behavioral reaction to DDT, but *Palaemometes pugio* hardly avoids this harmful substance. Hu Guoliang (1983) found the 50% avoidance rates of *Mugil so-iuy Basilewsky* to Pb are 39mg/L. Compared with that result, *Penaeus chinensis* seems more sensitive than *Mugil so-iuy Basilewsky*.

When there are two or more toxic substances in seawater, the substances also exhibit joint action in the avoidance responses of marine organisms. Different species as well as the mixed proportions of

substances could affect the joint action. The avoidance reactions of *Penaeus chinensis* to Pb-Zn and Pb-Cr mixture basically exhibit additive effects, except the Pb-Zn mixture with 0.5 toxic unit of Pb and 0.5 toxic unit of Zn, which exhibit synergic effect.

It is suggested that three possibilities account for the avoidance responses of *Penaeus chinensis* to heavy metals or heavy metal mixtures: (1) the substances are harmful to shrimp; (2) the substances are irritating or in other ways lead to discomfort; or (3) the shrimp tends to stay in the environments which favor their survival.

Behavior is as much important to organisms' subsistence as are their morphological and physiological structures. More attention should be paid to the effects of environmental changes on the behavior of marine life as well as to the effects on the aspects of survival, growth, reproduction and so on.

References

[1] Zhou Yongxin, et al. (1989) Toxicity test method of aquatic organisms. Beijing: Agriculture Press.

[2] Carles E.W. (1971) Biology and water pollution control. W.B. Saunders Company.

[3] Sprague J.B. (1965) Sublethal copper-zinc pollution in a salmon river —a field and Laboratory study. *International Journal Air and Water Pollution* (Pergamon Press), 9:531-543.

[4] Warner R.E. (1966) Behavioural patholoy in fish: a quantitative study of sublethal pesticide toxication. *Journal of Applied Ecology*, 3 (Supplement): 223-247.

Marine Science Bulletin

Marine Science Bulletin publishes papers on marine science and technology including physical oceanography, chemical oceanography, marine biology, marine geology, environmental oceanography, estuarine & coastal sciences, marine technology, digital ocean, coastal zone management, ocean engineering, marine economics, etc., and aims to promote international academic cxchange.

Editor-in-Chief: Wang Hong（王 宏）
Deputy Editor-in-Chief: Lin Baofa（林宝法） Zhao Xucai（赵绪才）
Yang Ying （杨 鹰）
Executive Editor: Zhang Deshan（张德山） Xu Jie（徐 杰）
Computer typist: Cheng Xiuchun（程秀春）

Marine Science Bulletin **(Vol .3 No.1 May 2001)**

Responsible Institution:
State Oceanic Administration of China
Edited and Published Semi-annually by:
National Marine Data and Information Service
Address: 93 Liuwei Road, Hedong District, Tianjin 300171, China
E-mail: msb@mail.nmdis.gov.cn

ISSN1000-9620
CN12-1271/N **Price: $ 30.00 Per year**